Titre: Title:	Refinement of Non-Synchronous Vibrations Prediction in Axial Compressors
Auteur: Author:	Martin Drolet
Date:	2010
Type:	Mémoire ou thèse / Dissertation or Thesis
Référence: Citation:	Drolet, M. (2010). Refinement of Non-Synchronous Vibrations Prediction in Axial Compressors [Mémoire de maîtrise, École Polytechnique de Montréal]. PolyPublie. https://publications.polymtl.ca/488/

UNIVERSITÉ DE MONTRÉAL

REFINEMENT OF NON-SYNCHRONOUS VIBRATIONS PREDICTION IN AXIAL COMPRESSORS

MARTIN DROLET

DÉPARTEMENT DE GÉNIE MÉCANIQUE

ÉCOLE POLYTECHNIQUE DE MONTRÉAL

MÉMOIRE PRÉSENTÉ EN VUE DE L'OBTENTION

DU DIPLÔME DE MAÎTRISE ÈS SCIENCES APPLIQUÉES

(GÉNIE MÉCANIQUE)

DÉCEMBRE 2010

UNIVERSITÉ DE MONTRÉAL

ÉCOLE POLYTECHNIQUE DE MONTRÉAL

Ce mémoire intitulé:

REFINEMENT OF NON-SYNCHRONOUS VIBRATIONS PREDICTION IN AXIAL COMPRESSORS

Présenté par : DROLET Martin

en vue de l'obtention du diplôme de : Maîtrise ès sciences appliquées

a été dûment accepté par le jury d'examen constitué de :

M.TRÉPANIER Jean-Yves, Ph.D., président

M.VO Huu Duc, Ph.D., membre et directeur de recherche

M.MUREITHI Njuki W., Ph.D., membre et codirecteur de recherche

M.VÉTEL Jérome, Ph.D., membre

DÉDICACE

À Mélanie, Julie, Louise et Michel, pour
votre amour, support et soutien durant toutes
ces années d'études.

ACKNOWLEDGMENT

I would like to thank Pratt & Whitney Canada (P&WC), the Natural Science and Engineering Research Council of Canada (NSERC) and the Fond Québécois de Recherche sur la Nature et les Technologies (FQRNT) for funding and supporting this research initiative through an Industrial Innovative Scholarship (IIS). I would also like to thank P&WC for the authorization to publish this work. I am very grateful to Dr. Jean Thomassin for believing in me and for all the mentoring and numerous insightful discussions on non-synchronous vibrations.

Part of this project would not have been possible without the precious collaboration of the Special Tests organization at P&WC under the direction of Mr. Richard Lahaie who I am entirely grateful for his support. More specifically, I would like to thank the following people, in no particular order, for their contributions to the project: Patrick Rousseau, Benoît Patry, Daniel Summers-Lépine, Martin Cloutier, Renaud Lévesque, Yvon Michaud, Keith Ward, Michael W. Krieger, Jasmin Lamoureux, Michel Collin, André LeBlanc, Sylvain Bélanger and Sylvain Poupart. I would also like to acknowledge the support and mentoring of my director, Dr. Huu-Duc Vo and co-director, Dr. Njuki W. Mureithi. I would like to thank Benedict Besner and Kenny Huynh, from the lab at École Polytechnique de Montréal, for their help with the project. I am also very grateful to Shinya Ueno for his indescribable help with particle image velocimetry during the experimental tests.

Last, but not least, I would like to thank my girlfriend, Mélanie Brillant, my family: Julie Beaulieu-Drolet, Louise Beaulieu and Michel Drolet and my friends: Mathieu Côté, Martin Joly, Charles Paré, Laurence Côté, Mélissa Théorêt, Alexandre Charest and Alexandre Bernard, for all their motivation and support throughout my university studies. Without these precious people, I would certainly not be the person I am today and I am very grateful to them for what they all bring to my life.

RÉSUMÉ

Les vibrations asynchrones, ou NSV (de l'anglais « Non-Synchronous Vibrations »), ainsi que le flottement classique font parties de la famille des vibrations induites par les écoulements (ou FIV de l'anglais « Flow-Induced Vibrations ») observées dans les turbomachines. Les FIV sont habituellement causées par l'interaction des fluctuations de la charge aérodynamique sur une structure et la structure elle-même. Elles sont généralement classifiées en deux catégories distinctes, soient les réponses forcées et les instabilités fluide-élastiques qui regroupent, entre autres, les NSV et le flottement classique. Plusieurs cas de NSV ont été rapportés dans l'industrie, dans les étages avant de compresseurs axiaux, et sont typiquement reliées aux dommages en fatigue des aubes. Cependant, le mécanisme physique pouvant expliquer les NSV n'est pas entièrement compris et universellement accepté. Des études antérieures ont suggérées que les fluctuations de l'écoulement de jeu, qui surviennent plus souvent à haute charge aérodynamique et pour des jeux assez grands, pourraient expliquer les NSV. Une autre hypothèse suggère que les NSV découlent de l'impact de l'écoulement de jeu sur l'intrados d'une aube adjacente et que l'étude de la dynamique d'un jet impactant pourrait possiblement expliquer les NSV. Un modèle, basé sur l'analogie d'un jet impactant en résonance, a été proposé afin de prédire les vitesses critiques auxquelles les NSV peuvent survenir. Ce modèle a été statistiquement vérifié et validé expérimentalement. En dépit du fait que le modèle soit capable de fournir une bonne approximation *a priori* des vitesses critiques de NSV, il a été démontré expérimentalement que l'exactitude des prédictions découlant du modèle est très sensible à un paramètre k, qui a été définit comme étant le « coefficient de convection de l'instabilité ». En effet, les prédictions du modèle ne s'avèrent justes que si le coefficient k est connu.

Cet ouvrage présente une étude du modèle de NSV proposé, basé sur l'analogie du jet impactant en résonance décris précédemment, qui utilise principalement des outils numériques afin d'améliorer les prédictions des vitesses critiques de NSV. L'étude démontre que le paramètre « k » est influencé par la grandeur du jeu ainsi que la température d'opération. Cependant, l'effet dominant semble provenir de la grandeur du jeu alors que l'effet de la température sur « k » peut être négligé à des fins de conception. Les travaux suggèrent également que les résultats obtenus devraient être générique, i.e. indépendant de la géométrie utilisée. La principale contribution des travaux est donc une corrélation basée sur des résultats numériques, qui peut déterminer le

paramètre k indépendamment de la géométrie, ce qui améliore de façon significative les prédictions de NSV d'après le modèle proposé et en fait un outil de conception pouvant être utilisé dès les premières étapes de conception d'un rotor de compresseur axial. De plus, cet ouvrage propose une configuration possible pour rencontrer les NSV en conditions d'étranglement alors qu'elles sont connues jusqu'à présent pour survenir près du décrochage.

ABSTRACT

Non-Synchronous Vibrations (NSV), along with classical flutter, are part of the Flow-Induced Vibrations (FIV) family observed in turbomachineries. FIV are typically caused by the interaction of the unsteady aerodynamic loading on a structure and the structure itself and can be generally classified into two categories, which are Forced Responses and Fluid-Elastic Instabilities. The latter regroups NSV and classical flutter. A number of NSV cases have been reported in the industry, in the front stages of axial compressors, and are typically known to cause high-cycle fatigue damages. However, the physical mechanism underlying NSV is not yet fully understood and universally accepted. Previous studies have suggested that the tip clearance flow oscillations, which are more likely to occur at large tip clearances and high aerodynamic blade loading, could explain NSV. It was also suggested that NSV could arise from the impingement of the tip clearance flow leakage on the blade pressure side and that the study of the dynamics of impinging jets could explain NSV. A model to predict the critical speed at which NSV are likely to occur was derived, based on the resonant impinging jet analogy. The model was statistically verified and experimentally demonstrated. Although the proposed model provides a very good approximation of the critical NSV speed, it was found very sensitive to what was defined as the "instability convection coefficient" (k). It was found from experiments that the proposed NSV model can only yield accurate predictions of the critical NSV speed if the k parameter is known.

This work investigates NSV based on the proposed model and the resonant impinging jet analogy, mainly using CFD, to improve the critical NSV speed predictions. The results showed that the k parameter is influenced by both the tip clearance size and operating temperature. However, the dominant effect appears to come from the tip clearance size while the effect of temperature on k can be neglected for design purposes. In addition, this work suggests that the results should be generic, i.e. independent from the geometry used. The main contribution from the current Thesis is a correlation for the k parameter that is independent from the geometry, based on a numerical experiment, which significantly improves the critical NSV speed predictions and makes the proposed model independent from further experiments or numerical studies. In addition, this work also proposes a possible configuration to encounter NSV, which are typically known to occur near stall, in choked flow conditions.

CONDENSÉ EN FRANÇAIS

Chapitre 1: Introduction.

De nos jours, les compagnies de turbines à gaz repoussent continuellement les limites en termes de ratio poussée/poids et de consommation spécifique des moteurs afin de demeurer compétitif sur le marché. La réduction constante du poids des pièces pose de nouveaux défis en ce qui a trait aux vibrations des diverses composantes. La compréhension des divers phénomènes de vibrations, souvent associés aux dommages en fatigue des pièces, est donc primordiale afin de profiter pleinement des avantages compétitifs sur le marché. Le présent ouvrage se concentre sur un type particulier de vibrations rencontrées dans les modules de compresseurs axiaux: les vibrations asynchrones, ou NSV (de l'anglais « Non-Synchronous Vibrations »).

Problématique et objectifs.

Un modèle, sous la forme d'une équation, a été développé par Thomassin, J., Vo, H.D. et Mureithi, N.W. (2008, 2009) et s'avère être un outil à la fois simple et puissant qui permet de déterminer les vitesses critiques de NSV. Cependant, les prédictions du modèle ne s'avèrent juste que lorsque la valeur exacte d'un paramètre k, défini comme le « coefficient de transport de l'instabilité en bout d'aube » est connue. En effet, l'approximation générale k=2 (Thomassin *et al*., 2009) s'avère inadéquate pour déterminer de façon précise les vitesses critiques. L'objectif principal du présent ouvrage consiste donc à utiliser la mécanique des fluides numériques afin d'améliorer les prédictions des vitesses critiques de NSV basées sur le modèle proposé par Thomassin *et al*. (2008, 2009). Plus spécifiquement, les objectifs sont :

- Estimer le paramètre « k » à l'aide d'un modèle numérique de l'écoulement et déterminer l'influence de la dimension du jeu et de la température d'opération sur sa valeur.
- Proposer une corrélation basée sur les résultats numériques permettant d'identifier le paramètre « k » pour une géométrie donnée afin d'améliorer les prédictions des vitesses critiques de NSV d'après le modèle de Thomassin *et al*. (2008, 2009).
- Examiner l'aspect générique, ou universel, des travaux par l'étude de la mécanique des fluides inhérente aux compresseurs axiaux et identifier la possibilité d'obtenir les NSV en condition d'étranglement du compresseur, par opposition aux conditions de décrochage où les NSV sont typiquement observées.

Chapitre 2 : Revue de la Littérature.

Historique des vibrations asynchrones.

Les compresseurs axiaux sont souvent assujettis aux vibrations qui sont généralement divisées en deux grandes catégories : les vibrations mécaniques, résultant de l'interaction physique entre les composantes, ainsi que les vibrations induites par l'écoulement, qui découlent souvent d'une interaction fluide-structure entre les aubes et l'écoulement de l'air. Cette dernière catégorie peut également être subdivisée en deux types distincts, soient les réponses forcées et les instabilités fluide-élastiques.

Les réponses forcées sont les vibrations les plus couramment rencontrées dans les compresseurs axiaux. Elles sont connues pour être « synchrones » avec la vitesse de rotation de l'arbre, ce qui signifie que la fréquence d'excitation sera un multiple entier de la fréquence de rotation de l'arbre, plus couramment désignée EO (de l'anglais « Engine Order »). Les vibrations asynchrones (NSV) quant à elles, ne surviennent pas nécessairement à un multiple entier de la fréquence de rotation de l'arbre.

Un cas typique d'instabilité fluide-élastique est connu sous le nom de « flottement ». Plusieurs types de flottement ont été répertoriés dans l'industrie (Dowell, E.H., Crawley, E.F., Curtiss Jr, .H.C., Peters, D.A., Scanlan, R.H. et Sisto, F., 1995) et ont été souvent confondus avec les vibrations asynchrones (NSV). Ceci explique pourquoi les cas de NSV n'ont été que vaguement répertoriés dans les 15 à 20 dernières années.

Un des premiers cas de NSV répertorié est attribué à Baumgartner M., Kamaler F. et Hourmouziadis J. (1995) qui ont fait le lien entre les instabilités rotatives (RI, de l'anglais « rotating instabilities ») à partir d'observations expérimentales. Les RI ont été grandement étudiées dans le passé comme une source d'excitation possible des aubes de compresseurs (Liu, J.M., Holste, F. et Neise, W., 1996; Kameier, F. et Neise, W., 1997a; Kameier, F. et Neise, W., 1997b; Mailach, R., Lehmann, I. et Vogeler, K., 2001a; Mailach, R., Sauer, H. et Vogeler, K., 2001b; März, J., Hah, C. et Neise, W., 2002). Elles ont été modélisées comme étant une source de bruit émanant des fluctuations de l'écoulement au bord d'attaque en bout d'aube, possiblement liées aux NSV.

Ce n'est qu'en 2003 que les instabilités rotatives ont reçu l'appellation « vibrations asynchrones » (NSV) par Kielb, R.E., Thomas, J.P., Barter, J.W. et Hall, K.C. (2003) qui ont démontrés l'effet

des conditions d'opérations, tel que la température, sur les NSV et ont fait le liens avec les instabilités de l'écoulement de jeu à l'aide de modèles numériques. Ils ont également observé un changement soudain des formes de mode en fréquence, pour des conditions d'opérations constantes, ce qui s'avère un phénomène caractéristique aux NSV. Par la suite, Vo, H.D. (2006) a observé que le refoulement de l'écoulement de jeu en bord de fuite pouvait possiblement agir comme un jet impactant sur l'aube adjacente, lorsque la charge aérodynamique est élevée. Ce phénomène a également été observé expérimentalement par Deppe, A., Saathoff, H. et Stark, U. (2005). Basé sur ses observations, Vo, H.D. (2006) a donc proposé d'étudier la dynamique d'un jet impactant comme une explication possible des vibrations asynchrones.

Théorie de la rétroaction d'onde dans le noyau potentiel d'un jet.

Thomassin *et al*. (2009) ont donc répété l'expérience d'un jet impactant sur une plaque de Ho, C.-M. et Nosseir, S. (1981). Par contre, leur plaque était flexible et en vibration afin de simuler une aube de compresseur en porte-à-faux. Cette plaque flexible permettait donc des fluctuations de pression au centre du jet, au point de stagnation, ce qui crée une onde de rétroaction additionnelle à l'intérieur même du noyau potentiel du jet. Par conséquent, cette nouvelle onde de rétroaction se propage à une vitesse U_B de sorte que $U_B = c - U$, où c est la vitesse du son locale (équation (2.1), p.14). Afin que le jet entre en résonance, ceci implique que la fréquence réduite du jet doit satisfaire la condition définie à l'équation (2.2), p.14. Ils ont également trouvé que la distance jet-plaque (L) doit satisfaire $L = n\lambda_B/2$, où λ_B est la longueur de l'onde de rétroaction et n est un multiple entier qui tient compte des super-harmoniques de la longueur d'onde (voir équation (2.3), p.14). Ces relations présentent donc la base derrière la théorie de la rétroaction d'onde dans le noyau potentiel d'un jet impactant (en anglais : « Jet-Core Feedback Theory ») proposée et validée expérimentalement par Thomassin *et al*. (2009).

Modèle de prédiction des vibrations asynchrones.

Thomassin *et al*. (2008, 2009) ont alors suggéré que lorsque certaines conditions d'opérations sont rencontrées (haute charge aérodynamique et vitesse du son adéquate), la résonance de l'écoulement de jeu, de façon analogue au modèle de l'onde de rétroaction dans le noyau potentiel d'un jet impactant, pouvait être le mécanisme physique derrière les NSV. Un modèle, sous la forme d'une équation (équation (2.4), p.17), a alors été proposé par Thomassin *et al.* (2009) afin de prédire la vitesse critique en bout d'aube à laquelle les NSV peuvent être

rencontrées. Dans cette équation, U_{tipc} est la vitesse critique en bout d'aube à laquelle les NSV devraient survenir, c est la vitesse du son en bout d'aube, s est le pas en bout d'aube (distance d'aube-en-aube), f_b est la fréquence naturelle de l'aube et n est un multiple entier relié aux super-harmoniques de l'onde de rétroaction acoustique. En utilisant l'égalité $U_{tipc} = k\ U_F$, où k est définit comme étant le « coefficient de transport de l'instabilité en bout d'aube » (de l'anglais, « tip instability convection coefficient », Thomassin *et al.*, 2009), on obtient une forme plus générale du modèle, tel que définit par l'équation (2.5) (p.17). Le modèle de NSV proposé par Thomassin *et al*. (2008, 2009) a été validé expérimentalement et il a été démontré que le paramètre « k » dans l'équation (2.5) discutée précédemment devait être connue afin que les prédictions des vitesses critiques de NSV s'avèrent justes. En effet, ils ont mesuré expérimentalement le paramètre « k » et les prédictions des vitesses critiques de NSV découlant de l'utilisation de la valeur adéquate de k étaient toutes à l'intérieur de 2% d'erreur par rapport aux vitesses critiques observées expérimentalement. L'approximation générale k=2 a démontrée des erreurs allant jusqu'à 20% pour les mêmes prédictions.

Modélisation numérique de la résonance de l'écoulement de jeu.

Une méthode numérique permettant d'améliorer les prédictions des vitesses critiques de NSV d'après le modèle de Thomassin *et al*. (2008, 2009) a également été développée par Drolet, M., Thomassin, J., Vo, H.D. et Mureithi, N.W. (2009). En effet, en utilisant une géométrie de compresseur identique à celle utilisée expérimentalement par Thomassin *et al*. (2008), ils ont démontré qu'un modèle de mécanique des fluides numérique, utilisant un maillage déformable afin de simuler les vibrations de l'aube, pouvait déterminer les vitesses critiques de NSV en se basant sur l'amplification des pressions instationnaires en bout d'aube. La vitesse du « jet » (U_F) définie par le modèle de Thomassin *et al*. (2008, 2009) a également été estimée par Drolet *et al*. (2009) en utilisant la vitesse moyenne de la composante tangentielle de l'écoulement de jeu, pondérée par l'aire du jeu, afin de calculer la valeur du paramètre « k » d'après les simulations numériques. Malgré que les résultats obtenus pour « k » se soient avérés prometteurs, il y avait tout de même une erreur de 6% par rapport aux valeurs observées expérimentalement par Thomassin *et al*. (2008). Des améliorations s'imposent donc à la méthode numérique utilisée afin de déterminer la valeur du paramètre « k ».

Chapitre 3 : Méthodologie.

Des simulations numériques (CFD) ont été conduites afin de déterminer la vitesse du « jet », U_F, utilisée pour calculer le paramètre « *k* » d'après le modèle de NSV de Thomassin *et al*. (2008, 2009). Une analyse dimensionnelle a été réalisée afin de déterminer les variables qui gouvernent le paramètre « *k* ». L'approximation utilisée dans cet ouvrage, résultant de l'analyse dimensionnelle est donc $k \approx G_2(\tau, T)$ (équation (3.5)) où G_2 est une fonction arbitraire. Dans cette relation, le paramètre τ représente la dimension du jeu normalisée par la longueur de la corde en bout d'aube et T représente la température normalisée par une température de référence. L'approximation de l'équation (3.5) concorde également avec les observations expérimentales de Thomassin *et al*. (2008). Les simulations ont alors été réalisées pour différentes dimensions du jeu en bout d'aube et différentes températures d'opération afin de déterminer l'effet de ces paramètres sur « *k* ».

Les simulations numériques ont été réalisées à l'aide du logiciel commercial ANSYS CFX (version 11) en régime permanent. Un modèle de turbulence *k*-ε a également été employé. Deux géométries présentant des caractéristiques aérodynamiques différentes, une subsonique et une transsonique, ont été utilisées dans l'espoir de conférer un aspect générique à la présente étude. Les simulations ont été conduites pour six vitesses de rotation de l'arbre différentes, correspondant à une plage similaire aux vitesses utilisées par Thomassin *et al*. (2008). La composante de vitesse tangentielle de l'écoulement de jeu (V_L), telle que définie par Rains, D.A. (1954) et utilisée par Storer, J.A. et Cumpsty, N.A. (1991), est utilisée dans cet ouvrage afin de déterminer la vitesse du « jet » U_F.

Chapitre 4 : Résultats et Discussion.

Profils de vitesse (V_L) dans le plan de la corde en bout d'aube.

La vitesse tangentielle de l'écoulement de jeu (V_L), tel que définit par Rains (1954), a été calculée à partir des simulations numériques pour les différentes dimensions de jeu et conditions d'opération simulées. Un exemple de résultats obtenus est présenté à la Figure 4.1 (p.37). Les résultats démontrent une forme similaire à un profil de jet dans la première moitié de la longueur de corde en bout d'aube, près du bord d'attaque. Ces résultats sont également similaires à ceux obtenus par Storer et Cumpsty (1991). Cette portion de l'écoulement de jeu est donc possiblement attribuée aux NSV suivant l'analogie du jet impactant proposée et validée par

Thomassin *et al*. (2008, 2009). La vitesse du jet U_F a donc été calculée, dans le présent ouvrage, en utilisant la vitesse moyenne de la composante V_L de l'écoulement de jeu, pondérée par l'aire effective de la grandeur du jeu, sur la première moitié de la longueur de la corde en bout d'aube. Cette définition est mathématiquement représentée par l'équation (4.1) en page 38.

Profils de vitesse (U_F) et modèle proposé pour k vs. τ.

Le profil de vitesse V_L a été analysé plus en détails au centre du jet précédemment identifié, soit à environ 20% de la corde en bout d'aube à partir du bord d'attaque. Des exemples de résultats obtenus pour les deux différentes géométries simulées sont présentés à la Figure 4.2 (a) et (b) (p.39). Les résultats démontrent que le profil de vitesse change à mesure que la dimension du jeu en bout d'aube varie. En effet, le profil est similaire à celui d'une couche limite laminaire pour les très petites dimensions de jeu alors qu'il évolue vers un profil similaire à une couche limite turbulente pour les jeux d'aubes plus grands. L'influence de la dimension du jeu sur la contribution de l'écoulement de jeu à l'énergie cinétique de turbulence a également été analysée afin de supporter les résultats précédents. Les résultats calculés sont présentés à la Figure 4.3 (p.40) et suggèrent que la contribution de l'écoulement de jeu à l'énergie de turbulence augmente rapidement à mesure que la grandeur du jeu augmente avant de se stabiliser une fois que l'écoulement de jeu est devenu complètement turbulent. Ces observations supportent donc la transition du profil de vitesse, de laminaire à turbulent, telle que discutée précédemment.

À partir de ces résultats, la variation du coefficient « k » en fonction de la dimension du jeu peut être anticipée en se basant sur la transition du profil de vitesse. Le paramètre « k » a été définit par Thomassin *et al*. (2008, 2009) comme étant le rapport U_{tip}/U_F qui peut également s'écrire, pour un écoulement plus général, comme étant le rapport entre la vitesse maximale et la vitesse moyenne de l'écoulement, soit U_{max}/U_{moyen}. Ce rapport est typiquement de 2 pour un écoulement laminaire non-visqueux, autour de 1.5 pour un écoulement à profil parabolique (visqueux) et environ de 1.16 pour un écoulement turbulent. La valeur de « k » devrait donc suivre ces valeurs à mesure que le profil de vitesse évolue lorsque la grandeur du jeu augmente, suivant la transition du profil de vitesse observée précédemment. Une corrélation, basée sur un profil de tangente inverse, a donc été proposée à l'équation (4.3) en page 41 pour modéliser les variations de « k » qui ont été observées d'après les résultats numériques.

Effet de la grandeur du jeu sur k.

L'ensemble des résultats numériques obtenus sur l'effet de la dimension du jeu sur « *k* » sont présentés à la Figure 4.5 (a) (p.43). La corrélation proposée précédemment a été ajustée aux données (moyennées pour les différentes vitesses simulées) et est présentée à la Figure 4.5 (b). Les différents cas de NSV rapportés dans la littérature sont également montrés sur le graphique pour fins de comparaison. Le modèle de corrélation proposé concorde très bien avec les différents résultats disponibles dans la littérature. La corrélation, ajustée aux résultats numériques, semble cependant tendre vers ~1.2 pour des jeux très grands alors que selon l'analogie de la transition du profil de vitesse discutée précédemment, cette valeur devrait être plutôt 1.16. Une explication possible pour cet écart est la distorsion du profil de vitesse dans l'écoulement de jeu près du bord d'attaque, due à la croissance de la zone de séparation en bord d'attaque à mesure que la grandeur du jeu augmente. Des exemples de profils ayant subit une distorsion sont illustrés à la Figure 4.6 (a) (p.44). Également, les profils de vitesses ayant subit une distorsion ont été majoritairement observés pour la géométrie subsonique, qui présente un ratio épaisseur/longueur de corde plus grand. Ceci a pour effet d'accentuer la présence d'un « vena-contracta » tel qu'illustré à la Figure 4.6 (b) puisque la couche limite a plus de temps pour se développer sur une épaisseur d'aube plus grande par rapport à la grandeur du jeu. Ces facteurs peuvent donc contribuer à la distorsion des profils de vitesses pour les grandes dimensions de jeu en bout d'aube est ainsi biaiser la valeur de « *k* » calculée.

Effet de la température sur k.

Les résultats de l'effet de la température sur « *k* » sont présentés à la Figure 4.7 en page 45. Ces derniers montrent une pente croissante de la valeur de « *k* » en fonction de la température, qui est également similaire aux résultats obtenus expérimentalement par Thomassin *et al*. (2008). La plage de température couverte par les simulations corresponds à la moitié d'une enveloppe de conception typique d'un moteur à turbine. Les résultats démontrent que, malgré la faible variation de « *k* » avec la température, l'effet de la grandeur du jeu sur « *k* » est clairement dominant. Les variations de « *k* » avec la température peuvent donc être négligées pour des fins de conception. Ainsi, la corrélation proposée précédemment pour la variation de « *k* » en fonction de la grandeur du jeu peut être utilisée, à l'aide du modèle de NSV proposé par Thomassin *et al*. (2008,2009),

dès les toutes premières étapes de conception des aubes afin d'éviter les NSV dans la plage d'opération du compresseur.

Application du modèle proposé aux prédictions de vitesses critiques de NSV.

La corrélation proposée précédemment pour « k » a été utilisée dans l'équation proposée par Thomassin *et al*. (2008) (équation (2.5), p.17) afin de prédire les vitesses critiques de NSV observées pour certains cas disponibles dans la littérature. Les résultats obtenus sont présentés à la Table 4.1 (p.46). Les prédictions suivant les valeurs de « k » déterminées à l'aide de la corrélation proposée sont toutes en dessous de ~2% d'erreur par rapport aux vitesses critiques de NSV observées. L'approximation générale k=2 (Thomassin *et al*., 2009) donnent des erreurs jusqu'à ~20% pour les mêmes prédictions. La corrélation proposée augmente donc considérablement la précision des prédictions des vitesses critiques de NSV à l'aide du modèle proposé par Thomassin *et al*. (2008,2009).

Remarques sur l'aspect générique de la présente étude.

Tel que mentionné précédemment, les simulations numériques conduites par la présente étude ont été effectuées à l'aide de deux géométries distinctes dans l'espoir de conférer une approche générique aux travaux. Les résultats obtenus pour les deux géométries ont démontrés les mêmes tendances, et ce malgré leurs différentes caractéristiques aérodynamique, notamment au niveau du coefficient de pression (dont celui de la géométrie subsonique était près du double de celui de la géométrie transsonique), tel qu'illustré à la Figure 4.8 (p.47). Une relation analytique a été obtenue, basée sur le modèle de l'écoulement de jeu proposé par Storer et Cumpsty (1991), afin de solidifier davantage le caractère générique de cette étude. La relation obtenue suggère que le paramètre « k » serait inversement proportionnel à la racine carrée du coefficient de pression (ψ), tel que définit par l'équation (4.8) (p.49). Cette relation est tracée graphiquement à la Figure 4.9 (a) (p.49) et démontre que la variation de « k » par rapport à ψ devrait être minimisée à charge aérodynamique élevée puisque la pente tant vers zéro dans de telles conditions (voir Figure 4.9 (b)). Un bref échantillonnage de données disponibles dans la littérature a été effectué afin d'obtenir des valeurs typiques de charge aérodynamique observées près du décrochage pour diverses géométries de compresseurs. Les résultats sont présentés à la Figure 4.10 (p.50). Suivant la relation proposée à l'équation (4.8) et les données obtenues de la littérature, le paramètre « k » démontre une quasi-invariance à charge aérodynamique (ψ) élevée. Ces observations suggèrent

donc que la corrélation proposée précédemment pour « k » en fonction de la grandeur du jeu devrait être générique et ainsi s'appliquer directement à diverses géométries d'aubes, à des fins de conception.

Chapitre 5 : Conclusions.

Conclusions et contributions.

La contribution majeure découlant des travaux présentés dans cet ouvrage est la corrélation proposée pour le paramètre « k » en fonction de la grandeur du jeu, qui améliore considérablement les prédictions de vitesses critiques des NSV à l'aide du modèle proposé par Thomassin *et al.* (2008, 2009). En outre, les principales conclusions sont :

1. Les résultats des simulations numériques ont démontrés que le coefficient de transport de l'instabilité en bout d'aube (k), utilisé dans la prédiction des vitesses critique de NSV, varie avec la grandeur du jeu et la température d'opération. La contribution majeure semble provenir de la variation de la grandeur du jeu alors que l'effet des variations de températures peut être négligé à des fins de conception.
2. Une corrélation a été proposée afin de modéliser la variation du paramètre « k » en fonction de la grandeur du jeu. La corrélation a été ajustée aux résultats numériques obtenus et utilisée afin de prédire les vitesses critiques de NSV des cas disponibles dans la littérature. Les prédictions utilisant la corrélation proposée pour « k » ont été observées entre 0.22% à 2.22% d'erreur par rapport aux vitesses critiques rapportées. Les mêmes prédictions utilisant l'approximation générale k=2 (Thomassin *et al*, 2009) ont données des erreurs entre 1.96% et 19.81%.
3. Le caractère générique de l'étude a également été démontré à l'aide d'une formulation analytique de la variation de « k » en fonction de la charge aérodynamique (ψ). La relation proposée a été également comparée aux données disponibles dans la littérature et montre que, à charge aérodynamique élevée, la variation de « k » par rapport à ψ peut être négligée à des fins de conception.

Recommandations pour travaux futurs.

Simulations numériques couplées – Éléments finis et Mécanique des fluides.

Les travaux de Drolet *et al*. (2009) résumés au chapitre 2 et disponibles en annexe 2 ont été réalisés à l'aide d'une approximation de la forme du mode de l'aube et du déplacement en bout d'aube puisque les simulations considéraient seulement la mécanique des fluides associée au modèle de NSV proposé par Thomassin *et al*. (2008, 2009). Malgré que les fluctuations de pressions aient permis d'identifier les vitesses critiques de NSV à partir du modèle numérique, l'amplitude des fluctuations de pression en bout d'aube ne correspondaient pas à celles observées expérimentalement par Thomassin *et al*. (2008). Par conséquent, des simulations de mécanique des fluides couplées à un modèle d'éléments finis, permettant d'obtenir la forme exacte du mode ainsi que les niveaux de stress associés aux aubes, pourraient possiblement calculer les bonnes amplitudes de fluctuations de pressions. De plus, ce type de simulations pourrait également approfondir les connaissances du modèle proposé par Thomassin *et al*. (2008, 2009) en réunissant l'interaction fluide-structure en entier dans une même simulation.

Possibilité de NSV en conditions d'étranglement du compresseur.

Les NSV sont typiquement observées en conditions de décrochage du compresseur, tel que discuté au chapitre 2. Le modèle de NSV proposé par Thomassin *et al*. (2008, 2009) stipule à cet effet que l'écoulement de jeu évolue tangentiellement lorsque que la charge aérodynamique est élevée de sorte qu'il agit tel un jet impactant sur l'aube adjacente. Cependant, la présence du choc dans le passage principal en condition d'étranglement pourrait réunir les conditions requises afin d'obtenir un jet impactant provenant de l'écoulement de jeu. Les simulations conduites pour l'étude décrite dans le présent ouvrage ont alors été utilisées pour simuler des conditions près de l'étranglement du compresseur. Un exemple de résultats obtenus est présenté à la Figure 5.1 (p.56). Les résultats démontrent qu'en conditions d'étranglement, le profil de V_L (Figure 5.1 (a)) a la forme du jet tel qu'observé au chapitre 4, cependant en deux parties, séparées par le choc. La partie située derrière le choc a suffisamment d'énergie comparativement à l'écoulement principal en bout d'aube de sorte que l'écoulement de jeu impact sur l'aube adjacente près du bord de fuite (Figure 5.1 (b)). Cette configuration réunit donc les conditions nécessaires afin d'observer les NSV en condition d'étranglement du compresseur. Il serait alors intéressant de conduire une série d'expériences à l'aide d'un compresseur ayant connu des NSV près du décrochage afin d'étudier la configuration suggérée en condition d'étranglement.

TABLE OF CONTENT

LIST OF TABLES

LIST OF FIGURES

INITIALS AND ABBREVIATIONS

A	Blade tip displacement amplitude [m]
c	Local speed of sound [m/s]
C_a	Mean axial velocity [m/s]
CFD	Computational Fluid Dynamics
C_p	Specific heat at constant pressure [kJ/(kg-K)]
D	Diameter [m]
EO	Engine Order (1,2,3,...)
f	Frequency [Hz]
FIV	Flow-induced vibrations
FOR	Frame of reference
h	Tip clearance size [m]
k	Tip instability convection coefficient (U_{tip}/U_F)
L	Length or distance [m]
LE	Leading edge
M	Mach number
n	Harmonic integer number
N	Rotational speed [rpm]
NSV	Non-Synchronous Vibrations
p’	Pressure fluctuation, unsteady pressure [Pa]
PIV	Particle Image Velocimetry
PR	Pressure ratio
PS	Pressure side
R_s	Specific gas constant [kJ/(kg-K)]

RI	Rotating Instabilities
s	Blade pitch (inter-blade) distance [m]
S’	Vibration level [Pa]
SS	Suction side
S_t	Strouhal number (reduced or non-dimensional frequency)
T	Torsional vibration mode, Temperature [K]
TE	Trailing Edge
U	Flow velocity [m/s]
U_{tip}	Blade tip velocity [m/s]
U_F	Foward wave (jet) speed [m/s]
V_L	Tip leakage flow velocity [m/s]
W	Air mass flow [Kg/s]
W_{corr}	Corrected air mass flow ($W_{corr} = W*\sqrt{[(T/T_{ref})/(P/P_{ref})]}$) [Kg/s]

Greek symbols

α	Absolute air flow angle [deg.], Correlation coefficient
β	Relative air flow angle [deg.], Correlation coefficient
γ	Specific heat ratio
η	Compressor efficiency
θ	Temperature ratio (inlet temperature/reference temperature) [T_1/T_{ref}]
λ	Wave length [m]
μ	Dynamic viscosity [Pa.s]
ξ	Hub-to-tip ratio
ρ	Fluid density [Kg/m^3]

σ	Tip solidity (ς_{tip}/s)
ς	Chord length [m]
τ	Non-dimensional tip clearance ($\tau = h/\varsigma_{tip}$)
φ	Flow coefficient
ψ	Loading coefficient, pressure coefficient
ω	Angular frequency [rad/s]

Subscripts

0	Local, total
b	Blade
B	Backward wave in rotating frame
c	Speed of sound, critical
D	Diameter [m], Design
F	Forward wave in rotating frame
h	Hub
j	Jet
max	Maximum
min	Minimum
t or tip	Blade tip

LIST OF APPENDICES

CHAPTER 1 INTRODUCTION

The gas turbine industry has been one of the few technological sectors that have shown continuous and sustained research and development since its early debut in the mid 1900's. Nowadays, modern gas turbine companies are pushing the design to the limits in terms of thrust-to-weight ratio and specific fuel consumption, in order to thrive in the competitive market. This war on weight has led to new challenge in terms of vibrations of the diverse gas turbine engine components. Being able to understand and master the numerous vibration phenomena, often associated with fatigue damage of components, thus represents a tremendous competitive advantage on the market. The current work will focus on vibrations encountered in the axial compressor module found in modern gas turbine engines, more specifically, Non-Synchronous Vibrations (NSV). Although some relevant details on compressor will be given, it will be assumed throughout this work, that the reader has some basic knowledge on the subject.

1.1 Review on Axial Flow Compressors

1.1.1 Flow Features and Operating Principle

An axial compressor involves two main components, the rotor that accelerates the flow and that is essentially made of a disc with a number of airfoils, referred to as "blades", which rotates confined within a casing. The second main component is the stator, that converts the kinetic energy into static pressure rise, and is also made of a disc with airfoil sections but that are fixed with respect to the rotor. Typically, many stages are required to achieve the desired pressure rise through the compressor module. An illustration of a typical compressor stage (rotor and stator) assembly is shown for reference in Figure 1.1. This configuration leads to an important and widely studied aspect of compressor aerodynamics, namely the tip clearance flow, which is the air that flows through the spacing between the rotor blade tip and the casing, as shown also in Figure 1.1. Typically, the tip clearance size in commercial gas turbine engine is on the order of 1% of the blade tip chord.

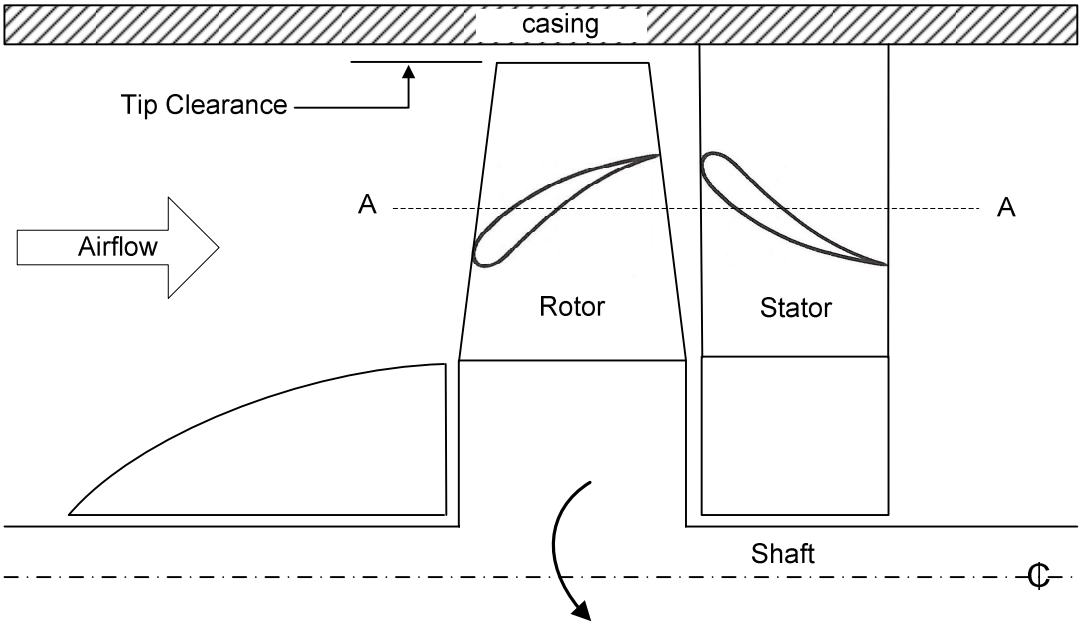

Figure 1.1 : Typical axial compressor stage configuration

Figure 1.2 shows the typical flow features of an axial compressor stage. The velocity triangles are used to determine the magnitude and direction of velocity vectors through the stage. The velocity component and direction in the blade frame of reference are denoted V and β, respectively, while the velocity component and direction in the absolute frame of reference are identified by C and α, respectively. The subscripts 1, 2 and 3 are referring to the inlet, mid-stage and outlet locations, respectively. In addition, C_a is the axial velocity component and U is the rotor blade speed at a given radial location.

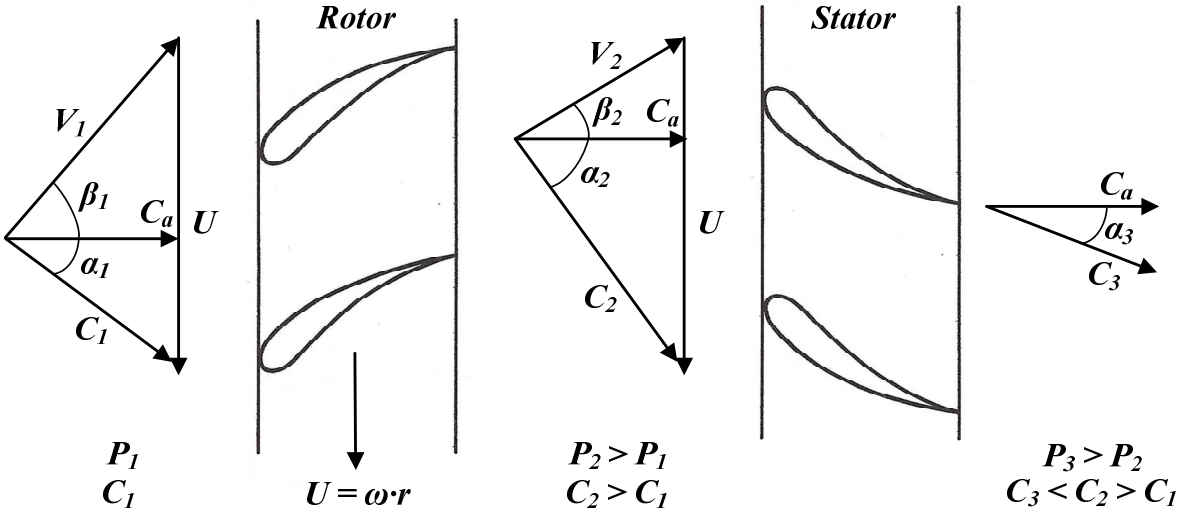

Figure 1.2 : Flow features of a typical axial compressor stage (rotor and stator)

The operating principle of an axial compressor was briefly described previously. As shown in Figure 1.2, the rotor accelerates the air while providing some static pressure increase, resulting in $P_2>P_1$ and $C_2>C_1$. The air then flows through the stator where the kinetic energy of the fluid is converted into static pressure rise, by deceleration of the flow, which results in $P_3>P_2$ and $C_3<C_2>C_1$. The fraction of static pressure rise provided by the rotor, when compared to the total pressure rise in the stage, is called the "degree of reaction" and is typically on the order of 0.5. This means that the rotor and stator are sharing approximately half of the static pressure increase through the stage.

1.1.2 Performance and Characteristics

The performance of axial compressor is typically characterized in terms of pressure ratio and efficiency. Figure 1.3 (a) shows a "compressor map" which is a plot of the stage pressure ratio versus the corrected mass flow. The surge line identified on the figure corresponds to the point of compressor stall or reverse flow while the operating line corresponds to the operating point of maximum efficiency. The speed lines are also identified which are points along a constant corrected speed ($N/\sqrt{\theta}$) and are shown as a fraction of the design speed in the figure. Figure 1.3 (b) shows the isentropic efficiency, also plotted as a function of the corrected mass flow where the point of maximum efficiency are identified and corresponds to the operating line points on Figure 1.3 (a).

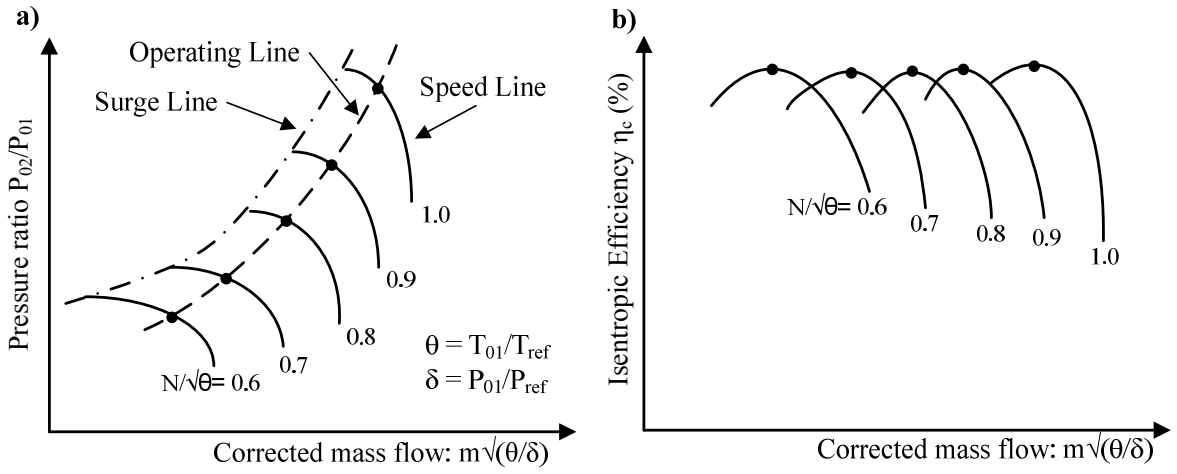

Figure 1.3 : Axial compressor characteristics, a) Pressure ratio and b) Efficiency vs corrected mass flow

1.1.3 Tip Clearance Flow Features

As it was previously mentioned, the typical configuration of axial flow compressors leads to an intrinsic feature of compressors: the tip clearance flow. The tip clearance flow is an air flow that is pressure driven (aerodynamic loading) which flows through the spacing between the rotor blade tip and the casing, as previously depicted in Figure 1.1. The principal features and characteristics of the tip clearance flow are shown in Figure 1.4 (Vo, H.D., 2001), for high aerodynamic loading conditions. In such conditions, the high incidence of the incoming flow leads to flow separation near the blade tip which creates a vortex, called the "tip clearance vortex", that is the results of fluid mixing between the separated flow and the tip clearance flow. This also leads to a passage blockage that increases in size as the aerodynamic loading increases.

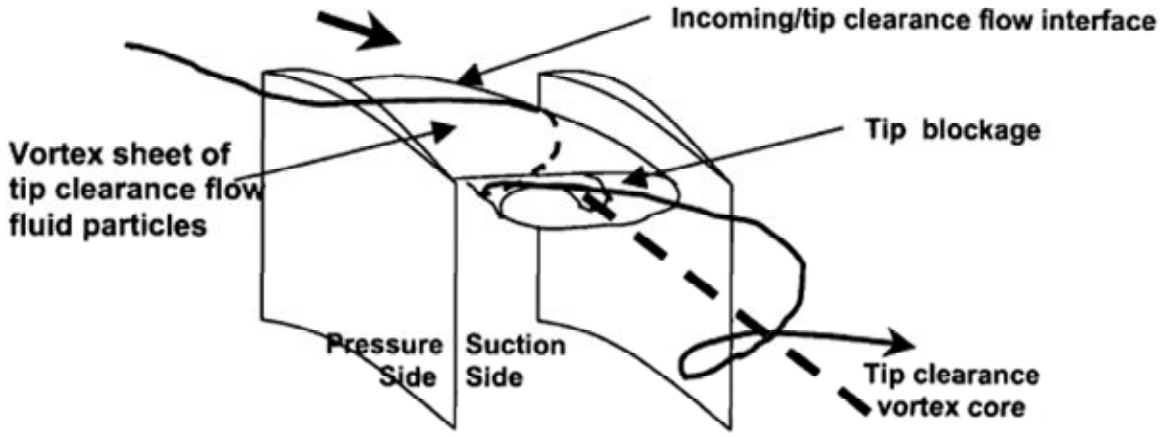

Figure 1.4 : Basic tip clearance flow features (Vo, H.D., 2001)

Figure 1.5 also depicts the behavior of the tip clearance flow as the aerodynamic loading is increased. In Figure 1.5 (a), a region of moderate aerodynamic loading, located just before peak efficiency or operating line, is circled by a dashed line. In such conditions, the tip clearance vortex is relatively small in size, as shown in Figure 1.5 (b), since the angle of incidence of the incoming flow is moderate. In addition, the tip vortex is redirected in the stream-wise direction by the high momentum incoming flow. In conditions of high aerodynamic loading, such as in conditions near stall as shown in Figure 1.5 (c), the angle of incidence of the incoming flow at the blade tip is such that the tip vortex is now bigger in size. It has more momentum than the incoming flow in the tip region such that it evolves tangentially and eventually travels across the passage and impact on the upcoming blade, as illustrated in Figure 1.5 (d). In some cases, the tip vortex is divided in two distinct portions, which are no longer “vortex” (strictly speaking), as a vortex core cannot usually be identified. This is also identified in Figure 1.5 (d) where a portion of the broken tip vortex follows the first blade suction side while another follows the upcoming blade pressure side.

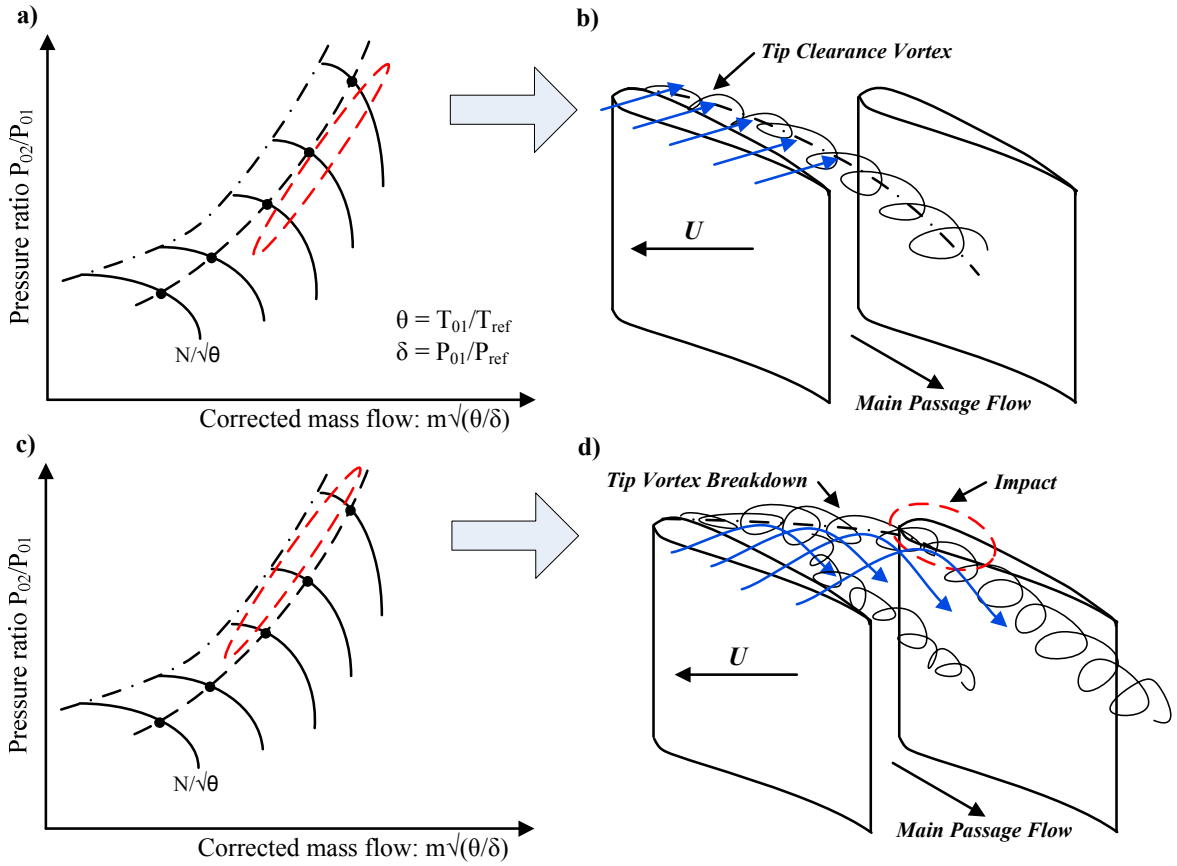

Figure 1.5 : Characteristics of the tip clearance flow at moderate aerodynamic loading in (a) and (b) and high loading near stall in (c) and (d)

1.2 Vibrations in Axial Flow Compressors

Compressors are prone to vibrations which are generally categorized as mechanical vibrations, originating from mechanical interaction among the diverse engine components, and flow-induced vibrations (FIV) that are often the result of a fluid-structure interaction between the rotor blades and the air flow through the compressor. The flow-induced vibration category is typically divided in two distinct sub-categories, which are “forced response” and “fluid-elastic instabilities”. The latter includes classical flutter and non-synchronous vibrations (NSV). The various types of vibrations are depicted on the Campbell diagram, shown here in Figure 1.6, which is the tool that is typically used to consider vibration sources in compressor design. The latter has on the abscise axis, the rotational speed of the rotor shaft, and on the ordinates axis, the frequency of excitation. The natural frequency modes of the blade are plotted, on the Campbell diagram, as a function of the rotational speed and show a slightly positive slope due to the inertial force that increases as

the speed increase, which changes the blade stiffness resulting in a change in the blade natural frequency.

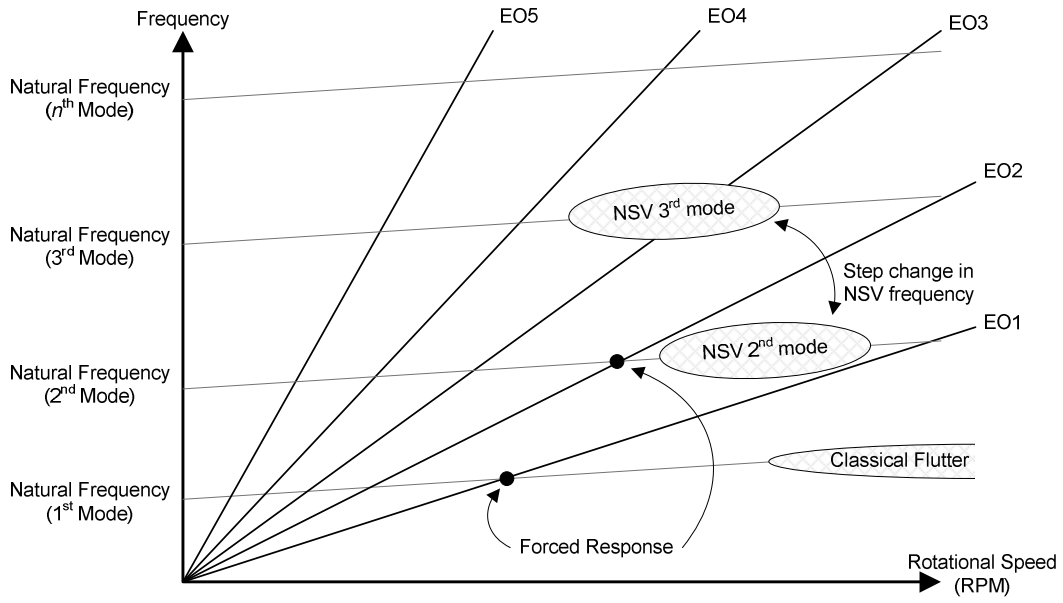

Figure 1.6 : Different vibration types depicted on the Campbell diagram

The forced response vibrations are the most typical vibrations sources in compressors and are known to be "synchronous" with the rotational speed of the shaft. This means that the frequency of excitation will be an integral multiple of the frequency of the rotational speed, known as "engine order" (EO). Typical sources of EO forced excitation are the blade wakes of the upstream blade row as well as the potential excitation of the downstream blade row. Coincidence of the frequency of excitation with one of the blade mode will results in a forced vibration of the blade. Unevenly distributed wakes coming from the stator can also results in sub- or super-harmonics of the engine order, resulting in 2EO, 3EO, etc excitation frequencies.

The fluid-elastic vibrations, on the other hand, are not necessarily synchronous with the rotor speed, as opposed to forced vibrations. A typical type of fluid-elastic instability that is of major concern in compressor design is known as "flutter". Classical flutter is the most common and understood type of flutter and consist of exponentially growing vibrations when the "flutter speed" is reached; meaning that the only way out of classical flutter is to go down in rotor speed below the flutter speed. This is very distinctive from NSV which occurs through a resonance despite that both phenomena can occur at non-integral multiple of the rotor speed. In addition,

many different types of flutter have been reported in the industry (Dowell, E.H., Crawley, E.F., Curtiss Jr, .H.C., Peters, D.A., Scanlan, R.H. and Sisto, F., 1995) and have often been a source of confusion with NSV. This is also why NSV cases have been vaguely reported in the last 15-20 years.

1.3 Research Objectives

Thomassin, J., Vo, H.D. and Mureithi, N.W. (2008, 2009) have proposed a mechanism and a model to explain the physics behind NSV. The latter was statistically and experimentally proven to be a powerful tool to predict the critical rotor speed at which NSV are likely to occur. However, the model was found very sensitive to what was defined as the "instability convection coefficient" (k) by Thomassin *et al*. (2008). In fact, the initial approximation of k=2 in the model (Thomassin *et al*., 2009) also showed significant error (up to ~20%) in the NSV predictions, which can only be improved by complex experimental measurements to determine the actual "k", as performed by Thomassin *et al*. (2008). The general objective of the research work described herein is to use computational fluid dynamics (CFD) to improve the NSV prediction model and extend our comprehension of the physics behind NSV. More specifically, the objectives are:

1. Estimate the "k" parameter from numerical simulations and determine how the tip clearance size and operating temperature affect its value.
2. Propose a correlation for "k" that can be used as a complementary tool to the NSV model proposed by Thomassin *et al*. (2008, 2009) such that the critical NSV speeds can be assessed in the very early design stage, independently from numerical simulations and experiments.
3. Assess the generic nature of the study by looking at the relevant fluid mechanics and aerodynamic characteristics of axial compressors and address the possibility to encounter NSV in choked-flow conditions, as opposed to the near-stall region where NSV are known to occur.

1.4 Thesis Organization

A brief introduction on compressor vibrations and the main objectives of the current work were presented in the introduction of chapter 1. Chapter two presents an historical background and literature review on NSV, along with a detailed description of the NSV model proposed by Thomassin *et al*. (2008, 2009). The relevant details of the work from Drolet *et al*. (2009) that led to the present thesis are also summarized in chapter 2. Chapter 3 describes the details of the methodology used for the current work. Chapter 4 presents the results of simulations that were conducted to assess the effect of tip clearance size and operating temperature on the k parameter involved in the critical NSV prediction model of Thomassin *et al*. (2008) (specific objective 1). It also proposes a correlation for k, based on the numerical results, that improves the critical NSV speed predictions using the proposed model and discusses the generic nature of the study (specific objective 2 and part of specific objective 3). Chapter 5 summarizes the main conclusions and contributions of the work described herein and also discuss on recommendations for future work, based on the results and observations presented in the current thesis (specific objective 3).

1.5 Research Contributions

This study proposes a correlation for the instability convection coefficient (k) that significantly improves the critical NSV speed predictions. The proposed correlation was also proven to be generic for any given compressor geometry. In addition, this work suggests a possible configuration for NSV to occur in choked-flow conditions as a recommendation for future work.

CHAPTER 2 LITERATURE REVIEW

This chapter presents a literature review on Non-Synchronous Vibrations (NSV) observed in axial flow compressors. First, an historical background on the subject is presented along with main contributions from previous research work. Secondly, a model that was proposed to predict the critical blade tip speed at which NSV can occur is presented in greater details since the current thesis builds upon this specific work. Finally, a numerical method that was developed to refine the critical NSV speed predictions is presented as the current research is also a direct continuation from this previous numerical work.

2.1 Background on Non-Synchronous Vibrations

One of the first reported NSV cases in the industry is attributed to Baumgartner M., Kamaler F. and Hourmouziadis J. (1995). They have linked NSV with rotating instabilities (RIs) from experimental observations. Rotating instabilities can be described as an oscillating flow phenomenon that causes periodic vortex separation and axial reverse flow in the tip clearance region (Mailach *et al*., 2001a) and were widely studied in the past as a possible excitation source for compressor blades. Examples can be found in Liu, J.M., Holste, F., Neise, W., 1996; Kameier, F. and Neise, W., 1997a; Kameier, F. and Neise, W., 1997b; Mailach, R., Lehmann, I. and Vogeler, K., 2001a; Mailach, R., Sauer, H. And Vogeler, K., 2001b; März, J., Hah, C. and Neise, W., 2002. RIs were associated with high amplitude vibrations and noise generation on compressor rotor blades. They were also modeled as a noise source or pressure fluctuation ($p=p(t)$), as shown in Figure 2.1, emanating from the leading edge tip vortex, possibly linked with NSV.

In fact, an interaction between the leading edge tip vortex and the adjacent blade was found by März *et al.* (2002), Fukano, T. and Jang, C.M. (2004) and Zhang, H., Lin, F., Chen, J., Deng, X. and Huang, W. (2006). Figure 2.1 depicts the different models that were proposed for rotating instabilities by a) Baumgartner *et al*. (1995) and b) Mailach *et al*. (2001). Kameier and Neise (1997a) have also found a Strouhal number (reduced frequency) for rotating instabilities that was function of the tip clearance and aerodynamic loading. This Strouhal number was later refined by Mailach *et al.* (2001) and found to be a constant at given flow conditions and blade geometry.

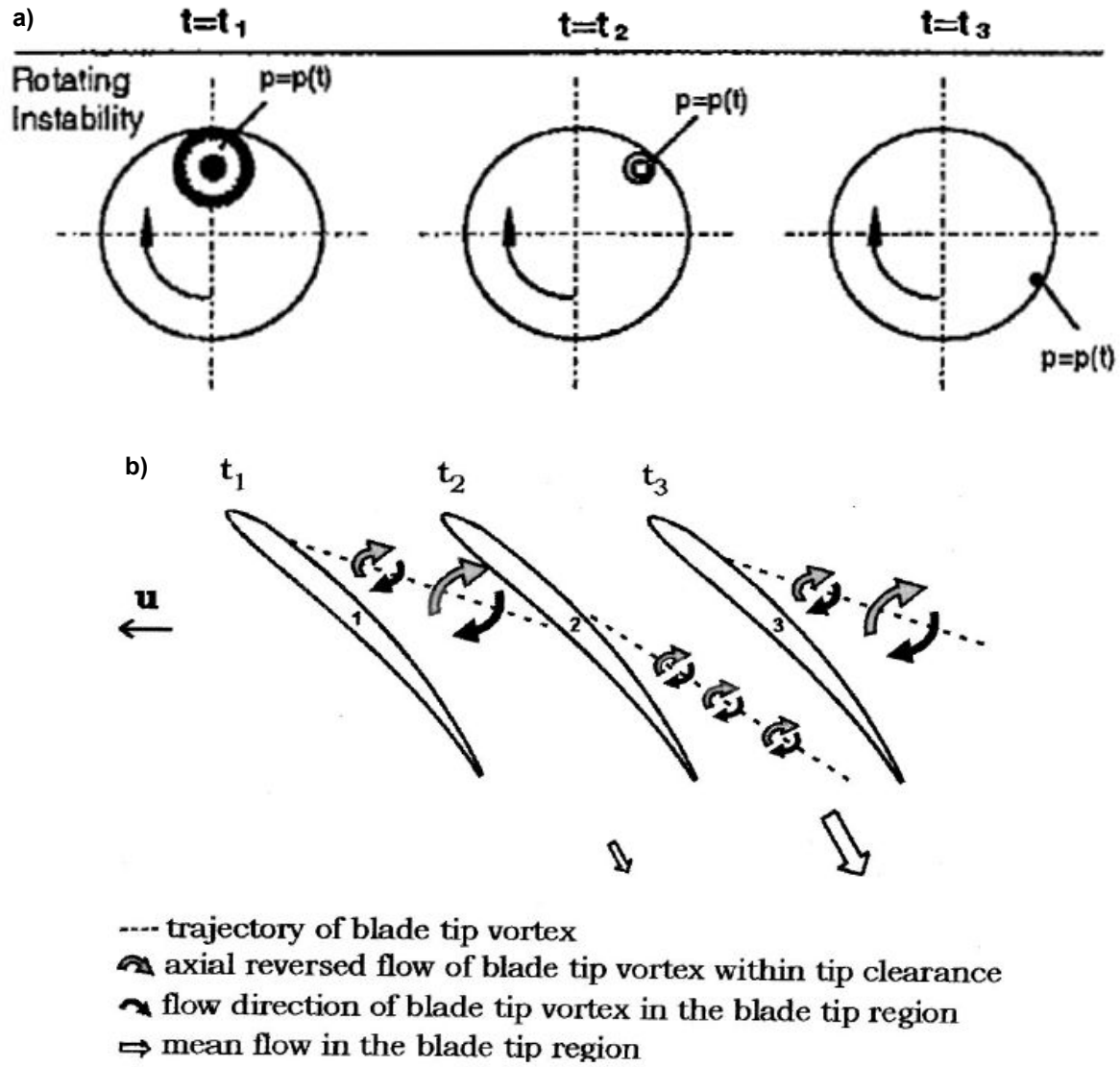

Figure 2.1 : Models proposed for rotating instabilities (RI) by a) Baumgartner *et al.* (1995) and b) Mailach *et al.* (2001)

It was not before 2003 that rotating instabilities, similar to that studied by Baumgartner *et al.* (1995), were named "non-synchronous vibrations" (NSV) by Kielb, R.E., Thomas, J.P., Barter, J.W. and Hall, K.C. (2003) who experimentally identified the effect of operating conditions, such as temperature, on NSV and linked it with tip clearance flow instabilities through numerical simulations. They have also observed a sudden step change in the frequency mode associated with NSV, for constant operating conditions, which is one of the most distinctive features of NSV. Later, Vo, H.D. (2006) found that the trailing edge backflow of tip clearance fluid, which is

one of the criteria for spike-initiated rotating stall (Vo, H.D., Tan, C.S. and Greitzer, E.M., 2008), showed signs of impingement on the upcoming blade, as shown in Figure 2.2 (a). This phenomenon occurs near stall and thus, at high aerodynamic loading. These observations were also experimentally observed later by Deppe, A., Saathoff, H. and Stark, U. (2005). Vo, H.D. (2006) also suggested, based on his observations, that the dynamics of impinging jets could possibly explain the underlying physics behind NSV.

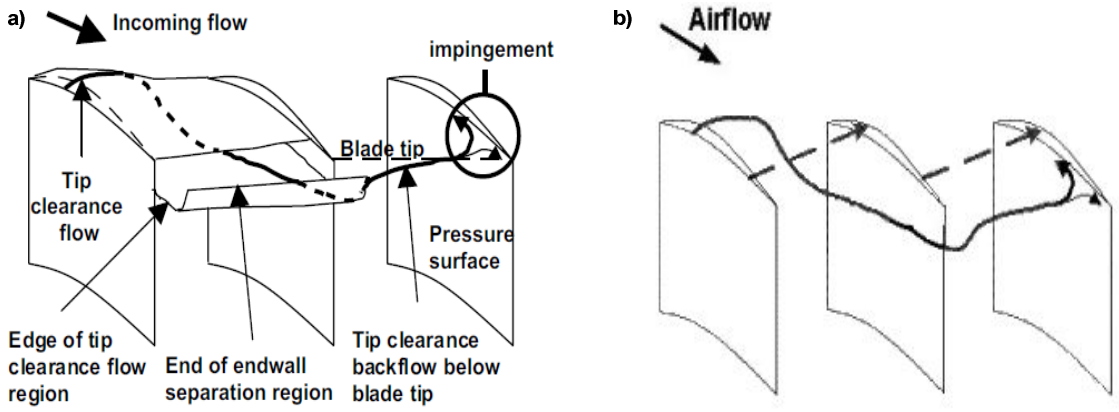

Figure 2.2 : Proposed tip clearance flow impingement patterns, possibly the physical mechanism behind NSV, from a) Vo (2006) and b) Thomassin *et al*. (2008)

2.2 Proposed Theory on Non-Synchronous Vibrations

In light of the proposed impinging jet analogy, Thomassin, J., Vo, H.D. and Mureithi, N.W. (2009) have reviewed the dynamics of impinging jets in order to explain the physics behind non-synchronous vibrations. They developed a novel theory for resonant impinging jets at Mach numbers of similar magnitude to those typically found in tip clearance flows of axial compressors. Based on their theory, a physics-based model was derived to predict the compressor blade tip speeds at which NSV are most likely to occur (Thomassin *et al*., 2009). The model was also experimentally verified by Thomassin, J., Vo, H.D. and Mureithi, N.W. (2008). The research presented in this thesis builds on previous work from Thomassin *et al.* (2008, 2009). Hence, this section presents their findings in greater details to help the comprehension of the reader throughout the current work.

2.2.1 The Jet Core Feedback Theory

Ho, C.-M. and Nosseir, S. (1981) studied the dynamics of high-speed subsonic jets impinging on rigid flat plates. They found that the shear layer emanating from the jet lip produces vortical structures that are convected at approximately half of the jet velocity and that scales with the jet diameter (D) and mean velocity (U). These turbulent structures create acoustic reflections that propagates outside the jet potential core when impinging on a rigid plate that is located in the jet potential core (typically $L \approx 7\ D$, where here L is the jet-to-plate distance corresponding to the extent of the jet potential core). When the reduced frequency, or Strouhal number ($S_t = fD/U$), reaches a critical value such that the acoustic feedback wavelength corresponds to the jet-to-plate distance, there is a significant amplification of the pressure fluctuation on the plate. In such conditions, the jet is said to be "resonant". Examples of a resonant and non-resonant jet are shown in Figure 2.3 (a). Typically, the lowest Mach number at which a jet can become resonant, when impinging on a rigid plate, was found to be 0.65, as shown in Figure 2.3 (b) from Lucas, M.J. (1997). Although the analogy of a jet impinging on a plate, as proposed by Vo (2006), looked promising, the Mach numbers observed in compressor tip clearance flows are typically lower than M=0.65.

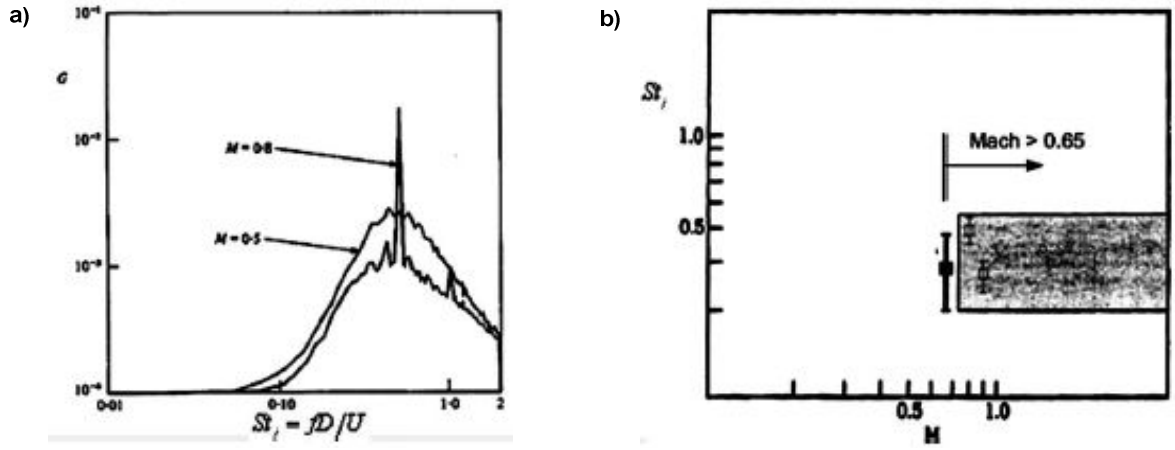

Figure 2.3 : a) Response of a jet impinging on a rigid plate: resonant jet at M=0.8 and non-resonant jet at M=0.5, from Ho *et al*. (1981) and b) reduced frequency (Strouhal number) range for resonant impinging jets (from Lucas, M.J., 1997)

Thomassin *et al*. (2009) have thus revisited the physics of the impinging jet on a flat plate of Ho *et al*. (1981). In their experiment, the plate was flexible and vibrating, to simulate a cantilevered rotor blade, as opposed to Ho *et al*. (1981) where the plate was rigid. The feedback mechanism of the "jet-core feedback theory", proposed by Thomassin *et al.* (2009), is illustrated in Figure 2.4 (a) while Figure 2.4 (b) presents the different flow and geometrical characteristics relevant to the proposed theory. The flexible vibrating (z') plate allowed pressure fluctuations at the stagnation point, in the jet centerline, that created an additional feedback within the jet potential core which travels back at a velocity U_B such that,

$$U_B = c - U \tag{2.1}$$

where c is the local speed of sound. For the jet to become resonant, this implies that the reduced jet frequency must satisfy a condition such that,

$$f = f_B = S_t U / D = U_B / \lambda_B = (c - U) / \lambda_B \tag{2.2}$$

Where f_B is the plate natural frequency and λ_B is the acoustic feedback wavelength. They also found that the jet-to-plate distance (L) for any wavelength should satisfy:

$$L = n \lambda_B / 2 \tag{2.3}$$

where n is an integer that accounts for higher harmonics of the wavelength. This led to the basis of the "jet core feedback theory" proposed by Thomassin *et al*. (2009).

An experimental validation of the proposed theory was performed by Thomassin *et al*. (2009) from which the results are summarized in Figure 2.5 (a) and (b). Figure 2.5 (a) shows the transfer function of the pressure fluctuations measured at the plate with respect to that measured at the jet lip and demonstrates that a jet can become resonant below M=0.65 (for M≈0.37 in this case) when impinging on a flexible plate. Figure 2.5 (b) shows the phase angle of the transfer function presented in Figure 2.5 (a), which also supports the resonance of the jet.

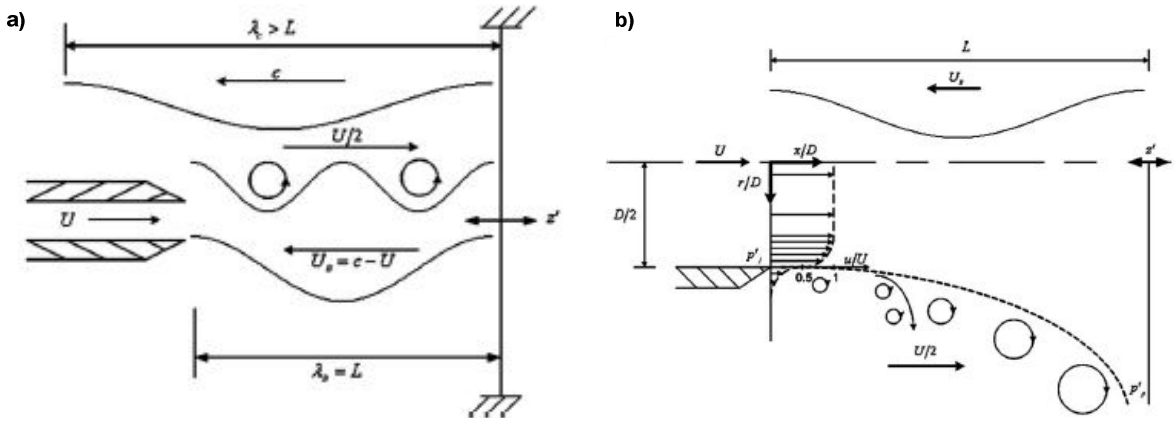

Figure 2.4 : The jet core feedback theory: a) detailed mechanism and b) flow and geometrical characteristics

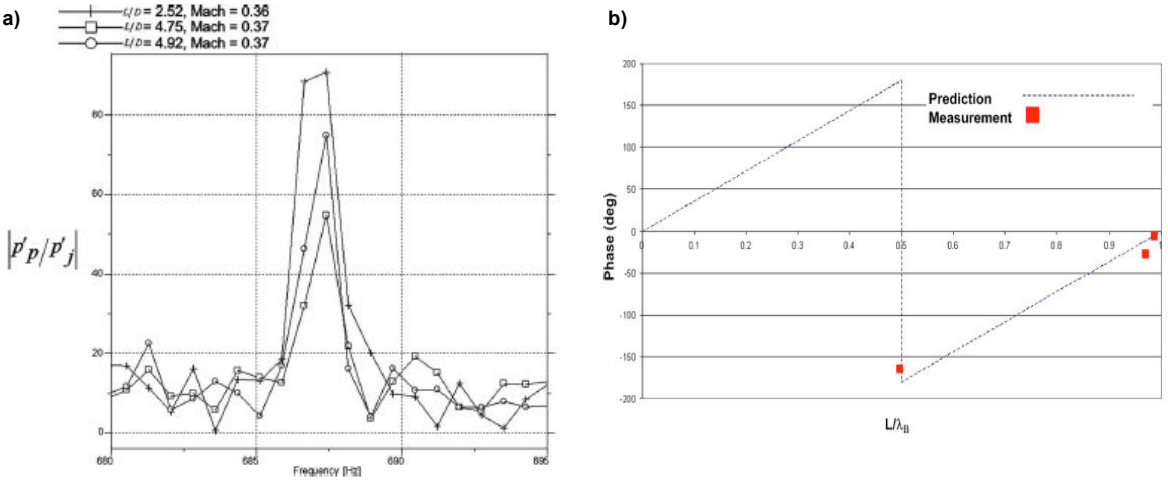

Figure 2.5 : a) Resonant jet impinging on a flexible plate for M≈0.37 at different jet-to-plate distances and b) acoustic feedback (backward wave) phase results of resonant jet, (Thomassin *et al*., 2009)

The jet speeds investigated are also representative of the tangential velocity component present at the blade tip during NSV. Consequently, this novel jet core feedback theory was adapted to compressor blades by Thomassin *et al*. (2008, 2009) as the possible mechanism behind non-synchronous vibrations, as it will be discussed in the next section.

2.2.2 Proposed Model for NSV Prediction

The analogy between the jet-core feedback flow and the compressor blade tip region flow is illustrated in Figure 2.6 (a) and (b) where the jet velocity U_F is now the tip clearance flow velocity. Structurally, the plate corresponds to the vibrating blade, the jet-to-plate distance is the blade pitch, s, and the jet diameter is two times the tip clearance size, h, since the tip clearance flow profile is analogous to half of a jet profile. Thomassin *et al*. (2008) suggested that at particular operating conditions, the resonance of the tip clearance flow, analogous to the impinging jet resonance, could be the physical mechanism behind NSV.

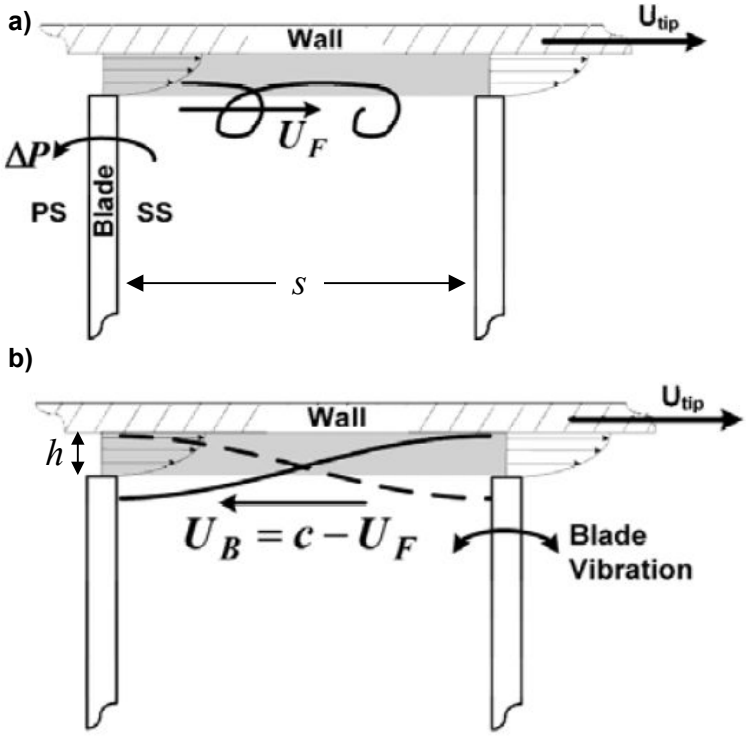

Figure 2.6 : The jet core feedback theory applied to compressor NSV: a) tip clearance flow tangential direction at high blade loading – rotating frame of reference (FOR) and b) acoustic feedback wave propagated upstream in rotating FOR, (adapted from Thomassin *et al*., 2008)

The tip clearance flow resonance can only occur if two main conditions are satisfied. First, the compressor must operate at high aerodynamic loading, such as in conditions near stall, to provide a tangential evolution of the tip clearance flow such that it can act as an impinging jet on the adjacent blades. Secondly, the local speed of sound in the blade tip region must be adequate for

the acoustic feedback from the adjacent blade vibrations to travel back and sychronize the tip shear layer causing instability and resonance of the tip clearance flow. An equation was derived based on this theory (Thomassin *et al.*, 2009), here shown as equation (2.4), to predict the critical rotor speed at which NSV can occur.

$$U_{tip,c} = 2\left(c - \frac{2sf_b}{n}\right) \qquad \text{where } c = \sqrt{\gamma R_s T_{tip}} \tag{2.4}$$

In equation (2.4), U_{tipc} is the critical blade tip speed at which NSV is expected to occur, c is the local speed of sound, s is the blade pitch, f_b is the blade natural vibration frequency and n is an integer related to the harmonics of the acoustic feedback wave, as previously discussed. This equation was statistically verified on a number of cases for which the compressor blades exhibited NSV (Thomassin *et al.*, 2009) and showed good agreement with the available data. Equation (2.4) can also be rearranged in terms of a corrected blade tip speed as a function of the blade frequency. Using $U_{tipc} = k\ U_F$, where k was defined as the tip instability convection coefficient for a more general form of the equation, this leads to

$$\frac{U_{tipc}}{\sqrt{T_{tip}}} = k\left(\sqrt{\gamma R_s} - \frac{2\ s\ f_b}{n\sqrt{T_{tip}}}\right) \qquad \text{where, } k = U_{tip}\ / U_F \tag{2.5}$$

It should be noted that in the early design stages of compressor design, the blade tip radius (r_{tip}), number of blades, blade pitch (s), blade natural frequency (f_b) and blade tip temperature (T_{tip}) are usually known or can be accurately estimated from experience and best practices. Therefore, the only remaining parameter to determine in equation (2.5), to identify the potential NSV conditions, is the "instability convection coefficient" (k). This stresses the need to determine k for a given rotor geometry which is the main objective of the work presented in this thesis.

By using the relation $N[rpm] = (30 \cdot U_{tip})/(\pi \cdot r_{tip})$, it is possible to plot the rotor speed, N, (on the x-axis), using equation (2.5), as a function of the frequency (f) (on the y-axis), given that the flow and geometrical characteristics are known. The resulting application of the model proposed by equation (2.5) is shown on the Campbell diagram in Figure 2.7 and appears as the negative slope lines which can predict the range of possible NSV events for a given operational envelope.

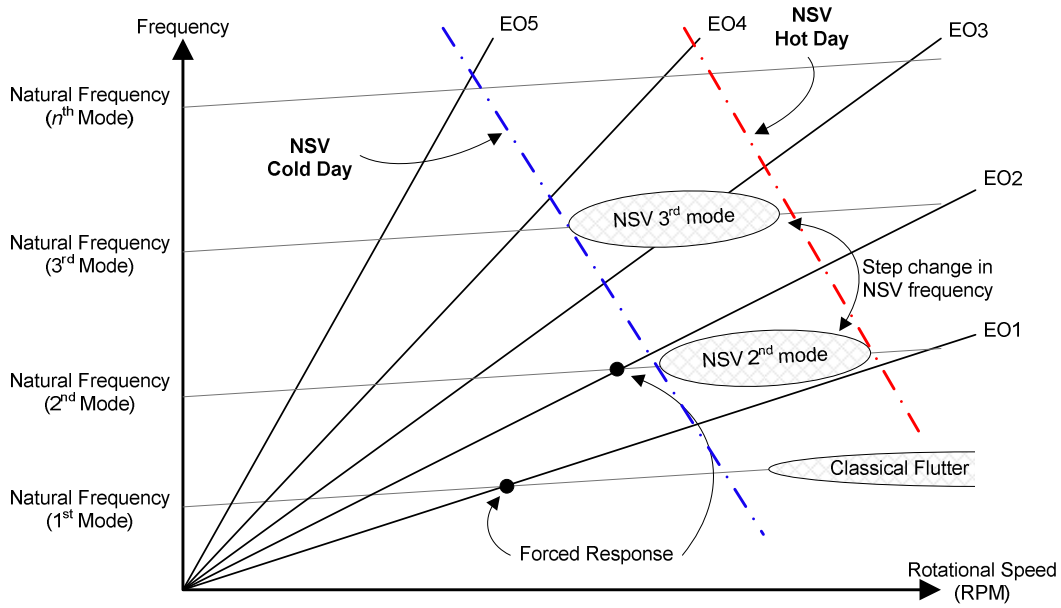

Figure 2.7 : Application of the proposed NSV model on the Campbell diagram

The proposed NSV model was also experimentally demonstrated on a compressor rotor known to exhibit NSV by Thomassin *et al*. (2008). Non-synchronous vibrations were observed for several rotor speeds and operating conditions. A summary of the results and trends observed is shown in Figure 2.8 from Thomassin *et al*. (2008). They have observed increasing NSV amplitudes going up the compressor speed lines as shown, which were referred as pre, mid and peak NSV regions respectively. The critical NSV speed predictions using the general approximation of k=2, as shown in equation (2.4), showed poor agreement (up to ~20% error) for the 2% tip clearance experimental condition. However, the critical NSV blade tip speed predicted by equation (2.5) was improved by a factor up to 10 when the proper value of k was used instead of the general approximation of $U_{tipc} \approx 2U_F$ initially proposed by Thomassin *et al*. (2009).

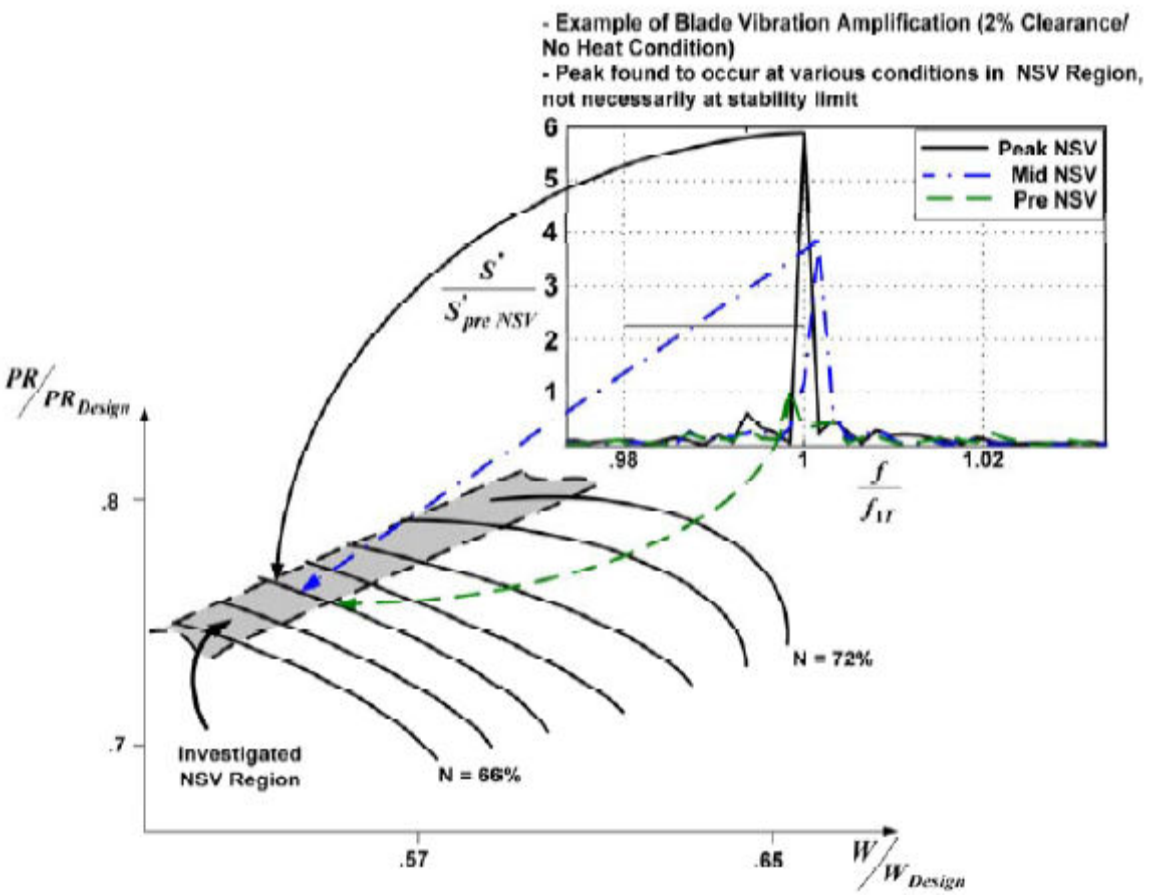

Figure 2.8 : Near stall NSV region and vibration amplification as experimentally observed by Thomassin *et al*. (2008)

Thomassin *et al*. (2008) have then measured the instability convection coefficient (k) using cross-correlation between unsteady pressure probes located on the blade (rotating frame of reference) and on the casing (fixed frame). The idea was to find the time delay (Δt) for 2 pressure fluctuation signals to be correlated. Knowing the distance between the blades and the time that a perturbation took to travel that distance, the convection velocity U_F was calculated. The results are shown in Figure 2.9 from Thomassin *et al*. (2008). Average values of k = 1.96 (cold inlet) and k = 1.85 (heated inlet) were found for the 2% tip clearance, while values of k = 1.67 (cold) and k = 1.73 (hot) were found for the 1% tip clearance case.

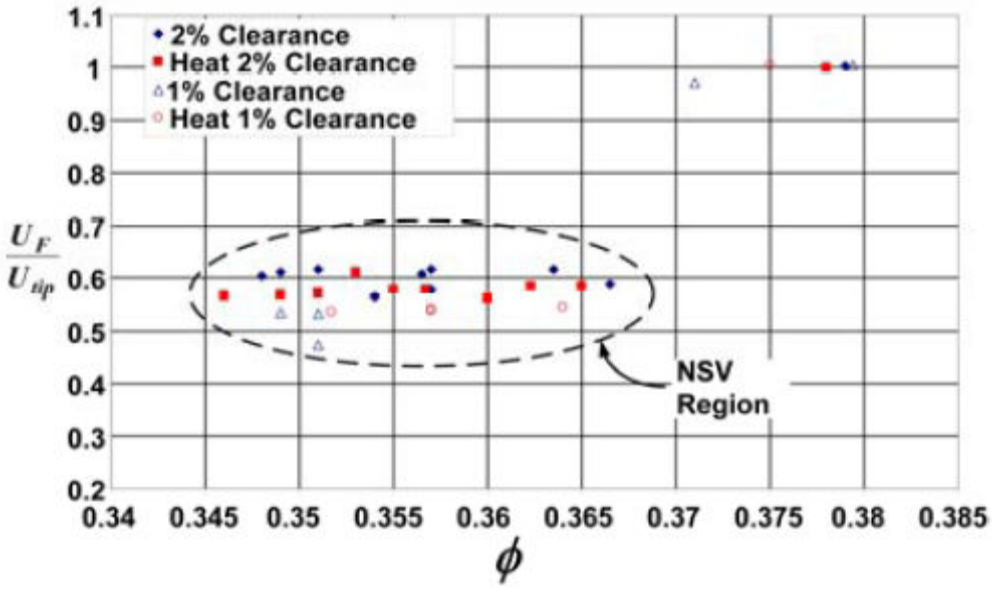

Figure 2.9 : Measured instability convection coefficient (k), Thomassin *et al*. (2008)

The NSV critical tip speeds were found in very good agreement using the measured values of k in equation (2.5). This suggests that, although rough estimates can be found using the approximation of $k = 2$, the exact value of k has to be known for a given rotor geometry in order for the proposed NSV model to yield accurate predictions of the critical NSV speed.

Additional experimental investigation was performed on the rotor used by Thomassin *et al*. (2008), as part of the research work presented in this Thesis, using particle image velocimetry (PIV) to gain further understanding of the proposed NSV mechanism. The details on the design of the experiment, which was based on previous work from Schrapp, H., Stark, U. and Saathoff, H. (2008), along with sample results, are provided in Appendix 1. The results were found to be in agreement with the work of Xianjun, Y., Baojie, L. and Hokang, J. (2003) and suggested that the leading edge tip vortex tends to be tangential and be redirected towards the upcoming blade near stall. This behavior of the tip clearance flow was also observed by Vo *et al*. (2005) as one of the criteria for spike-type stall and was discussed previously in section 1.1.3 from the characteristics of the tip clearance flow at high aerodynamic loading (near stall) in Figure 1.5 (c) and (d). The latter could thus possibly act as an impinging jet on the upcoming blade in conditions near stall, in agreement with the proposed NSV model of Thomassin *et al*. (2008, 2009).

2.3 A Numerical Approach to the Resonant Tip Clearance Flow

The work presented in this Thesis complements previous work from Drolet, M., Thomassin, J., Vo, H.D. and Mureithi, N.W. (2009) who proposed a numerical method that uses computational fluid dynamics (CFD) as a complementary tool to the proposed NSV prediction model previously discussed. Consequently, this section presents a short summary of their findings for the benefit of the reader throughout the current work. A copy of the original work from Drolet *et al*. (2009) is available in Appendix 2 for more details.

The main objectives were first, to demonstrate that the tip clearance flow resonance can be captured using a simple single-row, single-blade passage unsteady CFD simulation with a moving mesh capability. Secondly, to show that the unsteady blade pressure behavior can be used as a design tool to predict the experimental critical NSV speeds observed by Thomassin *et al*. (2008) for the rotor under study.

2.3.1 Tip Clearance Flow Resonance Assessment: Numerical vs Experimental

Thomassin *et al*. (2008) measured the unsteady blade pressure on the blade suction side in their experiment. The available data was used as a metric to assess the resonance of the tip clearance flow in the work from Drolet *et al*. (2009). Figure 2.10 (a) and (b) present the normalized frequency spectra of the measured unsteady blade pressure at 80% chord and 96% span for two inlet temperatures, one cold and one hot, respectively. Figure 2.10 (c) and (d) shows equivalent data for the calculated pressure fluctuations, at 80% chord and 96% span, at three neighboring speeds in the NSV region for the cold and hot inlet temperatures, respectively. It can be observed that the pressure fluctuations are showing signs of resonance, with the highest peak near the critical NSV speed, as the rotor speed approach the critical NSV speed. These observations are in agreement with the resonance of the tip clearance flow, proposed by Thomassin *et al*. (2008, 2009), as the mechanism behind NSV.

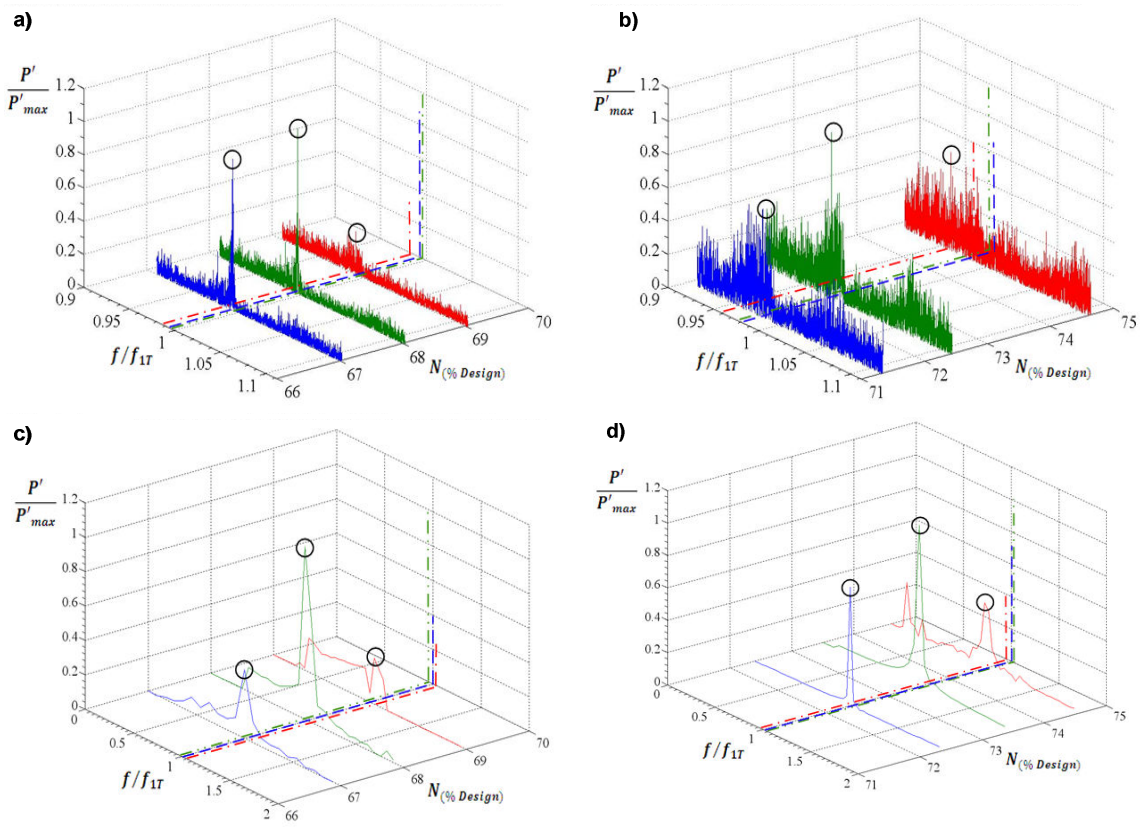

Figure 2.10 : Frequency spectrum of unsteady blade pressure: measured for a) cold and b) hot T1 and calculated for c) cold and d) hot T1, both plotted vs rotor speed

The peak amplitude of the unsteady blade pressure from the frequency spectra, at each rotor speed, was used to determine the critical NSV speed for both experimental and numerical results. Figure 2.11 (a) shows the data for all the experimental conditions tested while Figure 2.11 (b) presents the numerical results for all the simulated rotor speeds and temperatures. The polynomial curve fit of the experimental data suggests that the critical NSV speed occurred around 68.1% and 72.5% design speed for the cold and hot inlet temperatures, respectively. Similarly, the numerical results predicted the NSV critical speeds to be at 67.9% and 73.6% design speed, which showed very good agreement.

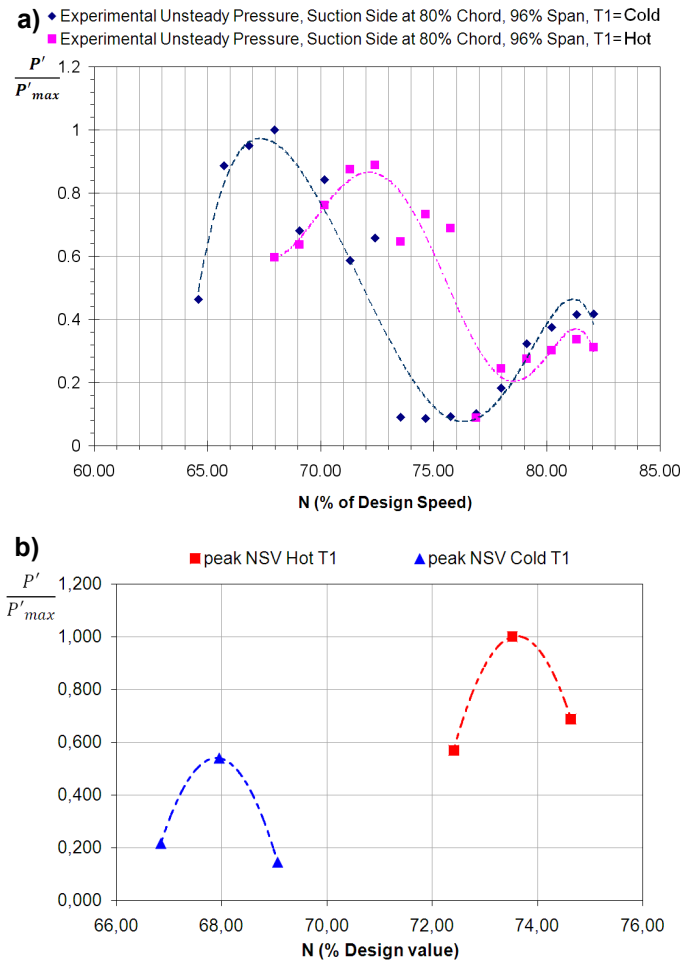

Figure 2.11 : Peak amplitude of unsteady blade pressure a) measured and b) calculated at 80% chord, 96% span for both cold and hot inlet temperatures

2.3.2 Resonance Condition and Tip Instability Convection Coefficient

The convection velocity (U_F) previously discussed and measured in the NSV rig experiment was estimated by Drolet *et al*. (2009) from the numerical simulations as the area-averaged tangential velocity (v), along the entire tip chord length, in the tip clearance flow. The resulting convection velocity was also used to calculate the resonance condition and the tip instability convection coefficient "k". The results are shown in Figure 2.12 (a) and (b), respectively. The experimental results are also shown for comparison.

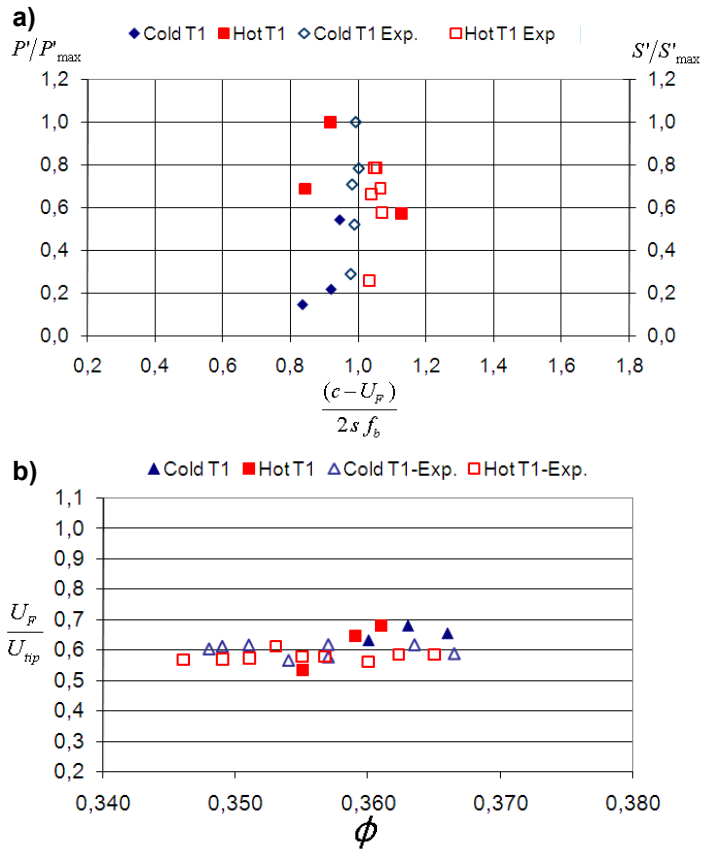

Figure 2.12 : Numerical vs experimental predictions of the convection velocity (U_F) shown for a) resonance condition and b) tip instability convection coefficient

It can be observed from the resonance condition of Figure 2.12 (a) that the peak unsteady blade pressure occur at the closest point from the resonance condition, which also corresponds to the critical NSV speed. In addition, the calculated convection velocity in Figure 2.12 (b) seems to over-estimate the measured values from the experiment. Using the averaged values of the measured vs. calculated k ($k=U_{tip}/U_F$) in equation (2.5), the predicted critical speeds were around 67% (experimental) vs. 63% (numerical) for the cold inlet temperature and 71% (experimental) vs. 68% (numerical) for the hot inlet temperature. The predictions based on the measured k values are in very good agreement with that found from Figure 2.11 (a). However, there is poor agreement between the predictions from the calculated values of k with predictions of Figure 2.11 (b). This suggests that the method used to estimate the convection velocity U_F should be improved.

2.4 Summary

As noted in this chapter, Non-Synchronous Vibrations (NSV) were widely studied in the field during the past two decades. NSV were associated with high-cycle fatigue damage on axial compressor blades. It was proposed that the tangential tip clearance flow, observed at high blade loading near stall, can act as an impinging jet on the upcoming blades by Vo (2006) as an attempt to explain NSV. Later, Thomassin *et al*. (2009) derived a novel "Jet Core Feedback Theory" as a possible mechanism behind NSV. They also developed a physics-based model, in the form of an equation, to predict the critical blade tip speed at which NSV can occur. The model was also validated through experiments by Thomassin *et al*. (2008). In the equation, a factor k that was called the "tip instability convection coefficient" was measured experimentally and found to have a significant impact on the accuracy of the NSV predictions obtained using the proposed model. Drolet *et al*. (2009) also proposed a numerical method to refine the NSV prediction but the latter requires significant computational resources. In addition, Thomassin *et al*. (2008) have measured the "k" parameter which also requires extensive rig testing. It is therefore relevant to seek a correlation that could determine the instability convection coefficient for a given compressor geometry, independently from experimental tests and simulations and that would be generic for any geometry, which is the main topic covered by this Thesis, as previously detailed in the research objectives section.

CHAPTER 3 METHODOLOGY

To achieve the main research objective, namely to obtain a generic correlation for the instability convection coefficient "*k*" for the NSV prediction model proposed by Thomassin *et al*. (2008, 2009), a computational approach was chosen. The choice for this methodology was selected primarily because it allows investigating different geometries, numerous tip clearance sizes and operating conditions without the high cost associated with equivalent experimental work. First, a dimensional analysis is carried out to establish the list of pertinent independent parameters upon which "*k*" depends. Thereafter, a parametric computational study is conducted in terms of the chosen dependent parameters. As opposed to Drolet *et al*. (2009) who averaged the tangential velocity component over the entire tip chord to estimate the "jet" velocity, U_F, (used in the NSV model of Thomassin *et al*. (2008, 2009) to calculate the instability convection coefficient "*k*"), the latter is estimated herein from an average of the leakage velocity (V_L) over a more suitable tip chord extent. This chapter will begin with the dimensional analysis, followed by a description of the geometrical configurations that were studied and finally the numerical setup.

3.1 Parametric Consideration on the Instability Convection Coefficient

A dimensional analysis was conducted to determine the parameters governing the *k* coefficient using a theoretical point of view. The parameters considered in the analysis, which were determined from the fluid mechanics associated with the NSV model proposed by Thomassin *et al*. (2009) and the jet-like behavior of the tip clearance flow as explained by Storer and Cumpsty (1991), are listed in Table 3.1. These parameters were selected since ΔP is what mainly drives the tip clearance flow, the blade tip speed (U_{tip}), mean tip clearance flow velocity (U_F) and tip clearance size (h) are directly related to the "jet" velocity and diameter, respectively, from the jet-core feeback theory. The blade tip chord (ς_{tip}) is a geometric characteristic of compressor blades while the operating temperature (T_{tip} and $T_{1,ref}$) and fluid density (ρ) consider the compressibility effect of the flow. These parameters are thus expected to influence the value calculated for "*k*".

Table 3.1 : Parameters used in dimensional analysis for k

Parameter	Definition	Units
ΔP	Pressure difference across blade	[Pa = Kg/m.s^2]
U_{tip}	Blade tip speed	[m/s]
h	Tip clearance size	[m]
ς_{tip}	Blade chord length at tip	[m]
U_F	Mean tip clearance flow velocity	[m/s]
T_{tip}	Average blade tip temperature	[K]
$T_{1,ref}$	Reference inlet temperature	[K]
ρ	Fluid density	[Kg/m^3]

Consequently, one can expect that the velocity U_F, that is used to calculate the instability convection coefficient (k), can be written as an arbitrary function g_1 of the following flow and geometry parameters:

$$U_F = g_1\left(\Delta P, U_{tip}, h, \varsigma_{tip}, T_{tip}, T_{1,ref}, \rho\right) \tag{3.1}$$

The four repeating parameters that were chosen to conduct the analysis are ρ, U_{tip}, ς_{tip} and $T_{1,ref}$ which can be used to form the following dimensionless groups (Π):

$$\text{(a) } \Pi_1 = \frac{U_F}{U_{tip}} = \frac{1}{k} \qquad \text{(b) } \Pi_2 = \frac{h}{\varsigma_{tip}} \equiv \tau \qquad \text{(c) } \Pi_3 = \frac{T_{tip}}{T_{1,ref}} \equiv \mathrm{T} \qquad \text{(d) } \Pi_4 = \frac{\Delta P}{\rho U_{tip}^2} \tag{3.2}$$

If we recall the definition of the instability convection coefficient (k) from equation (2.5), we now recognize that Π_1 is the reciprocal of k. In addition, Π_4 is analogous to a loading or "pressure coefficient" that can be written as:

$$\psi = \frac{\Delta P}{1/2\,\rho U_{tip}^2} \tag{3.3}$$

With Π_2 and Π_3 defined as the non-dimensional tip clearance (τ) and non-dimensional temperature (T), respectively, the instability convection coefficient "k" can now be written as an arbitrary function G_1 of the other dimensionless groups which leads to:

$$k \equiv \frac{U_{tip}}{U_F} = G_1(\tau, T, \psi) \tag{3.4}$$

NSV is known to occur at high loading such as in conditions near stall, as discussed in chapter 2. It will be argued later in chapter 4 that the blade loading ψ does not play an important role on the variations of the instability convection coefficient (*k*) in high loading conditions. Consequently, we can finally simplify the relation for "*k*" in NSV conditions as:

$$k \equiv \frac{U_{tip}}{U_F} \approx G_2(\tau, \mathrm{T}) \tag{3.5}$$

This relation puts forth the basic assumption considered in the current numerical study which states that the instability convection coefficient "*k*" will be mainly influenced by the tip clearance and operating temperature. The instability convection coefficient (*k*) was experimentally measured by Thomassin *et al*. (2008) for two inlet temperatures and two tip clearance sizes. The available data is presented as a function of the corrected speed in Figure 3.1 in which the tip clearance size is shown as a percentage of the tip chord.

It can be observed from Figure 3.1 that the parameter *k* appears to vary with tip clearance size. Indeed, when the tip clearance size is increased from 1% to 2% tip chord, the results shows that *k* changes from an average of 1.96 to 1.67 (cold) and from 1.85 to 1.73 (hot), respectively. Although there are not enough data points to provide adequate statistics on the variation of *k* with temperature, there is a slight distinction between the cold and hot measurements. The variation is especially distinct for the 2% tip clearance case; however, the trends are not as clear in the case of 1% tip clearance.

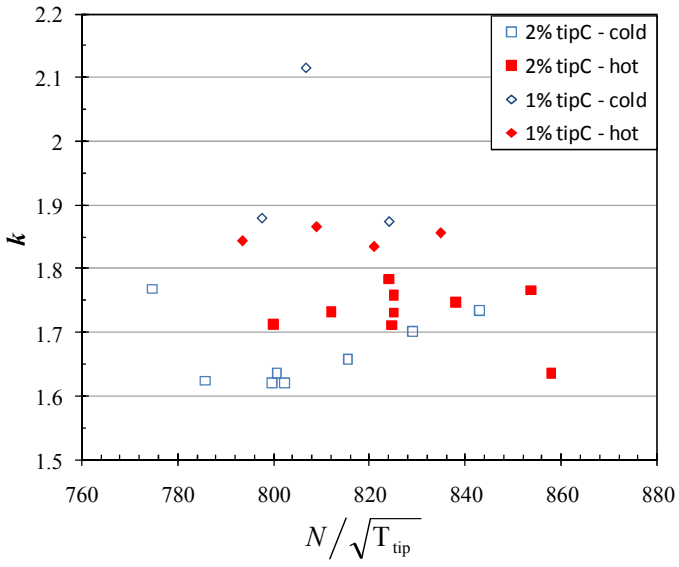

Figure 3.1 : Measured instability convection coefficient, *k*, at different operating conditions, data from Thomassin *et al*. (2008)

Consequently, the results obtained from the dimensional analysis conducted in this section are in agreement with the observations from the experimental results of Thomassin *et al*. (2008).

3.2 Studied Configurations

3.2.1 Compressor Rotors

Two different compressor rotor geometries, one subsonic (low-speed/front-loaded) and one transonic (high-speed/rear-loaded), were chosen for their distinctive aerodynamic characteristics which could provide insights into the generic nature of the current study. They will be both referred from now on as SR and TR geometries, respectively. The two geometries are characterized by, among other things, very different loading coefficient (ψ) near stall (the loading of the SR geometry was approximately twice the loading of the TR geometry) and were investigated at every ~4% design speed ranging from 67% to 85% for a total of six different rotor speeds. This was to ensure that any dependency on the tip speed would be captured. This speed range is also similar to that investigated by Thomassin *et al*. (2008) in their experiments. The characteristics of the two geometries are summarized in Table 3.2. The SR geometry has 45 blades with a tip solidity (σ) of 1.12 and a hub-to-tip ratio (ξ) of 0.8. The TR geometry is the

same rotor geometry that was used by Thomassin *et al*. (2008) in their experiment with 23 blades, $\sigma \approx 1.35$ and $\xi \approx 0.47$.

Table 3.2 : Characteristics of the compressor rotor geometries used for simulations

Parameter	**SR Rotor**	**TR Rotor**
Number of blades	45	23
Tip Solidity (σ)	1.12	1.35
Hub-to-tip ratio (ξ)	0.8	0.47
ϕ_{Design}	0.54	0.48
$\psi_{S\text{-}S,Design}$	0.32	0.34

3.2.2 Tip Clearance Sizes

Six different tip clearance sizes that are representative of typical values found in full engine configurations were simulated on both geometries investigated. These tip clearance sizes resulted in a dimensionless tip clearance (τ) range of 0.5% to 4.8% of the tip chord and from 0.2% to 2.6% for the subsonic and transonic geometry respectively, given the difference in the tip chord dimensions.

3.2.3 Inlet Temperatures

The simulations performed to assess the effect of tip clearance size on the instability convection coefficient (k) were set at ISA sea-level condition. The latter is also used herein to define the reference inlet temperature ($T_{1,ref}$). Three additional temperatures were selected to cover the most common half of a typical engine operating envelope in order to investigate the effect of temperature on k.

3.3 Numerical Set-up

3.3.1 Computational Tools

The numerical simulations were performed using the commercial code ANSYS CFX (release 11.0) which is a leading CFD code in the turbomachinery industry. This particular code was chosen primarily for its availability and for its multi-functionality and ease of use with, in addition to its solver, pre and post-processing tools tailored for turbomachinery applications. The meshes used for computation were generated using ANSYS TurboGrid and the data reduction was performed using CFX. Part of the data was also processed using MS Excel and MatLab.

3.3.2 Computational Domain and Mesh

A mesh study was performed by Drolet *et al*. (2009) and the mesh specifications used herein were selected based on their investigation. Typical meshes used for computation are depicted in Figure 3.2 for the SR geometry and Figure 3.3 for the TR geometry. The computational domain was set-up as a single-row, single-blade passage mesh with approximately 250,000 nodes. An HJCL grid topology was used, which allows for separate topology types in the upstream and downstream part of the domain. The total number of nodes in the computational domain slightly varied depending on the tip clearance size. However, the average number of nodes in the axial, circumferential and span-wise directions was roughly 80, 26 and 98, respectively, for the SR geometry and 85, 26 and 80, respectively, for the TR geometry. In order to have adequate resolution of the radial distribution of the tip clearance flow velocity, the number of radial nodes in the tip region was always kept to a minimum of 12 nodes for small tip clearance sizes and increased for larger tip clearance sizes. This also ensured a y+ value below 10 at the wall near the blade tip for all simulations. The inlet and outlet portions of the domain were approximately 2 and 1.5 pitches long for the SR and TR geometry, respectively. This allowed potential perturbations in the blade passage with circumferential wavelength on the order of one blade pitch (the computational domain width) to decay to zero at the inlet and exit boundary to satisfy the associated circumferentially uniform boundary conditions.

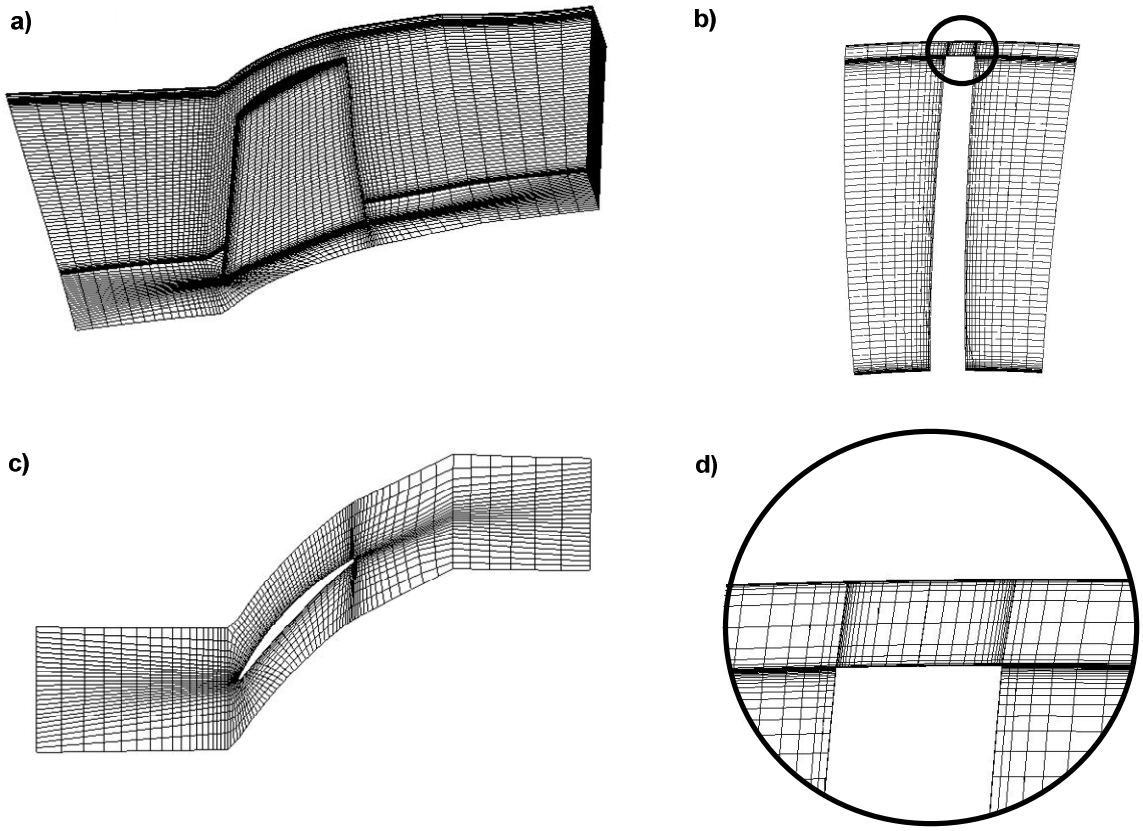

Figure 3.2 : Detailed mesh for Subsonic Rotor (SR): a) side view, b) blade tip section, c) span cut at mid-chord and d) close-up view of tip region

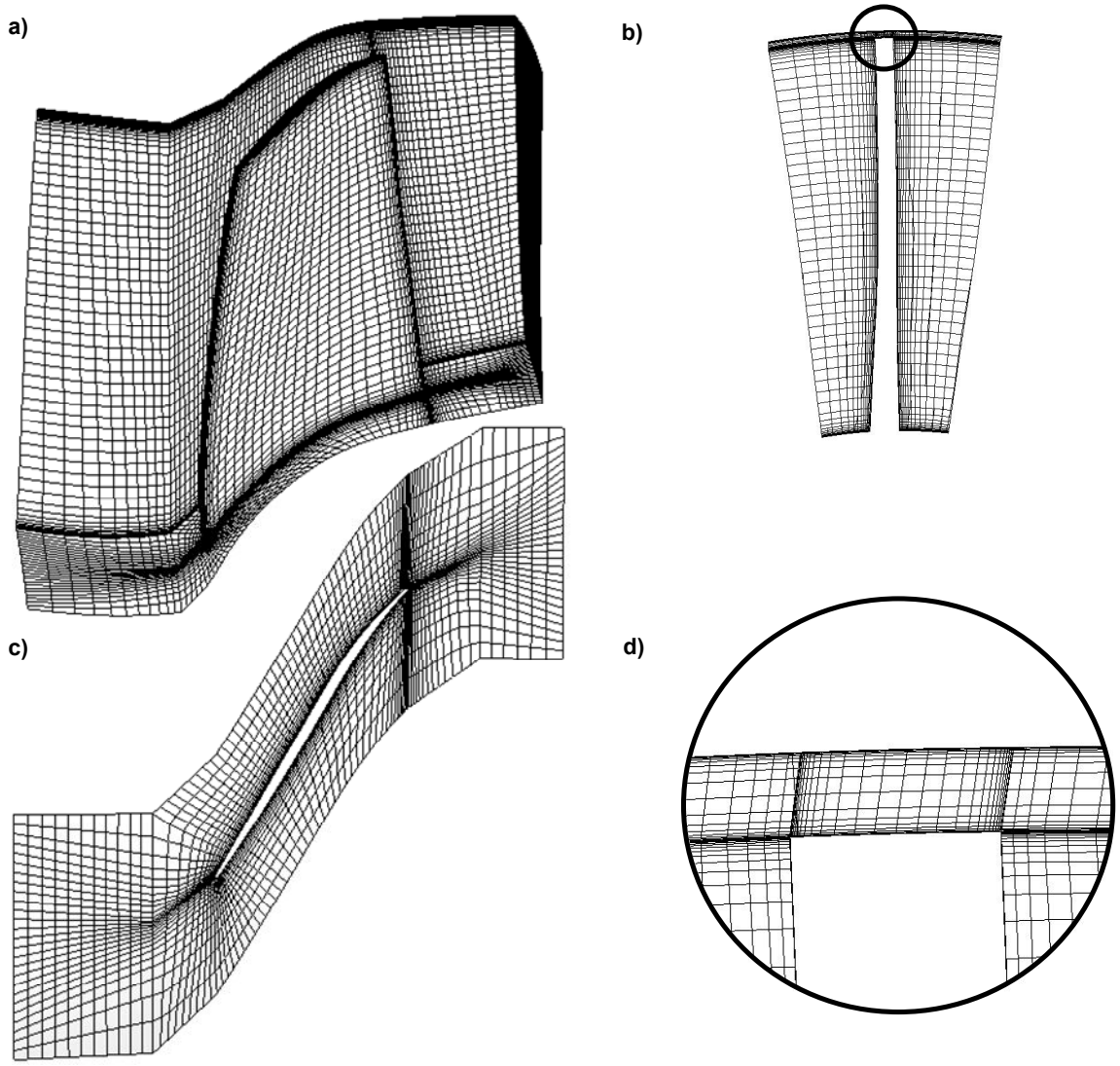

Figure 3.3 : Detailed mesh for Transonic Rotor (TR): a) side view, b) blade tip section, c) span cut at mid-chord and d) close-up view of tip region

3.3.3 Boundary Conditions

The total pressure, total temperature and swirl angle were prescribed at the domain inlet. At the domain exit, the average static pressure was also specified for each simulation. A no-slip boundary conditions was imposed to the wall portions of the domain, i.e. at the hub, casing (shroud) and blade surfaces. Due to the presence of an adverse pressure gradient in axial compressors, transition from laminar to turbulent flow occurs very close to the blade leading-edge. Consequently, the flow was assumed to be turbulent and a scalable wall function was applied to the wall surfaces. Scalable wall functions, unlike standard wall functions, can be

applied on arbitrarily fine meshes[1]. If the boundary layer is not fully resolved, it relies on the logarithmic wall function approximation to model the boundary layer without affecting the validity of the scalable wall function approach[2]. A two-equation k-ε model was used for turbulence modeling with 5% turbulence intensity and an Eddy viscosity ratio of 300. As previously mentioned, the computational domain was set-up as a single-row, single-blade passage mesh. Consequently, a circumferential periodicity condition with a conservative interface flux for mass, momentum, turbulence and energy equations was used.

3.3.4 Simulation Procedure

Given the large number of simulations required for this study, a steady-state mode was chosen primarily to save on computation time. Since the tip clearance flow near stall can sometimes show flow oscillations, sample simulations near stall were verified in unsteady mode to ensure that no flow oscillations were observed near stall such that the choice of steady-state would not affect the results. This verification was performed on the TR geometry for the 0.43%, 1.29% and 2.15% tip clearance cases and no flow oscillations were found in the sample simulations investigated. Consequently, it was decided that the choice for steady-state simulations was adequate for the purpose of the study, which aims to capture the area-averaged mean tip clearance flow velocity.

The average static pressure at the domain exit was increased to obtain points along different speedlines to characterize both compressors and approach the near-stall conditions associated with NSV. The near stall NSV region identified by Thomassin *et al*. (2008) where the instability convection coefficient (k) was measured was not necessarily at the compressor stability limit, as previously shown in Figure 2.8. However, it was decided to increase the outlet static pressure to approach the stability limit region as close as possible in order to have a common base among all the simulations. The spike-stall inception criteria as defined by Vo (2006) were used, most predominantly the leading-edge spillage criterion, to determine that limit which was considered as the near-stall region. It is important to note that when a static pressure boundary condition is

---

[1] ANSYS CFX, version 11.0, *help content on Scalable Wall Functions*.

[2] *Ibidem*.

used at the exit plane, solutions near stall cannot be calculated, should they fall beyond the peak total-to-static pressure rise characteristic of the compressor. This situation was encountered for a few simulations for which the last converged conditions closest to stall were used. The Reynolds number, based on the blade tip speed and blade tip chord length (ς), was on the order of $6E^5$ for the subsonic geometry and $1.5E^6$ for the transonic geometry.

CHAPTER 4 RESULTS AND DISCUSSION

This chapter presents the numerical results that were obtained from the computational study described in the previous chapter. The chord-wise leakage velocity (V_L) profiles are first presented which assess the jet-like pattern of the tip clearance flow. The velocity profiles of the leakage flow are then studied to gain insights on the expected variation of "*k*" with tip clearance size and establish a physics-based model to predict the behavior of "*k*". The results on the effect of tip clearance size and operating temperature on "*k*" are finally presented before the generic nature of the study is discussed.

4.1 Chord-wise Leakage Velocity Profiles

As was discussed in chapter 2, the NSV model proposed by Thomassin *et al*. (2008, 2009) is based on an impinging jet analogy that was suggested by Vo (2006). Storer J.A. and Cumpsty N.A. (1991) have also identified the jet-like behavior of the tip clearance flow from experimental measurements of the tip leakage velocity, V_L. The leakage velocity can be defined, according to Rains D.A. (1954), as the velocity component normal to the camber line. Since the leakage velocity (V_L) profile is analogous to a jet, the latter was used herein to estimate the "jet" velocity, U_F, in Thomassin's model and ultimately calculate the instability convection coefficient (*k*). The *u* and *v* velocity components in the tip clearance flow were calculated at ten equally spaced span-wise locations across the entire tip gap to find V_L which was area-averaged, over the tip clearance gap. This was repeated at ten chord-wise locations to cover the entire blade tip chord. The tip leakage flow velocity (V_L) was also calculated for all the different speed and tip clearance sizes investigated. The leakage velocity (V_L) is also normalized by the inlet axial velocity (C_a), as was done by Storer and Cumpsty (1991), for ease of comparison with their data.

Typical chord-wise tip leakage velocity distributions, calculated at different rotor speeds, for the subsonic geometry at 1% tip clearance and for the transonic geometry at 0.4% tip clearance, are shown in Figure 4.1 (a) and (b), respectively.

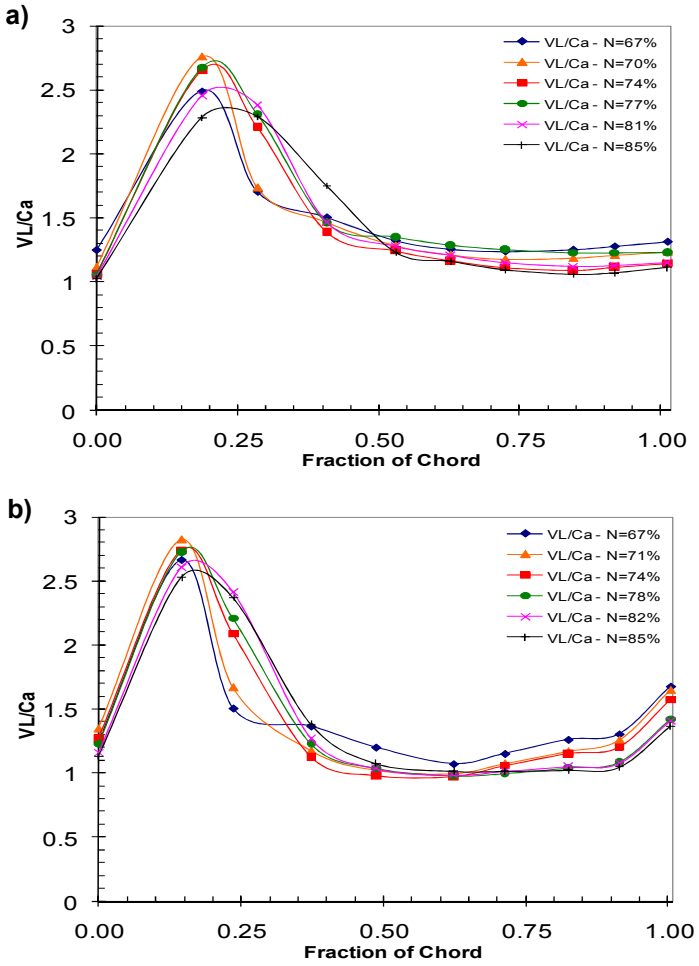

Figure 4.1 : Typical chord-wise V_L profiles calculated at different speeds for a) SR geometry at 1% chord tip clearance and b) TR geometry at 0.4% chord tip clearance

There is a distinctive pattern, analogous to a jet, in the first half portion of the blade chord, near the leading-edge. Similar results were also obtained for the other simulated tip clearances and are available in Appendix 3. The results are in agreement with those observed by Storer and Cumpsty (1991). However in their case, the maximum leakage flow velocity in the jet-like profile was obtained at mid-chord. This is most likely due to the loading conditions since their results were obtained at design conditions (closer to peak efficiency), where as in the present case, the results were calculated at very high blade loading (near stall). According to the resonant jet analogy proposed and experimentally verified by Thomassin *et al*. (2008,2009), this jet-like pattern observed in the first half portion of the chord for all simulated cases could be responsible for

NSV. Hence, the jet speed U_F used in Thomassin's model was calculated herein from the area-averaged tip leakage velocity in the first half portion of the blade near the leading-edge, from 0 to 0.5 chord length. Consequently, for the purpose of the current study the "jet" velocity, U_F, is defined according to equation (4.1). In this relation, ς_{tip} is the tip chord length and $V_{L,tip}$ is the spanwise area-averaged V_L velocity component at chordwise location "*i*".

$$U_F \equiv \frac{1}{\Delta \varsigma_{tip}} \int_{\varsigma_{tip,0}}^{\varsigma_{tip,f}} \left(\overline{V_{L,tip}} \right)_i \, d\varsigma_{tip} \tag{4.1}$$

Since the points in the tip clearance flow where the tip leakage velocity was calculated were discrete, the previous relation was implemented using a summation of the data. This can be written as shown in equation (4.2) in which "*x*" is a coordinate following the blade chord.

$$U_F \equiv \frac{1}{x_0 - x_f} \sum_{x_0}^{x_f} \left[\left(\overline{V_{L,tip}} \right)_i \cdot \left(\frac{x_{i+1} - x_{i-1}}{2} \right) \right] \tag{4.2}$$

4.2 U_F Velocity Profiles and Proposed Model for k vs τ

The velocity profile of the leakage flow across the tip gap near the center of the jet location, at around 20% of the chord, was investigated for all the different simulated tip clearances and speeds. An example of typical calculated profiles for the SR and TR geometries are shown in Figure 4.2 (a) and (b), respectively. Figure 4.2 (b) shows, for the transonic rotor, that the velocity profiles in the tip gap undergo a transition as the tip clearance is increased. The velocity profile is similar to that of a laminar boundary layer for small tip clearances (0.22%, 0.43%, 0.86% and 1.29% chord tip clearances) before it finally reaches a fuller profile, similar to a turbulent boundary layer, at large clearances (1.72%, 2.15% and 2.58% chord tip clearances). The same observation can be made from the subsonic geometry velocity profiles in Figure 4.2 (a) as well. Similar results were also obtained for the other simulated rotor speeds and are available in Appendix 3.

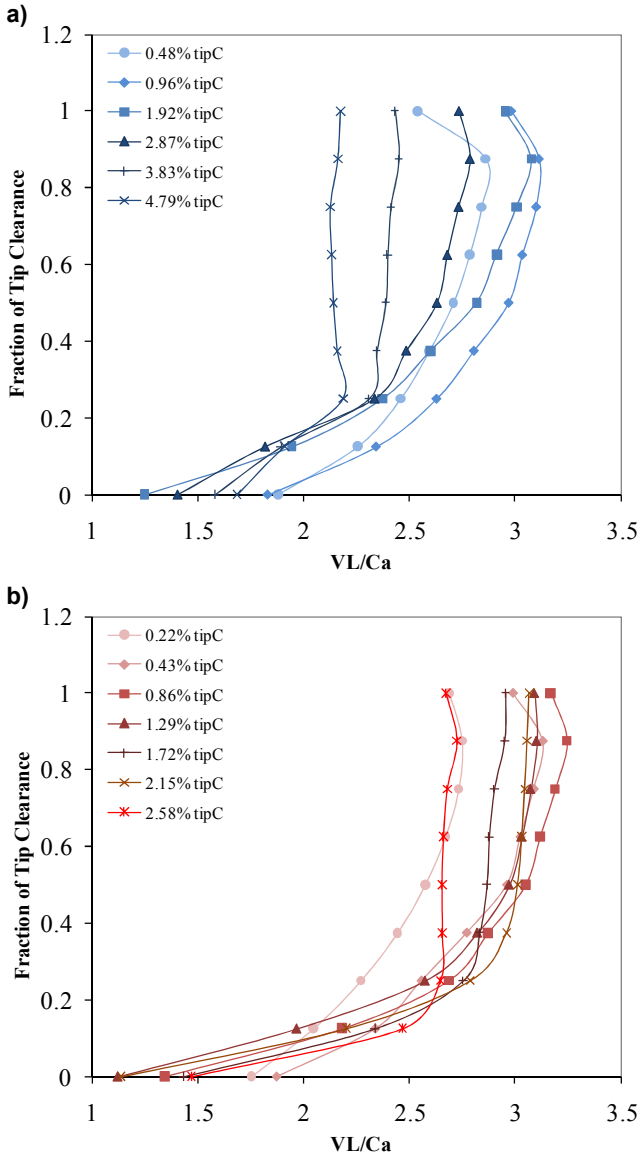

Figure 4.2 : Calculated tip leakage velocity profiles at 20% chord for a) SR geometry (N=70%) and b) TR geometry (N=71%)

The influence of the tip gap size and its contribution to turbulence was investigated from calculations of the area-averaged turbulent kinetic energy (TKE) across the tip gap which was averaged for all speeds (N-averaged) for a given tip clearance. The results are shown in Figure 4.3 in which logarithmic trend lines are fitted through the data points.

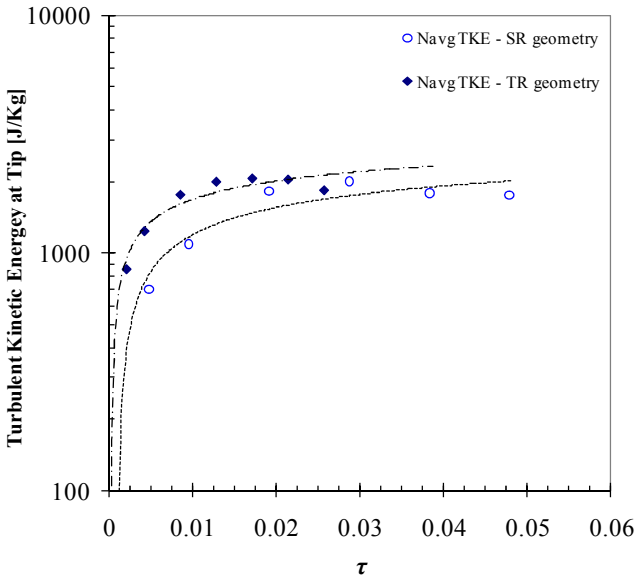

Figure 4.3 : Area-averaged turbulent kinetic energy at tip averaged for all speeds with logarithmic trend lines (dashed lines)

The results suggest that there is very low contribution of turbulent kinetic energy from the tip leakage flow at very small tip clearances and that its contribution rapidly increases before reaching an approximately constant value at very large tip clearances, once the tip leakage flow has become turbulent. These observations support the previous discussion regarding the laminar-to-turbulent profile transition observed in the tip leakage flow as the tip clearance increases.

It is now possible to anticipate the behavior of the instability convection coefficient, k, based on the observations of the tip leakage flow velocity profile transitions in the jet-like portion of the tip clearance flow. The k parameter was defined by Thomassin *et al*. (2008) as the ratio of the blade tip speed over the jet speed, as previously shown in equation (2.5). This definition was based on the tip clearance flow velocity profile and is analogous to the ratio U_{max}/U_{avg} for any velocity profile. Following this profile transition from turbulent to linear as the tip clearance goes to zero, it is expected that the value of k should go from approximately 1.16 to 2 with an intermediate point around 1.5, which corresponds to typical values observed for theoretical wall-bounded turbulent flow, linear and parabolic velocity profiles, respectively. The expected profile transition, based on the numerical results, is clearly depicted in Figure 4.4 (a) and (b).

Consequently, a correlation based on these physical trends is used to model the relation between k and the variation in non-dimensional tip clearance (τ), as will be discussed in the next section. The correlation that was developed is based on a modified inverse tangent profile and was found based on the velocity profile transition, as depicted in Figure 4.4 (c). The equation can be written as:

$$k(\tau) = \alpha \tan^{-1}\left[\beta\left(\tau_c - \tau\right)\right] + k_c \tag{4.3}$$

where τ_c and k_c represents the position of the inflection point in the inverse tangent profile. The coefficient α and β will be used to fit the proposed correlation to the numerical results.

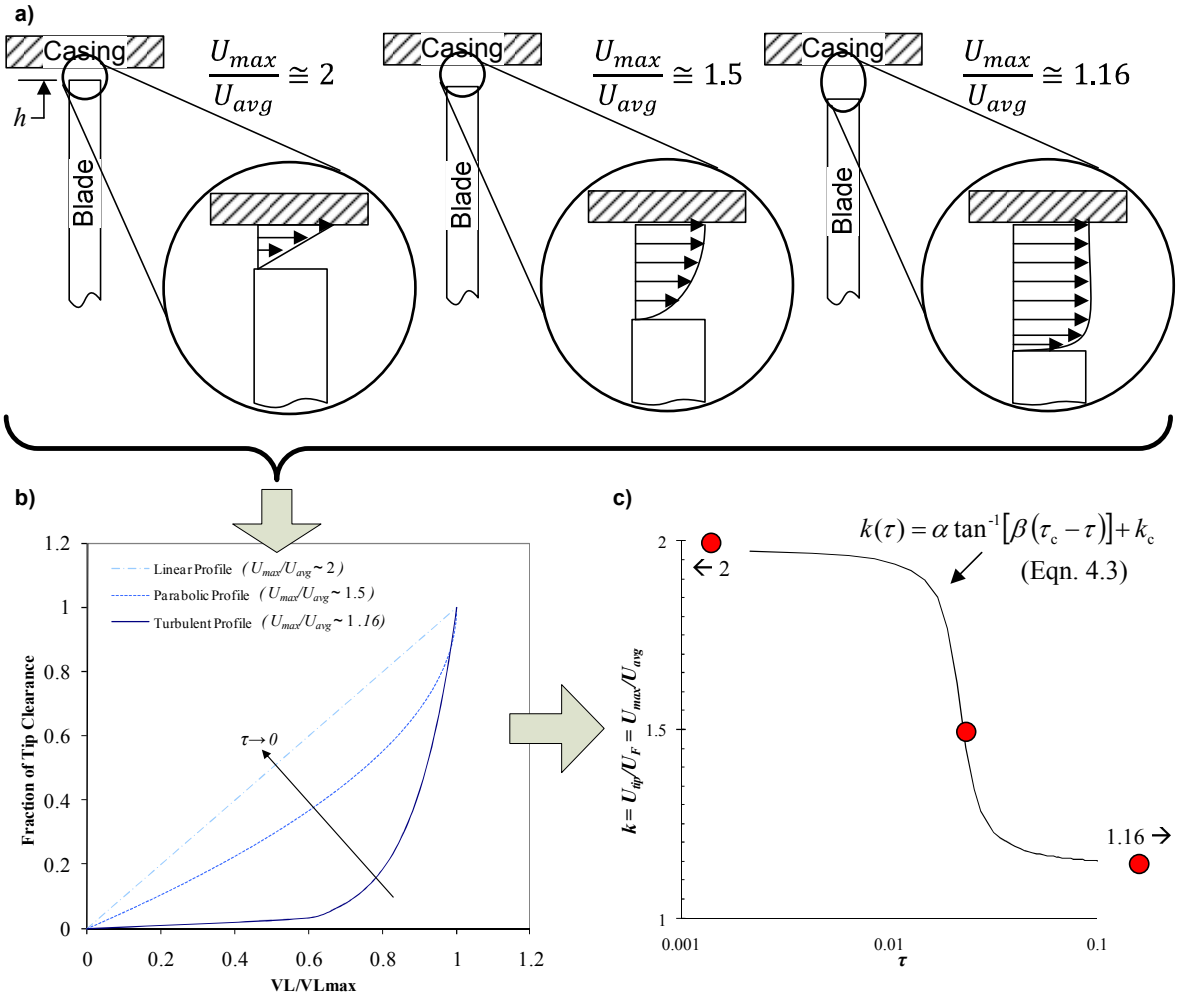

Figure 4.4 : a) Profile transition and b) detailed velocity profiles as tip clearance is increased, c) model of equation (4.3) derived based on velocity profile transitions

4.3 Effect of Tip Clearance Size on *k*

The calculated values for the *k* coefficient for all the speeds and tip clearances investigated are shown in Figure 4.5 (a). The standard deviation in the data varies, in terms of *k*, from approximately 2% to 6%. There was no significant correlation between the different rotor speeds simulated and the variation of the data. Hence, the scatter in the data is possibly related to the variations in aerodynamic loading, which will be discussed later on.

The correlation proposed in equation (4.3) was fitted through the numerical results averaged over all speeds (N-averared) for the calculated *k*., as shown in Figure 4.5 (b) using a custom fitting model in the commercial MatLab software. The values of τ_c and k_c used were 0.022 and 1.6, respectively, and the correlation coefficients were found to be α = 0.265 and β = 300. The resulting goodness-of-fit (*r*-value) is 0.99 and the rms error is around 3%. The results in Figure 4.5 (b) are also compared with available experimental data points of reported NSV cases for which the term "*k* exact" is defined as the exact value of *k* that would be required for equation (2.5) to perfectly predict the critical NSV speed. In the case of Thomassin *et al*. (2008), the "*k* measured" are the values of *k* measured from correlation between the casing and blade unsteady pressure measurements in their experiment.

It is seen that the available data from the literature show very good agreement with the proposed correlation model which was calculated from the speed-averaged numerical results. However, according to the previous discussion on profile transition, the value of k_c used in the correlation should have been ~1.5 when the value that best-fitted the results was 1.6. In addition, the value of *k* should tend to ~1.16 at large non-dimensional tip clearance when the correlation that best-fitted the results actually tends to ~1.2. One possible explanation for this small deviation at large non-dimensional tip clearance is that the velocity profile in the tip gap was found to be distorted at large tip clearance due to the roll-up of the tip clearance flow near the blade suction side originating from the leading edge.

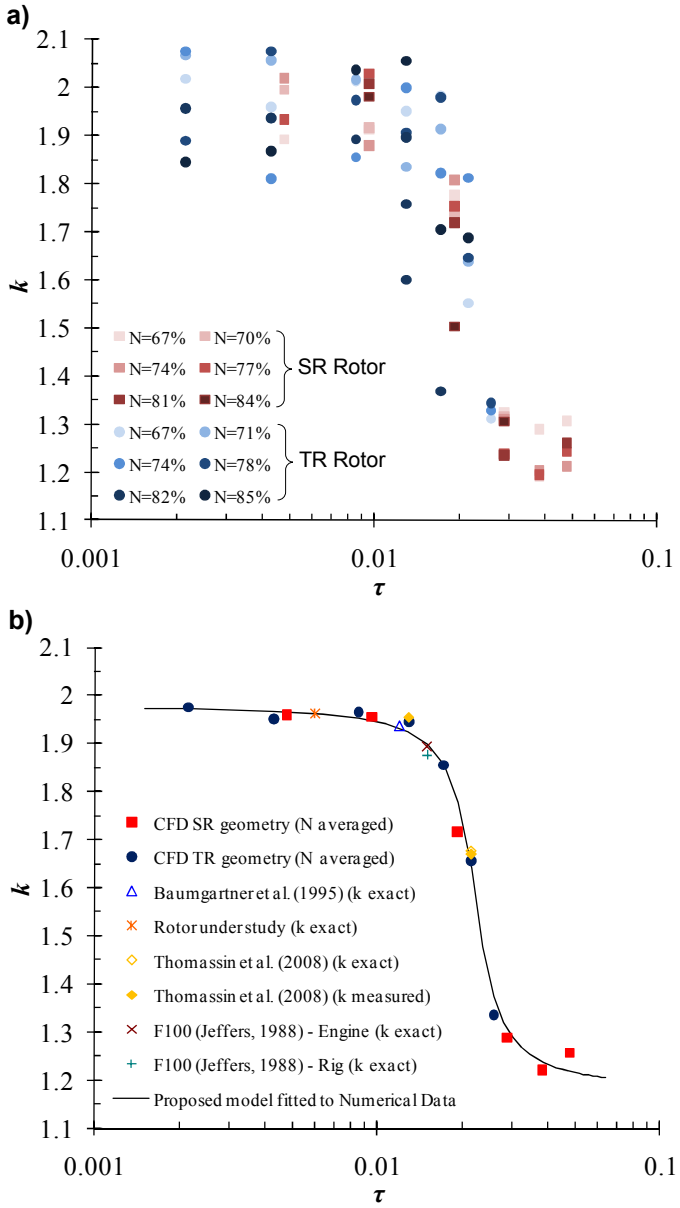

Figure 4.5 : Calculated *k*, a) Overall results, b) Comparison of available data in the literature with eqn. (4.3) fitted with speed-averaged numerical results

Examples of distorted velocity profiles are shown (circled) in Figure 4.6 (a). This distortion of the velocity profiles were also mostly observed on the subsonic rotor geometry which has a much thicker blade profile at the tip when compared to the transonic geometry (~5.17% of the tip chord for the SR geometry versus ~3.13% for the TR geometry). This suggests that the vena-contracta effect, depicted by the ideal tip clearance flow model of Rains (1954) in Figure 4.6 (b), is much

more dominant when the blade thickness is large (relative to the tip clearance size) since the boundary layer has more time to develop and become more important in size relative to the tip gap size. An example of vena-contracta observed for the SR geometry and calculated at N=74% and 3.83% tip clearance is also shown in Figure 4.6 (c), in agreement with the previous discussion.

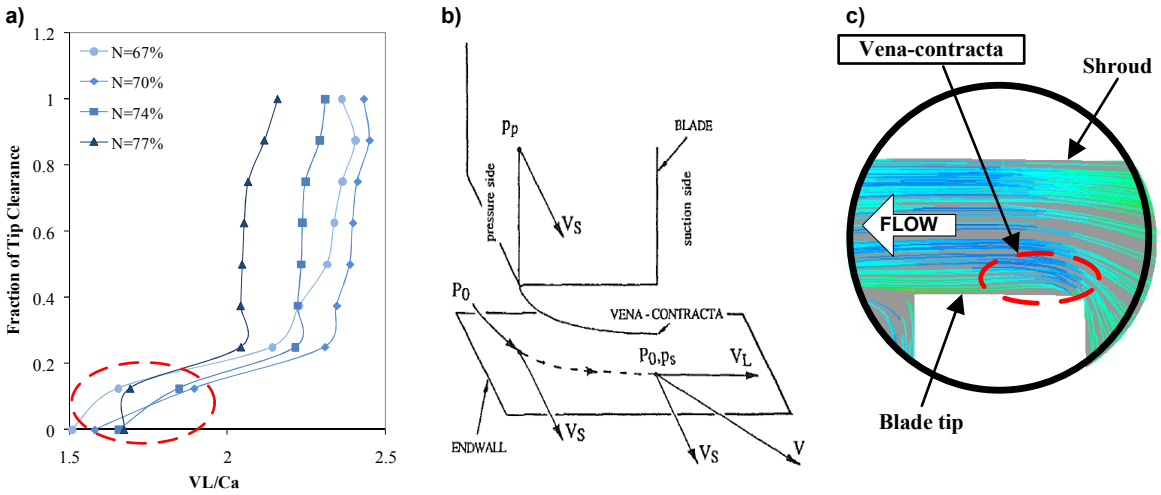

Figure 4.6 : a) Distorted velocity profiles calculated at 20% chord and 3.83% tip clearance for the SR geometry, b) Ideal tip clearance flow model of Rains (1954) as depicted in Storer and Cumpsty (1991) and c) vena-contracta as observed in simulations for N=74% in a)

This vena-contracta effect could thus be responsible for the distortion of the velocity profiles near the tip which introduce a bias the value of *k* calculated. This results in a deviation from the value of ~1.16 expected from typical turbulent velocity profiles.

4.4 Effect of Temperature on *k*

The previous results on the effect of the tip clearance showed that there is little or no effect from the different blade geometries on the *k* calculated. Consequently, the effect of temperature was only investigated for the transonic rotor geometry at two different tip clearances, one small and one large, to save on computational time. Four temperatures were simulated to cover half of a typical engine design envelope that is most likely encountered in flight conditions. The results are presented in Figure 4.7 in which the average values experimentally obtained by Thomassin *et al*.

(2008) are shown for comparison. The dashed lines are linear trend lines fitted through the data points.

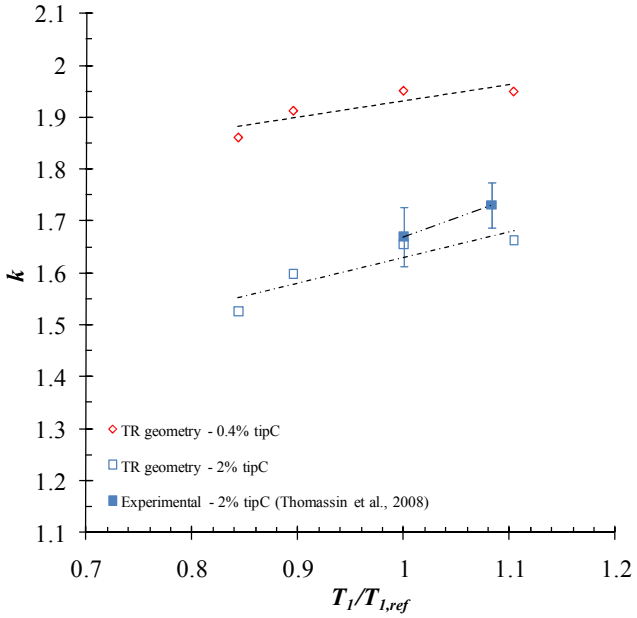

Figure 4.7 : Calculated *k* at different inlet temperatures near stall for the TR geometry. Experimental data is from Thomassin *et al*. (2008)

It can be observed from Figure 4.7 that there is a positive slope in the linear trend lines shown, as the temperature increase, for both tip clearances calculated. The actual values of the slopes calculated were $dk/dT \approx 0.32$ and $dk/dT \approx 0.5$ for the 0.4% and 2% tip clearance, respectively. The results are consistent with those found by Thomassin *et al*. (2008) for the 2% tip clearance case since both slopes calculated falls within that suggested by the experimental values, considering the measurement errors.

The numerical results showed that the tip instability convection coefficient "*k*" is influenced by both the tip clearance size and the operating temperature, which is in agreement with the experimental observations made by Thomassin *et al*. (2008). However, the numerical results also suggested that the major contribution appeared to come from the change in tip clearance size such that the variations in "*k*" with temperature can be neglected for preliminary design purposes. Indeed, a slight change in tip clearance size will cause a significant shift in the critical NSV

speed. To obtain a comparable effect by changing the operating temperature, the latter could possibly have to change to values outside a physically realistic operating range.

4.5 Application of the Proposed Correlation to NSV Prediction

The correlation that was proposed in equation (4.3) was fitted to the numerical results as previously presented in Figure 4.5 (b). The resulting equation was used here together with equation (2.5) as an attempt to improved the critical NSV speed predictions, when compared to the general approximation of $k = 2$ initially used by Thomassin *et al*. (2009). The results for the different cases available in the literature are presented in Table 4.1. For the Baumgartner *et al*. (1995) case, the exact tip clearance was unknown. A tip clearance value of 1% of the tip chord was thus used in equation (4.3), which is a typical tip clearance size encountered in such engines. In the F100 full engine case (Jeffers, 1988) the inlet temperature was unknown. However, it was mentioned that the engine was at high Mach number flight conditions such that an estimation of the inlet temperature can be made, based on the rig data (Jeffers, 1988). Consequently, a temperature ~1.2 times higher than the rig sea level conditions was used to determine k in this case. The resulting critical NSV speed predictions using the correlation proposed as equation (4.3) with $\tau_c = 0.022$, $k_c = 1.6$, $\alpha = 0.265$ and $\beta = 300$ shows very good agreement with the actual critical NSV speeds reported with a maximum error of 2.2%. These predictions are also a significant improvement when compared to that found using $k = 2$ (Thomassin *et al*., 2009). For the same predictions, that approximation yielded errors between 2.0% and 19.8%.

Table 4.1 : Summary of critical NSV speed predictions using proposed k correlation

Reference Case	$U_{tip,c}$ *[m/s]*	$U_{tip,c}$, $k = 2$ **(Thomassin *et al*., 2009)**	**% error ($k = 2$)**	$U_{tip,c}$, $k = k(\tau)$ **(eqn.** (4.3)**)**	**% error $k = k(\tau)$**
Baumgartner *et al*. (1995)	411.00	424.58	3.30	409.93	0.26
Rotor under study	329.50	335.96	1.96	329.53	0.01
Thomassin *et al*. (2008) (Cold T1)	292.88	349.48	19.33	286.39	2.22
Thomassin *et al*. (2008) (Hot T1)	312.57	374.49	19.81	306.88	1.82
F100 (Jeffers, 1988) (Rig)	386.20	411.68	6.60	390.78	1.19
F100 (Jeffers, 1988) (Engine)	380.00	401.20	5.58	380.84	0.22

The very good agreement between the reported critical NSV blade tip speed and the analytical predictions suggest that the proposed correlation can be used, together with equation (2.5), to accurately predict the critical NSV speed for a given rotor geometry and operating conditions at the very early stages of the design process.

4.6 Remarks on the Generic Nature of the Proposed Correlations

The numerical results were obtained from simulations conducted for two distinct geometries in the hope of finding a generic nature to correlation proposed for *k*. The pressure coefficients, calculated near stall for both geometries and all the tip clearances and different speeds that were simulated, are shown in Figure 4.8. The pressure coefficient was determined in this case using the area-averaged static pressure on the blade pressure and suction sides. It can be noted from the figure that the two geometries had quite different pressure coefficients in the near-stall region investigated; the loading of the SR geometry was almost twice the loading of the TR geometry.

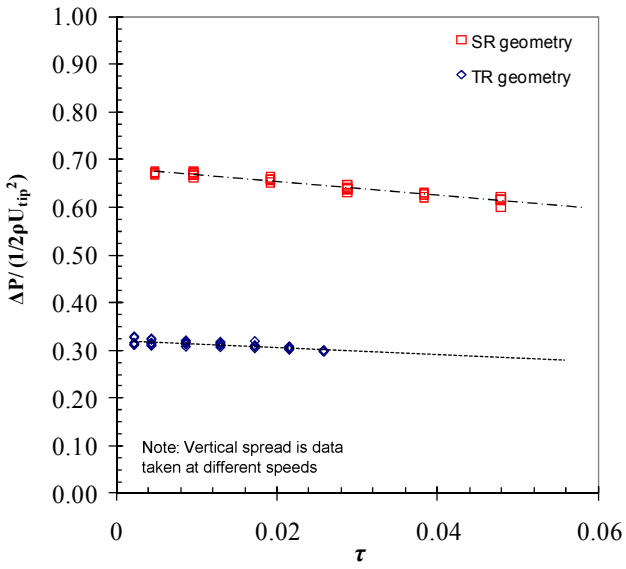

Figure 4.8 : Calculated blade loading vs. non-dimensional tip clearance for both SR and TR geometries (data shown for all the different speeds)

Despite this significant difference in loading, all the simulations showed similar trends in *k*. This suggests that the correlations found for *k* could be independent of the loading. Given that compressors can have different aerodynamic characteristics in terms of loading near stall, a

theoretical analysis is presented here to complement the above numerical results and support the generic nature of the correlation for "*k*" found in this work.

Based on the ideal tip clearance flow model proposed by Rains (1954), the tip clearance velocity (V) can be written in terms of the leakage (tangential) (V_L) and streamwise (V_S) components as:

$$V^2 = V_s^2 + V_L^2 \tag{4.4}$$

Storer and Cumpsty (1991) developed a simple model for the tip clearance flow, based on the ideal flow model proposed by Rains (1954), assuming a purely pressure-driven flow. In their model, previously presented in Figure 4.6 (b), the tip clearance flow velocity (V) and its stream wise component (V_s) were mathematically represented as:

$$V = \sqrt{\frac{2(P_0 - p_s)}{\rho}} \tag{4.5}$$

$$V_s = \sqrt{\frac{2(P_0 - p_p)}{\rho}} \tag{4.6}$$

Consequently, one can re-write equation (4.4) in terms of equations (4.5) and (4.6) to find an expression for the leakage velocity (V_L) in terms of a pressure coefficient. Using the blade tip speed (U_{tip}) to normalize the equation, this leads to:

$$\frac{V_L}{U_{tip}} = \sqrt{\frac{V^2}{U_{tip}^2} - \frac{V_s^2}{U_{tip}^2}} = \sqrt{\frac{(P_0 - p_p)}{1/2\,\rho U_{tip}^2} - \frac{(P_0 - p_s)}{1/2\,\rho U_{tip}^2}} = \sqrt{\frac{(p_p - p_s)}{1/2\,\rho U_{tip}^2}} \tag{4.7}$$

Since V_L was used in the present study to calculate the jet velocity U_F, as previously defined by equation (4.1), one can expect that the instability convection coefficient "*k*" should be proportional to the inverse of equation (4.7). This leads to equation (4.8) shown below, which can approximate how *k* is expected to vary with the aerodynamic loading, or pressure coefficient (ψ). The derivative, or rate of change, of U_{tip}/V_L is also shown in equation (4.9). These relations are also plotted as functions of the pressure coefficient in Figure 4.9.

$$k \propto \frac{U_{tip}}{V_L} = \sqrt{\frac{1}{\psi}} \tag{4.8}$$

$$\frac{dk}{d\psi} \propto \frac{d}{d\psi}\left(\frac{U_{tip}}{V_L}\right) = -\frac{1}{2}\sqrt{\frac{1}{\psi^3}} \tag{4.9}$$

In near-stall conditions, for which k was calculated to predict the critical NSV speed, the aerodynamic loading is typically high. In such conditions, Figure 4.9 (a) suggest that the value of k should show the smallest variations since the slope of equation (4.8) tends to zero, as shown in Figure 4.9 (b).

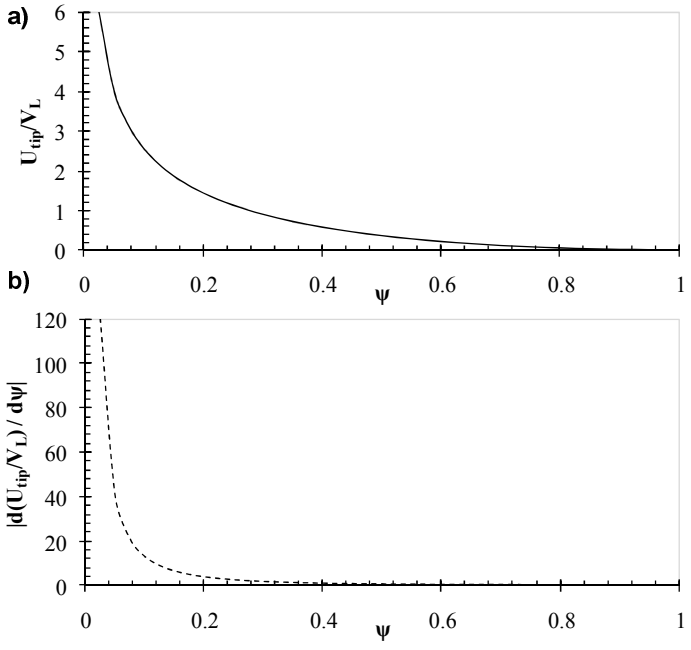

Figure 4.9 : a) Equation (4.8) and b) its derivative plotted vs ψ

To support the previous observations, a brief literature survey was conducted to assess typical values of flow coefficient (φ) and pressure coefficient (ψ) encountered near stall in most compressors. It should be noted that the pressure coefficient obtained from the literature was calculated using the static-to-static pressure rise to ensure a common base for comparison with the values calculated from the numerical simulations. An analytical relation, shown as equation (4.11) below, was found to determine the equivalent static-to-static pressure rise from the total-

to-static pressure rise, when the latter was the only information available from the literature. A summary of the available data is presented in Figure 4.10 and clearly shows that most compressors will stall at a loading greater than 0.3.

$$P_{t,in} = P_{s,in} + \frac{1}{2}\rho C_a^2 \tag{4.10}$$

$$\psi_{static-to-static} = \frac{P_{s,out} - P_{s,in}}{1/2\rho U_{tip}^2} = \frac{P_{s,out} - P_{t,in} + 1/2\rho C_a^2}{1/2\rho U_{tip}^2} = \psi_{total-to-static} + \phi^2 \tag{4.11}$$

It should also be noted that the pressure coefficients gathered from the literature are different to the one used in equation (4.8). In fact, the pressure coefficient in equation (4.8) was calculated using the static pressure rise across the blade surfaces while the static-to-static pressure coefficients obtained from the literature were calculated using the inlet and outlet static pressure. However, it is possible to show that both pressure coefficients are proportional to the blade solidity multiplied by the sinus of the blade stagger angle. This proportionality constant was found to be on the order of 1 for both geometries simulated and is typically the case for most compressor geometries. Consequently, the pressure coefficient used in equation (4.8) can be compared with the data taken from the literature.

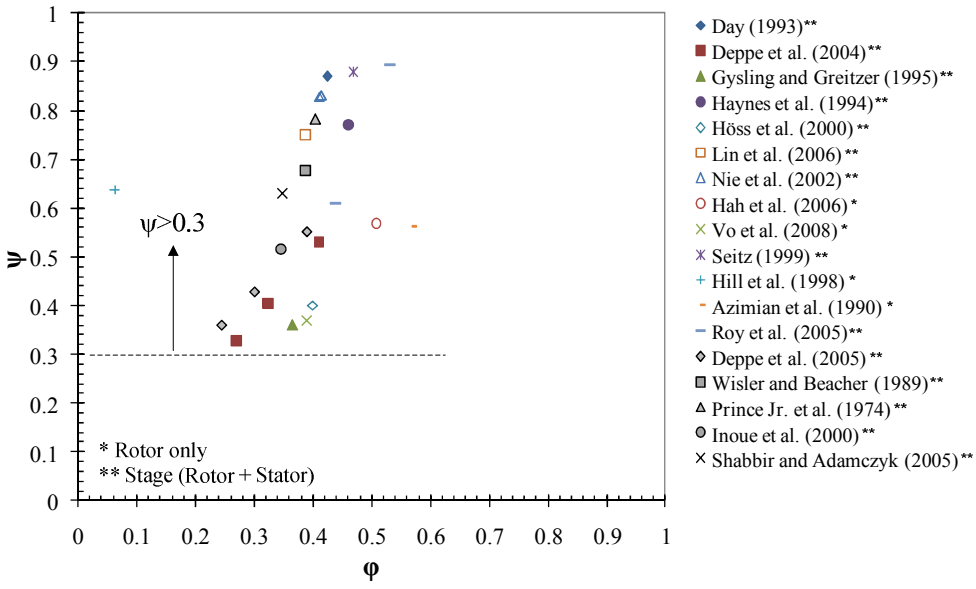

Figure 4.10 : Typical values of loading, ψ, and flow coefficient, φ, found near stall for different compressor geometries available in the literature

If we look at the variation in ψ of equation (4.8), a given value of k taken at ψ=0.6 will show variations of ±10% from ψ=0.45 to ψ=0.85. The analytical formulation of equation (4.8) supported by available data from the literature thus suggests a near-invariance of k with blade shape near stall. Consequently, the correlation proposed herein as equation (4.3) can be considered as generic for any compressor geometry for design purposes.

CHAPTER 5 CONCLUSION

A numerical experiment was conducted in order to determine the effect of tip clearance size and operating temperature on the prediction of NSV. Numerical simulations were performed for several tip clearance sizes and temperatures, representative of typical engine operating conditions, in order to estimate the "jet" velocity, U_F. The latter was ultimately used to determine the instability convection coefficient (k) used to refine the critical NSV blade tip speed predictions in a proposed NSV model by Thomassin *et al*. (2008, 2009). Two different rotor geometries were used to assess the generic nature of the study. The main conclusions and suggestions for future work based on the results obtained are presented below.

5.1 Conclusions and Contributions

The main contribution from the current work is a simple correlation that greatly improves the critical NSV speed predictions using the NSV model proposed by Thomassin *et al*. (2008, 2009). More specifically, the main conclusions are:

1. The tip instability convection coefficient, k, used to predict the critical NSV speed was found to vary with both tip clearance size and operating temperature. This is also consistent with the experimental results from Thomassin *et al*. (2008). However, the major contribution on the variations of k appears to come from the change in tip clearance size. The contribution from variations in temperature on k was found negligible for preliminary design purposes.

2. A correlation was proposed, based on the numerical results found in this study, to determine the k value as a function of the tip clearance size. The correlation was shown to significantly improve the critical NSV blade tip speed predictions, when applied to available data from the literature. The analytical NSV predictions were between 0.22% and 2.22% of the actual NSV critical tip speed. The same predictions using the previous assumption of $k = 2$ (Thomassin *et al*, 2009) were between 1.96% and 19.81% error.

3. The generic nature of the study was also discussed. An analytical formulation suggested a near-invariance of k with blade shape near stall, which was also validated

with available data from the literature. Consequently, it was recommended that the proposed correlation could be used for design purposes on any axial compressor blade geometry.

5.2 Recommendations for Future Work

The present work addresses the issues of predicting NSV near stall in the preliminary (mean-line) design stage of axial compressors. However, more accurate NSV prediction could be obtained with simple but clever CFD simulations at a later stage in the design process. In addition, there are CFD simulations performed during the current work which indicate a possibility of NSV occurring away from stall, near choke. These two subjects form the recommendations of future work as detailed below.

5.2.1 General Remarks on the Numerical Simulations

The instability convection coefficient "*k*" was defined by Thomassin *et al*. (2008, 2009) as the ratio of a "jet" velocity to the blade tip speed. However, the fundamental physics behind impinging jets also imply an actual convection speed of the instabilities. Steady-state simulations, as used in the current study, are not expected to capture this transient feature of the flow. Using unsteady simulations, as will be discussed in the following section, could therefore allow calculations of the instabilities' convection speed linked with the impinging jet analogy behind the proposed NSV model of Thomassin *et al*. (2008, 2009) and improve our understanding of the NSV mechanism.

The tip clearance size was also normalized in this work using the blade tip chord length which is the usual parameter used to characterize the tip clearance. However, since we are looking at a tangential component of the tip clearance flow, perhaps the local blade thickness could be used to normalize the tip clearance. In fact, the effect of blade thickness on the tip clearance velocity profile was addressed in section 4.3. Hence, using the blade thickness may perhaps minimize the spread between rotor speeds in Figure 4.5 (a).

The effect of temperature on "*k*" was investigated through numerical simulations in section 4.4. The results showed that the effect of temperature can be neglected for design purposes when compared to the effect of tip clearance size. However, only the general trends of "*k*" with

temperature were identified since the objective was mainly focused on the design applications of the study. Therefore, further numerical studies could capture the actual variations of "*k*" with temperature and be incorporated in the design rule proposed in the correlation for "*k*".

5.2.2 Numerical Assessment of Tip Clearance Flow Resonance using CFD-FEA Coupled Simulations

The unsteady numerical study from Drolet *et al*. (2009) discussed in Chapter 2, and provided in Appendix 2, used a single blade passage that had a periodicity condition which was chosen primarily for its low requirement in computation time and resources. The results from the simulations agreed with the NSV mechanism proposed by Thomassin *et al*. (2008, 2009) in addition to accurately predicting the critical NSV speeds. It showed that a single rotor passage model with a moving mesh can be used to locate the critical NSV condition. The periodicity conditions also imposed a 0 deg. inter-blade phase angle (IBPA), which is the worst case scenario expected. However, the IBPA is not anticipated to play a major role based on the proposed NSV model (Thomassin *et al*., 2008,2009) which originated from a jet-plate analogy. In fact, one blade could be fixed (no-motion) and if the adjacent blade vibrates, it would still synchronize the impinging shear layer frequency that would cause the tip clearance flow resonance leading to NSV.

Further investigation needs to be conducted to determine the actual size and detailed behavior, in terms of frequency and phase, of the flow structures responsible for NSV. Simulations with multiple passages using a moving mesh with complete fluid-structure interaction and blade finite-element analysis could perhaps capture both the NSV and the associated blade stress levels. The model proposed in Drolet *et al*. (2009) also approximated the mode shape and displacement amplitude at the blade tip which allows accurate prediction of the critical NSV speeds but does not simulate the proper pressure fluctuations amplitude. Simulations with more accurate representation of the mode shapes and displacement amplitude may allow capturing the pressure amplification levels more accurately. In addition, the effect of different time step values used for simulations should be considered to determine the effect on the resonant frequency response of the pressure fluctuations.

5.2.3 Possible Configuration for NSV in Choked-Flow Conditions

As previously explained, NSV are known to occur in near-stall conditions in which the high blade loading results in a tangential tip clearance flow that impinge on the upcoming blades. Since the only requirements for NSV to occur based on the proposed NSV model of Thomassin *et al*. (2008, 2009) are the impingement pattern and the proper tip temperature to provide the acoustic feedback, it is also suspected that NSV could occur in choked-flow conditions. Indeed, the presence of the shock could provide enough pressure difference across the blades to create the proper conditions for NSV. The leakage flow velocity (V_L) chord-wise profile was thus investigated from the numerical simulations performed and discussed in Chapter 3 and 4, to seek a jet-like pattern that would show the proper characteristics. The results are shown, for the TR geometry, in Figure 5.1 (a). It can be seen that the jet-like pattern of the tip leakage flow is divided into two distinct parts due to the presence of the passage shock, identified by the dashed line on the figure. On Figure 5.1 (b), it can be observed that the portion of the tip leakage flow on the upstream side of the shock, on the left of the dashed line on the figure, gets immediately redirected in the stream-wise direction as soon as it reaches the passage flow. Similar observations were obtained with the SR geometry.

However, the jet-like pattern on the downstream side of the shock, right side of dashed line on Figure 5.1 (b), has enough momentum to travel through the low momentum region behind the shock and reach the upcoming blade to act as an impinging jet, as circled on Figure 5.1 (b). In fact, impingement patterns were observed on the upcoming blade pressure side at the trailing edge. Therefore, the jet-like behavior of the tip leakage flow near the trailing edge provides the proper characteristics to possibly encounter NSV in choked-flow conditions.

An experimental investigation into the proposed configuration for NSV in choked conditions would definitely provide some insights into the physics behind the proposed NSV model of Thomassin *et al*. (2008,2009) and its application to choked NSV.

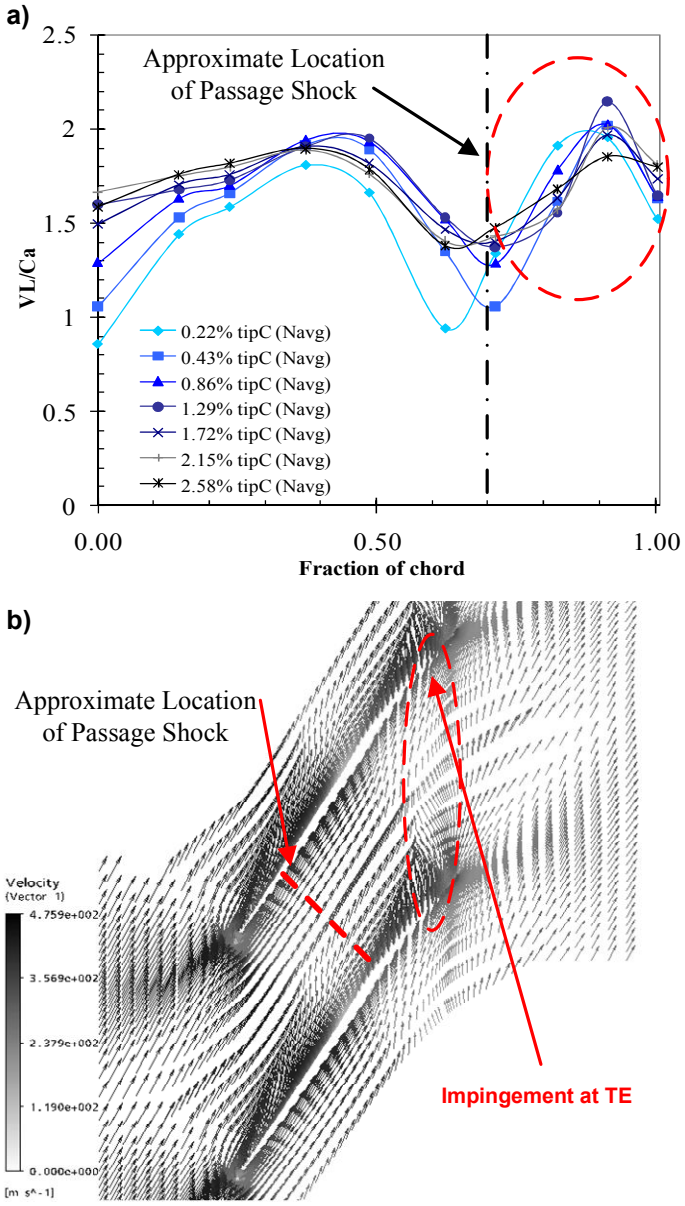

Figure 5.1 : Possible configuration for choke NSV, a) chord-wise profile of speed-averaged V_L/C_a in choked flow conditions showing jet-like pattern near trailing-edge and b) vector plot at tip showing impingement near trailing edge, data calculated for TR geometry, N=82% and 1.29% tip clearance

BIBLIOGRAPHY

Azimian, A.R., Elder, R.L. and McKenzie, A.B. (1990). *Application of Recess Vaned Casing Treatment to Axial Flow Fans*, Journal of Turbomachinery, 112.

Baumgartner, M., Kameier, F. and Hourmouziadis, J. (1995). *Non-Engine Order Blade Vibration in a High Pressure Compressor,* 12th International Symposium on Airbreathing Engines, Melbourne, Australia.

Blevins, R.D. (1990). *Flow-Induced Vibration*, 2nd Edition, Van Nostrand Reinhold, New York.

Cumpsty, N.A. (1989). *Compressor Aerodynamics*, Longman Group, United Kingdom.

Day, I.J. (1993). *Stall Inception in Axial Flow Compressors*, Journal of Turbomachinery, 115.

Deppe, A., Saathoff, H. and Stark, U. (2005). *Spike-Type Stall Inception in Axial-Flow Compressors,* Proceedings of the 6th European Conference on Turbomachinery – Fluid Dynamics and Thermodynamics, Lille, France.

Deppe, A., Saathoff, H. And Stark, U. (2004). *Stall Inception Phenomena in Three-Stage Low-Speed Axial Compressor*, 10th International Symposium on Transport Phenomena and Dynamics of Rotating Machinery, Honolulu, Hawaii.

Dowell, E.H., Crawley, E.F., Curtiss, Jr. H.C., Peters, D.A., Scanlan, R.H. and Sisto, F. (1995). *A Modern Course in Aeroelasticity,* Kluwer Academic Publishers.

Drolet, M., Thomassin, J., Vo, H.D. and Mureithi, N.W. (2009). *Numerical Investigation into Non-Synchronous Vibrations of Axial Flow Compressors by the Resonant Tip Clearance Flow,* GT2009-59074, Proceedings of the ASME Turbo Expo, Orlando, Florida.

Fukano, T. and Jang, C.-M. (2004). *Tip Clearance Noise of Axial Flow Fans Operating at Design and Off-Design Condition,* Journal of Sound and Vibrations, 275(3-5), 1027-1050.

Gysling, D.L. and Greitzer, E.M. (1995). *Dynamic Control of Rotating Stall in Axial Flow Compressors using Aeromechanical Feedback*, Journal of Turbomachinery, 117.

Hah, C., Bergner, J. and Schiffer, H.P. (2006). *Short Length-Scale Rotating Stall Inception in a Transonic Axial Compressor – Criteria and Mechanisms*, GT2006-90045, Proceedings of the ASME Turbo Expo, Barcelona, Spain.

Haynes, J.M., Hendricks, G.J. and Epstein, A.H. (1994). *Active Stabilization of Rotating Stall in a Three-Stage Axial Compressor*, Journal of Turbomachinery, 116.

Hill, S.D., Elder, R.L. and McKenzie, A.B. (1998). *Application of Casing Treatment to an Industrial Axial-Flow Fan*, Proceedings of the Institution of Mechanical Engineers, 212, 225-233.

Ho, C.-M. and Nosseir, S. (1981). *Dynamics of an Impinging Jet Part I: The Feedback Phenomena,* Journal of Fluid Mechanics, 105, 119-142.

Höss, B., Leinhos, D. And Fottner, L. (2000). *Stall Inception in the Compressor System of a Turbofan Engine*, Journal of Turbomachinery, 122.

Inoue, M., Kuroumaru, M., Tanino, T. and Furukawa, M. (2000). *Propagation of Multiple Short Length-Scale Stall Cells in an Axial Compressor Rotor*, Journal of Turbomachinery, 122.

Jeffers, J.D. (1988). *Aeroelastic Thermal Effects*, AGARD Manual on Aeroelasticity in Axial Turbomachines, vol.2, No.298, pp.21(1)-21(6).

Kameier, F. and Neise, W. (1997a). *Experimental Study of Tip Clearance Losses and Noise in Axial Turbomachines and their Reduction,* Journal of Turbomachinery, 119, 460-471.

Kameier, F. and Neise, W. (1997b). *Rotating Blade Flow Instability as a Source of Noise in Axial Turbomachines,* Journal of Sound and Vibrations, 203(2), 833-853.

Kielb, R.E., Thomas, J.P., Barter, J.W. and Hall, K.C. (2003). *Blade Excitation by Aerodynamic Instabilities – A Compressor Blade Study,* GT-2003-38634, Proceedings of the ASME Turbo Expo, Atlanta, Georgia.

Lin, F., Li, M. and Chen, J. (2006). *Long-to-Short Length-Scale Transition: A Stall Inception Phenomenon in an Axial Compressor with Inlet Distortion*, Journal of Turbomachinery, 128.

Liu, J.M., Holste, F. and Neise, W. (1996). *On the Azimutal Mode Structure of Rotating Blade Flow Instabilities in Axial Turbomachines,* AIAA paper 96-1741, AIAA & CEAS Aeroacoustics Conference.

Lucas, M.J. (1997). *Acoustic Characteristics of Turbomachinery Cavities*, ASME Press, New York.

Mailach, R., Lehmann, I. and Vogeler, K. (2001a). *Rotating Instabilities in a Axial Compressor Originating from the Fluctuating Blade Tip Vortex,* Journal of Turbomachinery, 123(3), 453-463.

Mailach, R., Sauer, H. and Vogeler, K. (2001b). *The Periodical Interaction of the Tip Clearance Flow in the Blade Rows of Axial Compressors,* 2001-GT-0299, Proceedings of the ASME Turbo Expo, New Orleans, Louisiana.

März, J., Hah, C. and Neise, W. (2002). *An Experimental and Numerical Investigation into the Mechanism of Rotating Instability,* Journal of Turbomachinery, 124, 367-375.

Menter, F. and Egorov, Y. (2007). *Turbulence Modeling of Aerodynamic Flows*, International Aerospace CFD Conference, June 18-19, Paris.

Nie, C., Xu, G., Cheng, X. and Chen, J. (2002). *Micro Air Injection and its Unsteady Response in a Low-Speed Axial Compressor*, Journal of Turbomachinery, 124.

Prince Jr., D.C., Wisler, D.C. and Hilvers, D.E. (1974). *Study of Casing Treatment Stall Margin Improvement Phenomena*, General Electric Company, NASA Report No. CR-134552.

Raffel, M., Willert, C.E., Wereley, S.T. and Kompenhans, J. (2007). *Particle Image Velocimetry: A Practicle Guide*, 2nd Edition, Springer.

Rains, D.A. (1954). *Tip Clearance Flows in Axial Flow Compressors and Pumps*, Ph.D. Thesis, California Institute of Technology, Laboratory Report No.5.

Roy, B., Chouhan, M. and Kaundinya, K.V. (2005). *Experimental Study of Boundary Layer Control through Tip Injection on Straight and Swept Compressor Blades*, GT2005-68304, Proceedings of the ASME Turbo Expo, Reno-Tahoe, Nevada.

Saravanamuttoo, H.I.H., Rogers, G.F.C. and Cohen, H. (2001). *Gas Turbine Theory*, 5th Edition, Pearson Education Limited, England.

Schrapp, H., Stark, U. and Saathoff, H. (2008). *Breakdown of the Tip Clearance Vortex in a Rotor Equivalent Cascade and in a Single-Stage Low-Speed Compressor,* GT2008-50195, Proceedings of the ASME Turbo Expo, Berlin, Germany.

Seitz, P.A. (1999). *Casing Treatment for Axial Flow Compressors*, Ph.D. Thesis, Department of Engineering, University of Cambridge, Cambridge, Massachussetts.

Shabbir, A. And Adamczyk, J.J. (2005). *Flow Mechanism for Stall Margin Improvement due to Circumferential Casing Grooves on Axial Compressors*, Journal of Turbomachinery, 127.

Spiker, M.A., Kielb, R.E., Hall, K.C. and Thomas, J.P. (2008). *Efficient Design Method for Non-Synchronous Vibrations using Enforced Motion,* GT2008-50599, Proceedings of the ASME Turbo Expo, Berlin, Germany.

Spille-Kohoff, A. (2006). *Acoustic Simulations with ANSYS CFX*, 24th CADFEM Users' Meeting 2006 International Congress on FEM Technology with 2006 German ANSYS Conference, Stuttgart Region, October 25-27, Stuttgart Region, Germany.

Storer, J.A. and Cumpsty, N.A. (1991). *Tip Leakage Flow in Axial Compressors*, Journal of Turbomachinery, 113, 252-259.

Thomassin, J. (2010). *Modélisation des Vibrations Asynchrones d'Aubes de Compresseurs Axiaux par la Résonance de l'Écoulement de Jeu*, Ph.D. Thesis, École Polytechnique de Montréal.

Thomassin, J., Vo, H.D. and Mureithi, N.W. (2009). *Blade Tip Clearance Flow and Compressor NSV: The Jet Core Feedabck Theory as the Coupling Mechanism,* Journal of Turbomachinery, vol. 131.

Thomassin, J., Vo, H.D. and Mureithi, N.W. (2008). *Experimental Demonstration to the Tip Clearance Flow Resonance behind Compressor NSV,* GT2008-50303, Proceedings of the ASME Turbo Expo, Berlin, Germany.

Thorsten, G. and Othmer, C. (2006). *Evaluation of Aerodynamic Noise Generation: Parameter Study of a Generic Side Mirror Evaluating the Aeroacoustic Source Strength*, ECCOMAS CFD 2006, TU Delft, The Netherlands.

Vo, H.D., Tan, C.S. and Greitzer, E.M. (2008). *Criteria for Spike Initiated Rotating Stall,* Journal of Turbomachinery, vol. 130.

Vo, H.D. (2006). *Role of Tip Clearance Flow in the Generation of Non-Synchronous Vibrations,* AIAA paper 2006-629, Proceedings of the 44th AIAA Aerospace Sciences Meeting and Exhibit, Reno, Nevada.

Vo, H.D. (2001). *Role of Tip Clearance Flow on Axial Compressor Stability,* Ph.D. Thesis, Department of Aeronautics and Astronautics, Massachusetts Institute of Technology.

Wernet, M.P., Zante, D.V., Strazisar, T.J., John, W.T. and Prahst, P.S. (2005). *Characterization of the Tip Clearance Flow in an Axial Compressor using 3-D Digital PIV,* Experiments in Fluids, 39(4), 743-753.

Wisler, D.C. and Beacher, B.F. (1989). *Improved Compressor Performance using Recessed Clerance (Trenches)*, AIAA Journal of Propulsion, 5(4), 469-475.

Xianjun, Y., Baojie, L. and Haokang, J. (2007). *Characteristics of the Tip Leakage Vortex in a Low-Speed Axial Compressor,* AIAA Journal, 45(4), 870-878.

Zhang, H., Lin, F., Chen, J., Deng, X. and Huang, W. (2006). *A Study on the Mechanism of Tip Leakage Flow Unsteadiness in an Isolated Compressor Rotor,* GT2006-91123, Proceedings of the ASME Turbo Expo, Barcelona, Spain.

APPENDIX 1 – Particle Image Velocimetry (PIV) Experiment

Experimental Set-Up

The fluctuations of the leading edge tip vortex have been possibly linked to rotating instabilities and non-synchronous vibrations from previous work by Liu *et al*. (1996), Kameier *et al*. (1997a, 1997b), Mailach *et al*. (2001a), Mailach *et al*. (2001b), März *et al*. (2002), Fukano *et al*. (2004) and Zhang *et al*. (2006), as previously discussed in chapter 2. The characteristics of the leading edge tip vortex in near-stall conditions were also found in agreement with the proposed NSV model of Thomassin *et al*. (2008, 2009) as a possible impinging jet in Drolet *et al*. (2009). Hence, further experimental investigation of the leading edge tip vortex during NSV conditions, near stall, was conducted using particle image velocimetry (PIV) to gain further understanding of the proposed NSV mechanism. The design of the experiment was based on previous work from Schrapp, H., Stark, U. and Saathoff, H. (2008). Additional reference on PIV experimental measurements and characterization of tip clearance flow can be found in Xianjun, Y., Baojie, L. and Hokang, J. (2003) and Wernet, M.P., Zante, D.V., Strazisar, T.J., John, W.T. and Prahst, P.S. (2005). The experiment was conducted in a compressor test rig facility which is depicted in Figure A2.1.

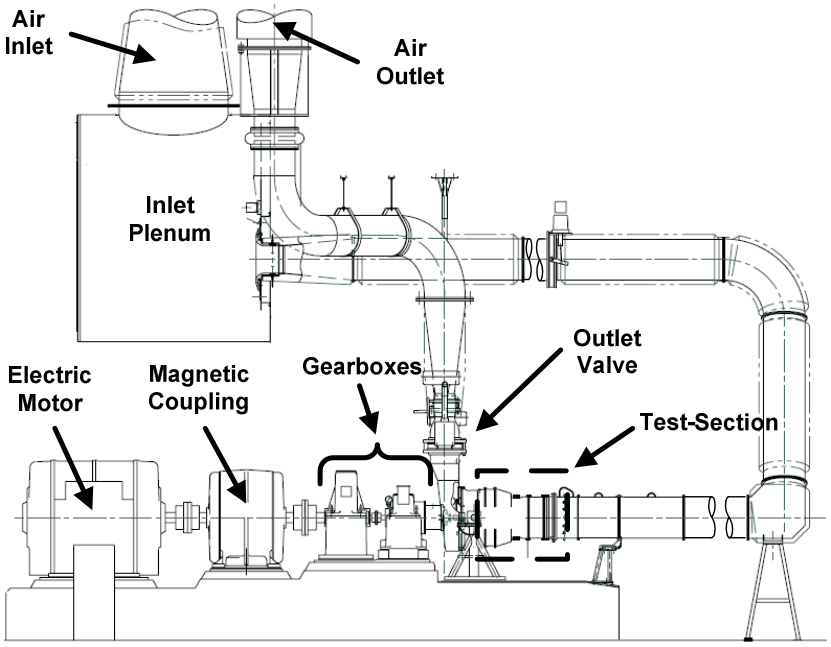

Figure A2.1 : Details of compressor rig installations

The compressor rotor is driven by an electric motor through a series of gearboxes. The air comes through a plenum chamber before being redirected through the test-section inlet. An outlet valve is placed before the outlet from the test-section which allows to change the back-pressure to characterize the compressor rotor. Figure A2.2 is a picture of the PIV hardware installation. The detailed characteristics of the hardware used for PIV are presented in Table A2.1 to Table A2.3 at the end of this Appendix. The seeding particles were brought into the gaspath through a series of seeding rakes as shown in the figure. The laser was also redirected in the gaspath by means of a lens designed for the application. A window placed directly over the compressor blades allowed the CCD camera to capture the flow images for PIV data processing. A detailed view of the camera window and laser lens is provided in Figure A2.3 (a). Figure A2.3 (b) shows a tool that was designed to allow modification of the laser plane height to gather data at different blade span locations.

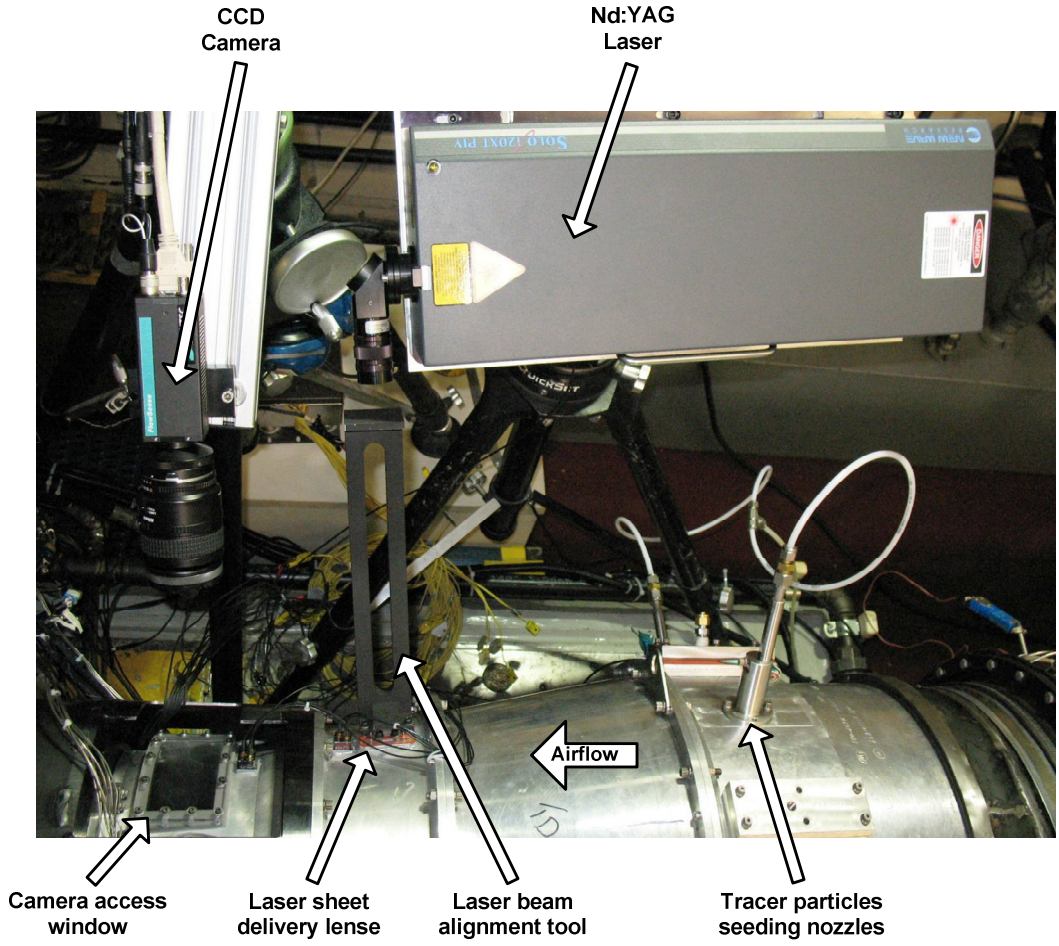

Figure A2.2 : Overview of PIV equipment and installations

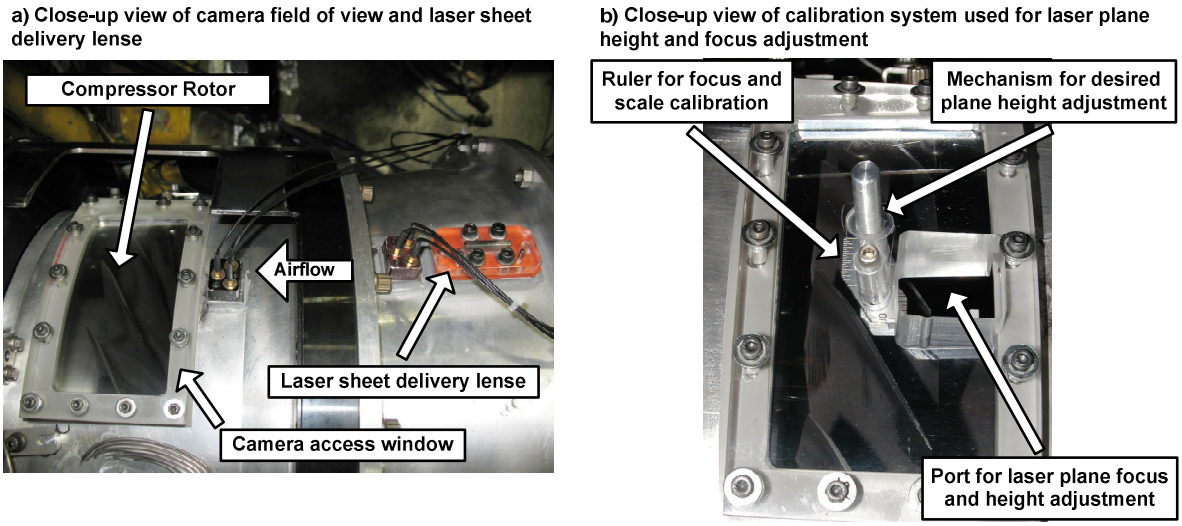

Figure A2.3 : Detailed view of PIV installations, a) close-up view of field of view and laser sheet delivery lense and b) detailed view of the calibration system

A CAD cross-sectional view of the PIV test-section is presented in Figure A2.4 (a). A laser light sheet, perpendicular to the radial direction, was brought into the compressor gas path through a lens. Olive oil was used as the seeding material and brought into the compressor gas-path using a series of seeding nozzles. Three different co-radial planes, located at 94%, 96% and 98% blade span, were investigated at different speeds and operating temperatures. A detailed CAD view of the co-radial plane locations is shown in Figure A2.4 (b).

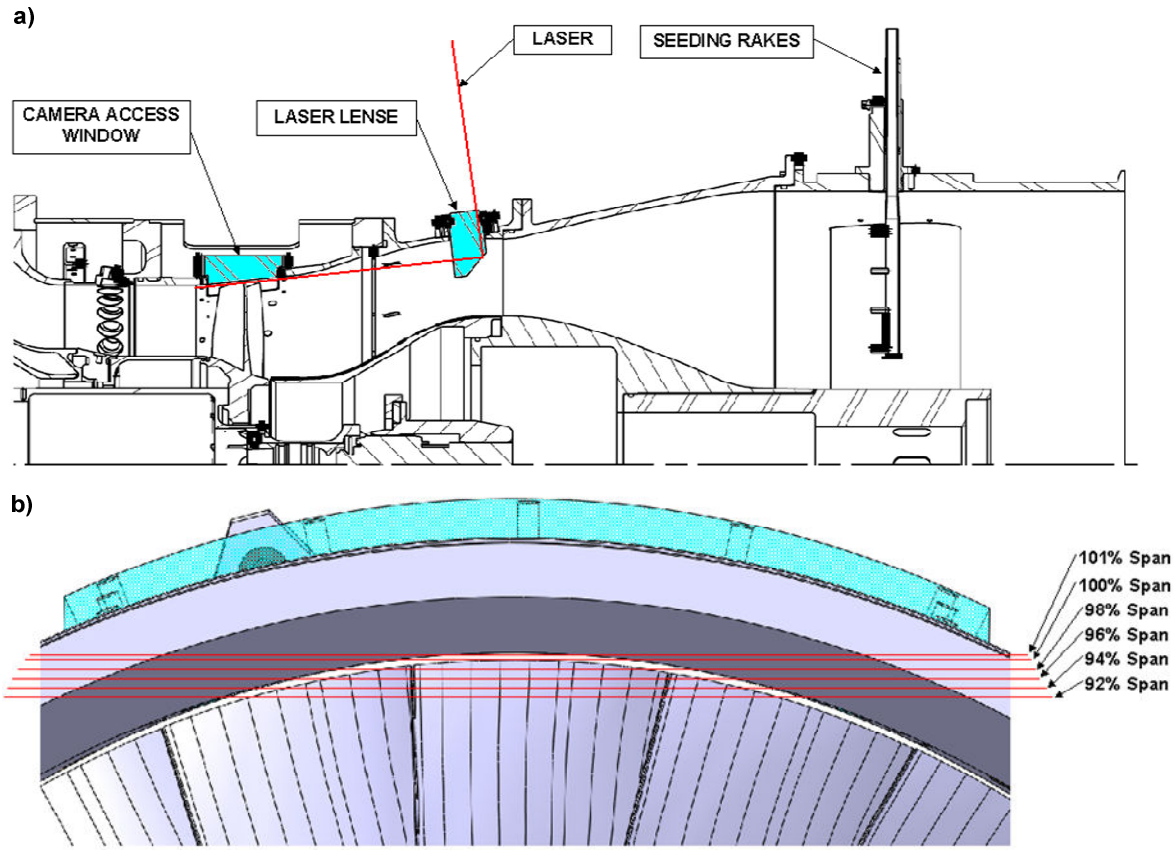

Figure A2.4 : CAD view of PIV experiment: a) detailed view of test-section and b) co-radial PIV measurement planes shown in % blade span

Experimental PIV Results Near Stall

As previously explained the flow measurements were performed at three different co-radial planes, located at 94%, 96% and 98% blade span, and were investigated at different speeds and different operating temperatures. An example of the results obtained at high loading conditions, near stall, is shown in Figure A2.5 (a), (b) and (c) for the 98%, 96% and 94% blade span co-radial planes, respectively. The vector fields shown were converted in the relative frame of reference from the data measured in the absolute frame of reference.

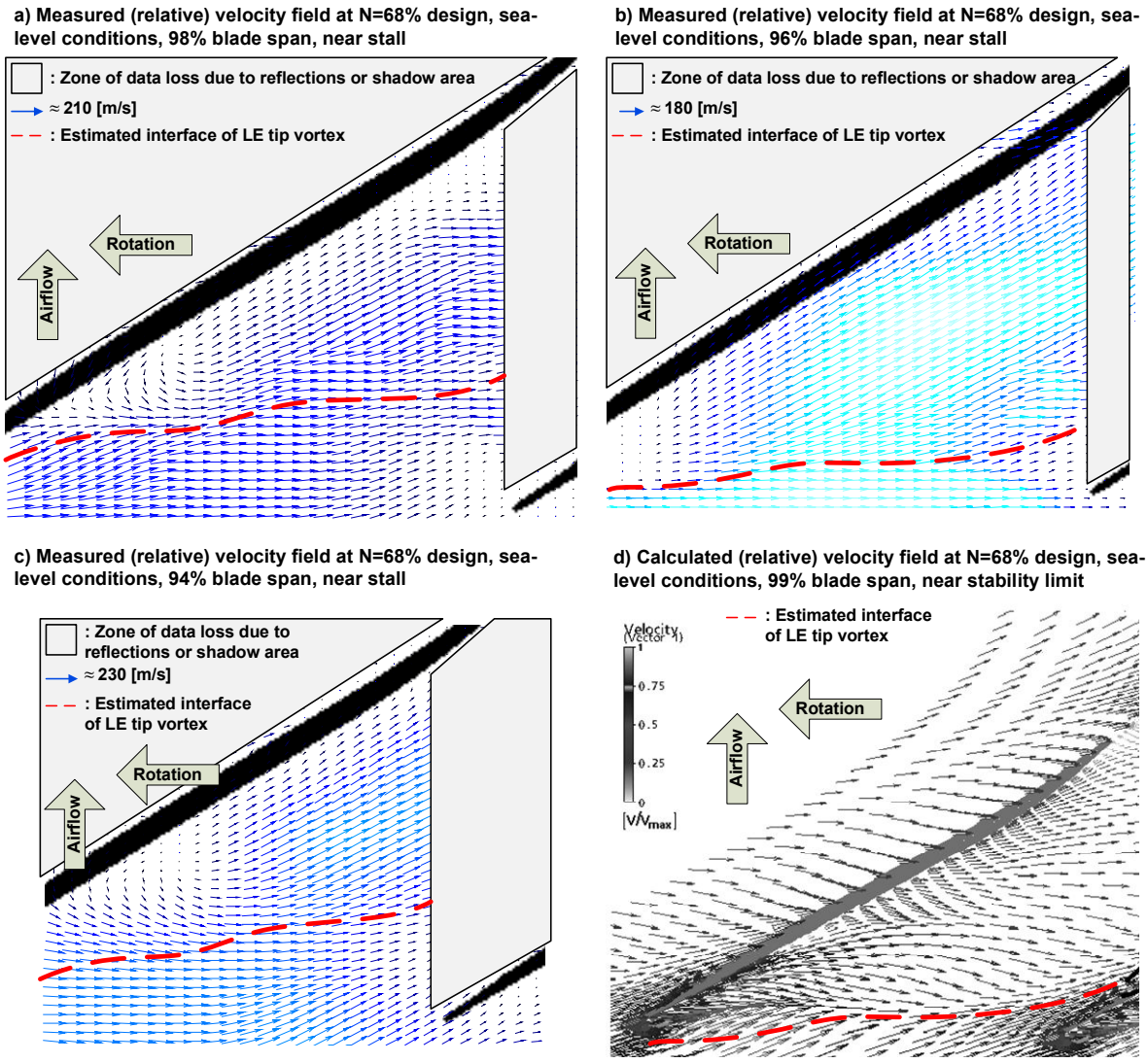

Figure A2.5 : Example of PIV experimental results obtained at sea-level conditions for N=68% design measured at a) 98%, b) 96% and c) 94% blade span co-radial planes. Shown in d) is equivalent numerical results calculated at 99% span co-axial plane.

The interface between the incoming flow and the leading edge tip vortex is approximated from the vector field by the dashed line on the figures. Also shown in Figure A2.5 (d) is comparable numerical results calculated for the same operating conditions. It should be noted, however, that the numerical and experimental vector fields are not directly comparable since the vector planes from the experiment are co-radial (ref. Figure A2.4b) while the plane shown in the numerical results is co-axial. The results shown are also in agreement with that found by Xianjun *et al*.

(2003). This suggests that the leading edge tip vortex tends to be tangential and be redirected towards the upcoming blade near stall, as also observed by Vo *et al*. (2005) as one of the criteria for spike-type stall. The latter could thus possibly act as an impinging jet on the upcoming blade in such conditions, in agreement with the proposed NSV model of Thomassin *et al*. (2008, 2009).

Hardware Specifications from the PIV Experiment

Table A2.1 : Specifications of PIV Nd:YAG laser

Characteristic	Value	Units
Brand	New Wave	[--]
Model	Solo PIV	[--]
Wavelength	532	[nm]
Energy	120	[mJ]
Stability	+/- 4	[%]
Pulse width	3-5	[nsec.]
Beam divergence	< 2	[mrad]
Beam pointing	< 100	[µrad]
Jitter	+/- 5	[nsec.]
Beam diameter	4.5	[mm]

Table A2.2 : Specifications of PIV CCD camera

Characteristic	Value	Units
Brand	Dantec Dynamics	[--]
Model	Flow sense 2M	[--]
Capter type	Charged-Coupled Device	[--]
Spatial resolution	$2E^6$	[pixels]
Image sensor size	1599x1185	[pixels]
Frame rate	15	[double-
Output	8	[bits/pixel]
Lense	Nikon	[--]
Lense model	AF micro 60mm f/2.8	[--]

Table A2.3 : Specifications of PIV seeding system

Characteristic	**Value**	**Units**
Brand	PIVtec	[--]
Model	30	[--]
Operating principle	Laskin	[--]
Seeding material	Olive	[--]
Max. operating	3	[bar]
Particle size (peak	1	[μm]
Max. particle flow	10^8	[part./sec.]

APPENDIX 2 – GT2009-59074: Numerical Investigation into Non-Synchronous Vibrations of Axial Flow Compressors by the Resonant Tip Clearance Flow

Proceedings of ASME Turbo Expo 2009: Power for Land, Sea and Air
GT2009
June 8-12, 2009, Orlando, Florida, USA

GT2009-59074

NUMERICAL INVESTIGATION INTO NON-SYNCHRONOUS VIBRATIONS OF AXIAL FLOW COMPRESSORS BY THE RESONANT TIP CLEARANCE FLOW

Martin Drolet
Jean Thomassin
Pratt & Whitney Canada
Longueuil, Québec, Canada

Huu Duc Vo
Njuki W. Mureithi
École Polytechnique de Montréal
Montréal, Québec, Canada

ABSTRACT

This work investigates Non-Synchronous Vibrations (NSV) encountered in a turbine engine axial flow compressor using a Computational Fluid Dynamics (CFD) approach. It has been proposed that the resonance of the tip clearance flow in compressor blades could be the physical mechanism behind NSV. This work's emphasis is on being able to computationally capture this resonance and predict the critical NSV speed using CFD. This would considerably reduce the costs involved in future hardware design and testing. The model uses the same compressor blade geometry on which experimental validation of the proposed NSV theory was conducted. The flow interaction with blade vibratory motion is modeled using a moving mesh capability and a SAS-SST turbulence model is used for computation.

A review of the proposed theory on NSV is done. The CFD model is first verified with experimental data and then characterized to ensure that the simulations are conducted at the proper NSV conditions, in order to assess the resonance of the tip clearance flow. Evidence of this resonance behavior is presented and critical NSV speeds are identified based on numerical results for two different inlet temperature cases and are validated against experimental data. Further study of the actual flow structure associated with NSV is done. Additional remarks on the numerical results are discussed. An iterative design methodology to account for NSV is also proposed based on the current numerical study.

NOMENCLATURE

A : Blade tip displacement amplitude

c : Local speed of sound

C_a : Mean axial velocity

CFD : Computational fluid dynamics

C_p : Specific heat at constant pressure

EO : Engine order (1,2,3,…)

f : Frequency

FOR : Frame of reference

k : Instability convection constant

LE : Leading edge

M : Mach number

n : Harmonic integer number

N : Rotor speed

NSV : Non-synchronous vibrations

p' : Pressure fluctuation

PR : Pressure ratio

PS : Pressure side

R_s : Specific gas constant

s : Blade pitch

S' : Vibration level

SS : Suction side

T : Torsional vibration mode, Temperature

TE : Trailing edge

U_{tip} : Blade tip velocity

ω : frequency of flow unsteadiness

W_{corr} : Corrected air mass flow

γ : Specific heat ratio

ϕ : Flow coefficient

Ψ : Stage loading coefficient

ξ : Hub-to-Tip ratio

Subscripts

B,F : Backward, Forward wave in rotating frame

b : Blade

c : Speed of sound, Critical

h,t : Hub, Tip

INTRODUCTION

Background

Flow-induced vibrations (FIV) are caused by the interaction of the unsteady aerodynamic loading on a structure and the structure itself. Several types of FIV exist in turbomachinery and can be generally classified into two categories, which are Forced Response and Fluid-Elastic Instabilities. The latter regroups, among others, classical flutter and Non-Synchronous Vibrations (NSV). A number of industry NSV cases have been reported [1,2,8], in the front stages of axial compressors. However, the physical mechanism underlying NSV is not yet fully understood.

Previous studies [2,3,4] have suggested that the tip clearance flow oscillations, could explain NSV and that these flow oscillations are likely to occur at large tip clearance and high aerodynamic blade loading. Mailach et al. [4] have observed instabilities in the blade tip vortex that evolves in a blade passage. Theses instabilities could involve impingement of the tip clearance flow on the pressure surface of the adjacent blade. In addition, Vo et al. [5] showed that two criteria must be satisfied to set the spike-initiated rotating stall point. These are leading edge tip clearance leakage and trailing edge tip clearance backflow. Vo [6] also showed that the flow oscillations at the blade tip, potentially linked to NSV, can occur when only one of the two criteria for stall inception is satisfied. Furthermore, he suggested that these rotating instabilities could arise from the impingement of the tip clearance flow leakage on the blade pressure side, as shown in Figure 1, and that the study of the dynamics of impinging jets could explain NSV.

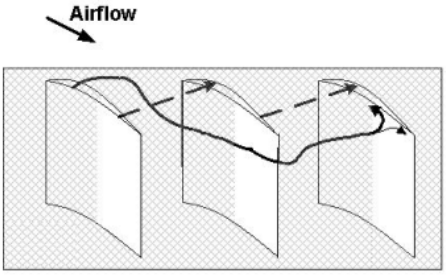

Figure 1: Tip clearance flow impingement flow paths [9]

The Jet-Core Feedback Theory

Thomassin et al. [8] have revisited the physics of the impinging jet on a flat plate of Ho et al. [7]. In their set-up the plate was flexible and vibrating, to simulate a cantilevered rotor blade, as opposed to Ho et al. [7], and thus allowed pressure fluctuations at the stagnation point, in the jet centerline. This created an additional feedback within the jet potential core. The proposed jet-core feedback theory is illustrated in Figure2a. From this experiment, it has been shown that resonance of a jet impinging on a flexible plate is possible for a jet speed representative of the tangential velocity component present at the blade tip during NSV.

This novel jet core feedback theory [8] was then applied to compressor blades as depicted in Figure2b and c. At particular operating conditions [9], it was suggested that the resonance of the tip clearance flow could be the physical mechanism behind NSV [8,9].

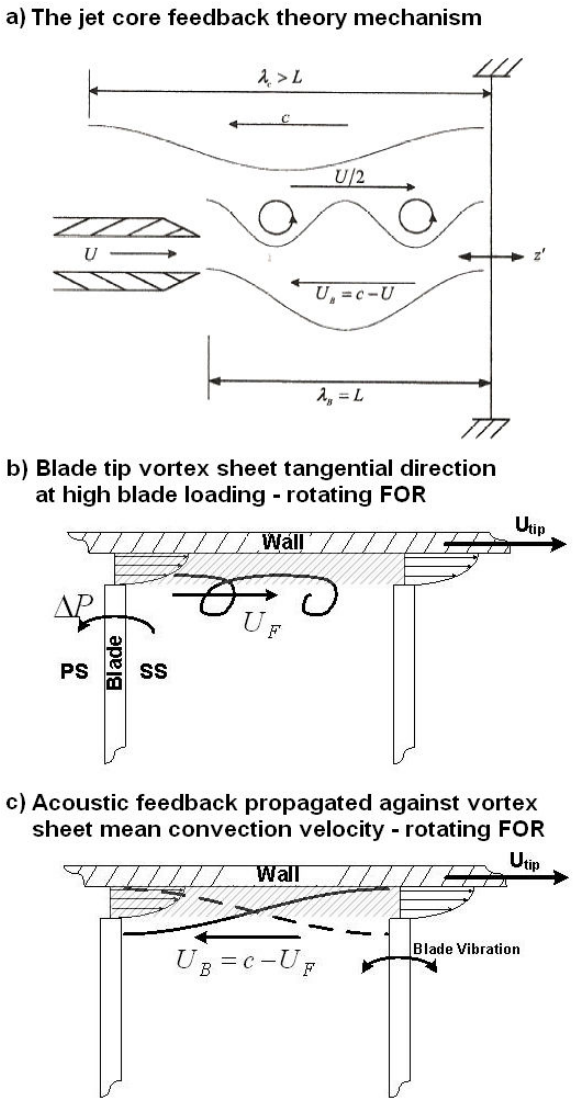

Figure 2 : a) The jet core feedback theory model [8] , b) and c) the model applied to NSV on compressor blades [9]

The tip clearance flow resonance will only occur if two conditions are satisfied. First, the compressor must operate at high aerodynamic loading, such as near-stall conditions, since this is where the tip clearance flow can evolve tangentially and possibly act as an impinging jet on the adjacent blades. Secondly, the local speed of sound at the blade tip must be adequate for the acoustic feedback from the adjacent blade vibrations to travel back and synchronize the tip clearance shear layer instability, thus causing the resonance of the tip clearance flow. An equation was derived based on this theory [8], here shown as equation (1), to predict the critical rotor speed at which NSV can occur.

$$U_{tipc} = 2\left(c - \frac{2sf_b}{n}\right) \tag{1}$$

where U_{tipc} is the critical blade tip speed, c is the local speed of sound, s is the blade pitch, f_b is the blade natural vibration frequency and n is an integer related to the harmonics of the acoustic feedback wave. Equation (1) was statistically verified on a number of cases for which the compressor blades exhibited NSV [8]. The predicted critical NSV tip speed showed good agreement with the available data. The proposed NSV resonance condition, as described above, has also been experimentally demonstrated on a compressor rotor known to exhibit NSV [9]. Equation (1) was reformulated in terms of the blade tip speed as a function of the blade frequency, which gives

$$\frac{U_{tipc}}{\sqrt{T_{tip}}} = k\left(\sqrt{\gamma R_s} - \frac{2\,s\,f_b}{n\sqrt{T_{tip}}}\right) \tag{2}$$

where $k = U_{tipc}/U_F$ with U_F defined as the forward travelling wave convection velocity in the rotating frame of reference. In the general case, when accurate calculation or measurement of k are unavailable, the approximation $k = 2$ can be used in equation (1).

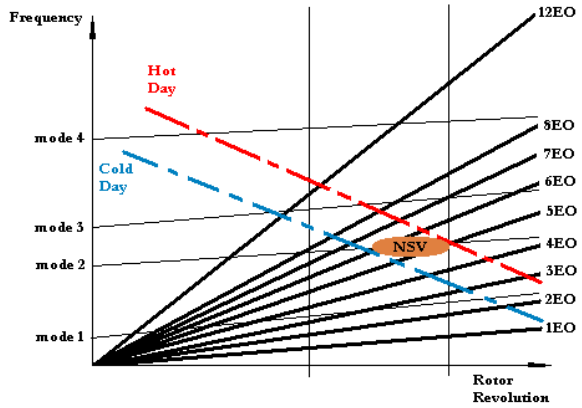

Figure 3 : NSV prediction on campbell diagram

This relation is represented as a negative-slope curve, which is a function of the running temperature, on the Campbell diagram. The application is shown by the dashed lines in Figure3. It can predict a range of possible NSV events on the diagram, for a given temperature range. The classical engine order crossings are also shown on the figure for reference.

Numerical Investigation

Previous numerical studies on the NSV phenomenon have been reported. Examples can be found in [2,3,6,13]. The current numerical study investigates NSV using a CFD approach with three main objectives. The first is to demonstrate that the tip

clearance flow resonance can be captured using a simple single row, single passage unsteady CFD simulation with a moving mesh capability. The second objective is to show that the unsteady pressures behavior can be used as a design tool to predict the experimental [9] critical NSV speeds for the rotor under study. Finally, the third objective is to extend our understanding of the relevant fluid mechanics by investigation of the simulated flow field at peak tip clearance flow resonance conditions.

The paper is organized as follow: a detailed description of the numerical simulations is first given. A summary of the experimental investigation [9] performed on the rotor under study is then presented. Thereafter, the simulation results of two validation cases are presented and compared to experimental data. A discussion of the results is carried out on evidence of tip clearance flow resonance and computational prediction of critical NSV speeds. The fluid mechanics associated with NSV are also studied and a design methodology to account for NSV is proposed. Lastly, conclusions are drawn from the investigation.

COMPUTATIONAL SET-UP

Simulations

All simulations were performed using the commercial code ANSYS CFX (release 11.0) in transient mode.

Geometry & Mesh Description

The current study uses the same rotor geometry that was used by Thomassin et al. [9] in their experiment. A single row, single blade passage with a periodicity condition is used in the computations. The complete rotor geometry and a close-up of the single blade passage computational domain are depicted in Figure4a and b respectively. The blade pitch (s) is close to 89% of the chord length at the hub and the hub-to-tip ratio (ξ) is approximately 0.47. The tip clearance is set at 2% of the tip chord to match one of the pertinent experimental conditions. Also note that the rotor is isolated (i.e. no inlet guide vanes and stators) to recreate the experimental conditions in [9]. The simulated ducts upstream and downstream of the blade passage are least one blade pitch long. This allows for potential flow perturbations in the blade passage to decay to zero amplitude at the inlet and exit domain boundary. A short mesh study was performed and lead to a mesh with about 125 000 nodes using a no-slip wall function, for which simulations were successfully carried out with and without blade motion.

Turbulence Model

The SAS-SST (Scale Adaptive Simulation – Shear Stress Transport) turbulence model and method is used for all unsteady simulations in the present work to capture the relevant fluid mechanics associated with the NSV phenomenon.

A) Full annulus (23 periodic passages)

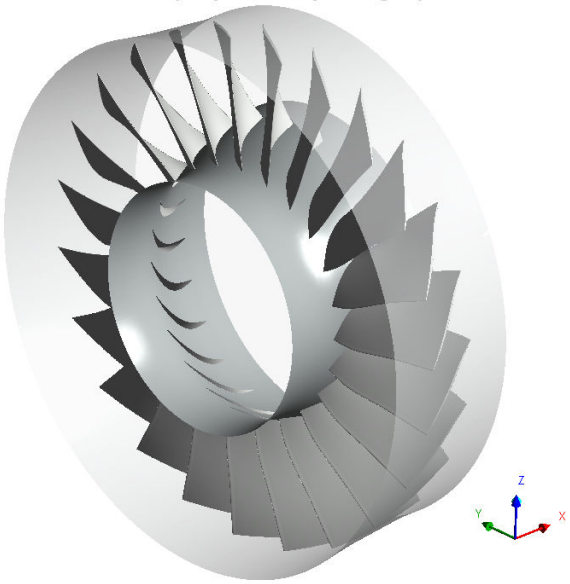

B) CFD model - Single blade passage geometry

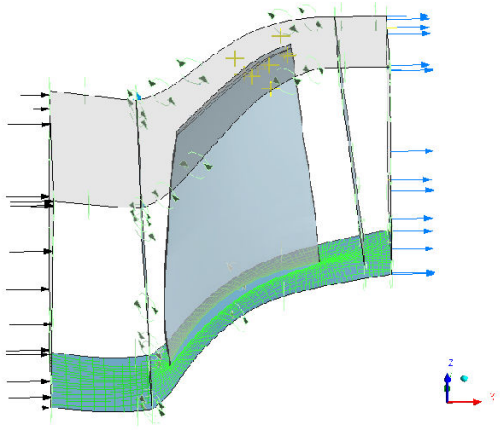

Figure 4 : a) Complete rotor geometry b) Single blade passage used for simulation

Mentor and Egorov [10] applied this method to a wide variety of problems and demonstrated its advantages. Namely, it captures the unsteady flow features more accurately than the standard SST-URANS method and is also less grid-sensitive than other methods such as LES (Large Eddy simulation) or DES (Detached Eddy Simulation). Thorsten and Othmer [11] have also performed aero-acoustic simulations using the SAS-SST turbulence model since for these types of simulations, the vortex structures of

the flow-field must be accurately resolved. The model was also applied to jet-edge tone simulations [12], which involve similar physical phenomena as the proposed NSV mechanism [8,9].

Boundary Conditions

The boundary conditions used in the simulations consisted of specified total pressure, total temperature and swirl angle at the domain inlet and average static pressure at the domain exit. To reproduce the experimental conditions from reference [9], a zero degree inlet swirl angle and two inlet temperatures (T1), one hot one cold, were used. The exit pressure was increased to obtain points along a speedline to characterize the compressor and approach the near-stall conditions associated with NSV.

Moving Mesh Capability

Blade vibrations associated with the resonance of the tip clearance flow are modeled using the moving mesh capability of the commercial CFD code used. A mesh displacement was imposed to the model, according to equation (3), in the tangential (y) direction of the relative frame of reference,

$$y(x,z,t) = A \cdot \sin(2\pi f_b t) \cdot \frac{(z - r_h)}{(r_t - r_h)} \cdot \frac{(x - x_m)}{(x_{TE} - x_{LE})} \quad (3)$$

where A is the displacement amplitude of the blade tip, which is kept constant for all simulations at around 0.5% of the chord, f_b is the blade vibration frequency and t the simulation time. The prescribed blade displacement scales with a factor that is a function of the radial (z) position, hub radius (r_h) and tip radius (r_t). Since the hub radius (r_h) varies with the x position, the hub radius at the mean x position is used in equation (3). This results in negligible leading edge and trailing edge displacements at the hub. A second factor that is a function of the axial position x, x mean (x_m) and x at leading edge and trailing edge (x_{TE} and x_{LE}) also gives the maximum displacement at blade tip. All together, equation (3) reproduces a torsional oscillatory motion, similar to the 1st torsional mode (1T) associated to the geometry and the proposed NSV model [8,9]. Since we were only looking at the fluid response to the blade vibratory motion, this approximation was found satisfactory for the purpose of our study.

A time-step value 44 times lower than the period associated with the maximum blade vibration frequency of interest, associated with the blade's first torsional mode (1T), was used for simulations to provide an adequate sampling frequency to capture the desired NSV phenomenon.

EXPERIMENTAL RESULTS OVERVIEW

Experimental investigations of the rotor under study have been made by Thomassin et al. [9]. A summary of the relevant measured data for the current work is presented here.

Figure5a shows vibration measurements of the same 1T mode for several instrumented blades during the experiment. Vibration values have been recorded at increments of about 1% of the rotor design speed ranging from around 65% to 82% for two different inlet temperatures, one cold and one hot. A polynomial curve fit (solid curves) of the data suggests that the maximum stress value during NSV was at approximately 68% and 73% of the rotor design speed for the cold and hot inlet temperatures, respectively.

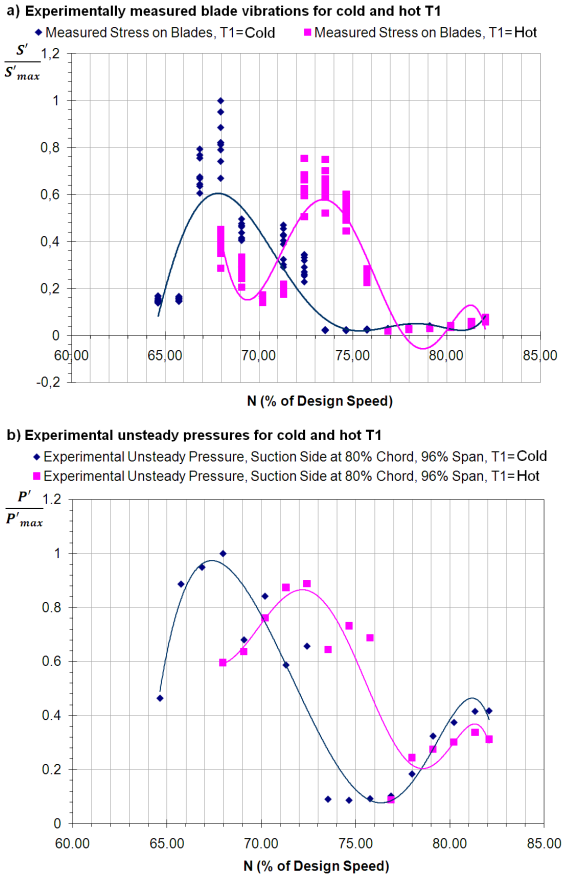

Figure 5 : a) Measured vibrations at various locations on blades b) Unsteady pressure measurements on blade

Figure 5b shows the simultaneously taken unsteady pressure measurements at locations near 80% chord and 96% span on the rotating blade. Again, a polynomial curve fit suggest that the peak pressure during NSV occurred around 68% and 73% of the rotor design speed for cold and hot inlet temperatures, respectively.

In addition, an average temperature at the shroud was measured and can be approximated as the blade tip local temperature to calculate the local speed of sound. Measurements allowed detailed analysis of the blade unsteady pressure (in the rotor FOR). The data revealed that the convective velocity U_F is around $0.61U_{tip}$ [9], which is not far from the approximation of $0.5U_{tip}$ used in Figure 2b.

The critical NSV speed can be found using equation (2) with k=1.6394, corresponding to U_F=$0.61U_{tip}$. The critical NSV speed was predicted to be 66.72% and 71.26% of the rotor design speed for the cold and hot inlet temperatures, respectively. Thus, the experimental results were found to be within 2-3% of the predictions by equation (2).

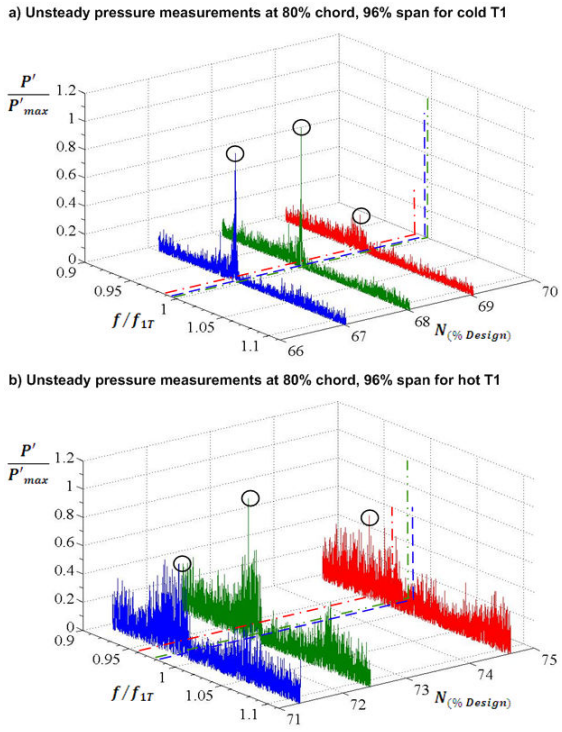

Figure 6 : Frequency analysis of experimental unsteady pressure measurements on blade SS at 80% chord, 96% span vs rotor speed for a) cold T1 b) hot T1

The unsteady pressures of Figure 5b shows a good correlation with the vibration levels of Figure 5a. The unsteady pressure fluctuations are therefore used as a metric for the current numerical study to predict the critical NSV speed.

Figure 6 shows the measured unsteady pressure in the frequency domain (normalized by the frequency of interest) as a function of the rotor speed for both cold and hot inlet temperatures. It shows that the normalized amplitude of the peak unsteady pressure fluctuations in the frequency domain is increasing in a manner consistent with a resonant behavior around the blade first torsional vibration mode (1T) frequency for both cold and hot inlet temperatures (6a and 6b, respectively). This also happens at rotor speeds around the NSV critical speed predicted by equations (1) and (2), suggesting that the tip clearance flow is in resonance during the maximum amplitude NSV.

In light of the foregoing, a frequency analysis of the numerical unsteady pressure fluctuations will be used to assess the tip clearance flow resonance.

NUMERICAL RESULTS AND DISCUSSION

Numerical Model Verification

The numerical model was first verified against experimental data to show that the simulations reasonably predict the aerodynamic performance of the rotor. Figure 7 presents the rotor loading ($\Psi=(C_p\Delta T_o)/(U_{tip}^2)$) at the blade tip as a function of the flow coefficient ($\Phi=C_a/U_{tip}$) for all numerical results performed with blade motion. Experimental data are shown for reference.

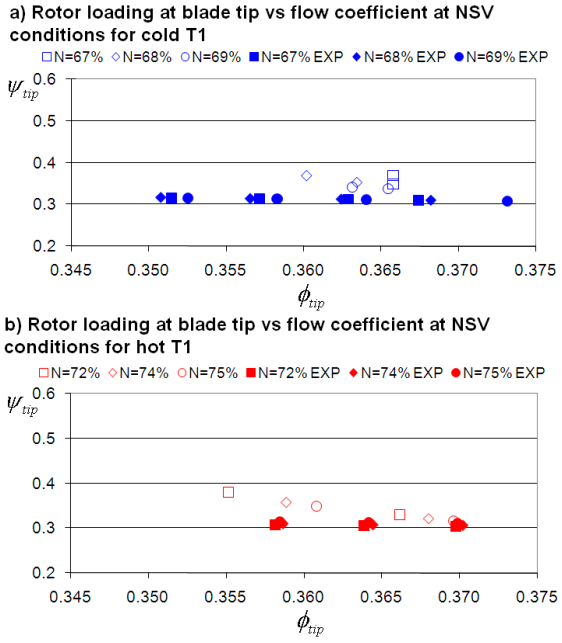

Figure 7: Experimental [9] and numerical blade tip stage loading vs flow coefficient at NSV conditions for a) cold T1 and b) hot T1

The agreement between numerical and experimental data was judged to be satisfactory and it was concluded that the model fidelity was adequate for the purpose of this study, which focuses on capturing the flow physics and not the exact compressor performance.

The rotor under study was also characterized for the different desired operating conditions. This was done

by performing simulations while varying the average outlet static pressure and letting the solution harmonically stabilize. A compressor map of the rotor was then built to give information on the pressure ratio and corrected mass flow.

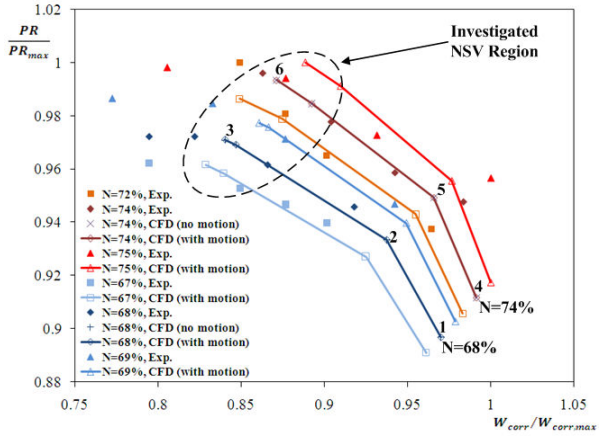

Figure 8 : Unsteady CFD compressor mapping

Figure 8 shows the compressor map based on roughly time-averaged numerical results on which the values of pressure ratios and corrected mass flow are normalized to the maximum values. Speed lines (solid lines) are curve-fitted for the different simulation cases. Experimental measurements are also shown for reference. The compressor map of Figure 8 aims to show that the simulations are conducted in the proper NSV region, near-stall (circled on the figure), that was experimentally identified [9].

Evidence of Tip Clearance Flow Resonance

Unsteady pressure can be monitored at several locations near the blade tip during simulations to capture any form of tip clearance flow resonance. The effect of aerodynamic loading is investigated in Figure 9 while the effect of rotor speed is shown in Figure 10. The resonant behavior is observed at several points as the pressure ratio is increased on the speed lines shown in Figure 8. An example of the unsteady pressures amplification at the blade tip, in the frequency domain, is shown in Figure 9a for operating points 1,2,3 on the 68% speed line (ref. Figure 8). Unsteady pressure data were taken on the blade pressure side at about 84% tip chord and 97% span at different points along the speedline. In addition, a time function of unsteady pressure simulation is shown on Figure 9b for points 1 (outside NSV region) and 3 (inside NSV region) on the 68% speed line. Data was taken on blade suction side at about 80% chord and 96% span. The latter shows that the pressure takes more time to stabilize during NSV. Similar results (not shown) for Figure 9a and b were obtained for the other monitor points locations and simulated rotor speeds.

It is also important to note that the peak unsteady pressure occurs at the blade vibrating frequency, in agreement with a resonant behavior. Moreover, low unsteady pressure amplifications at more or less random frequencies were found in the rigid blade simulations. Although most previous studies [2-5] have investigated NSV assuming a forced response with no motion, Figure 9a suggests that the blade vibration is necessary to induce the tip clearance flow resonance which is consistent with a fluid-elastic interaction. It was also suggested in [13] that blade motion is advantageous in NSV design considerations. Further evidence of the resonant behavior of the tip clearance flow is found when going through the NSV condition by varying the tip speed on a similar compressor operating line in the NSV region of Figure 8.

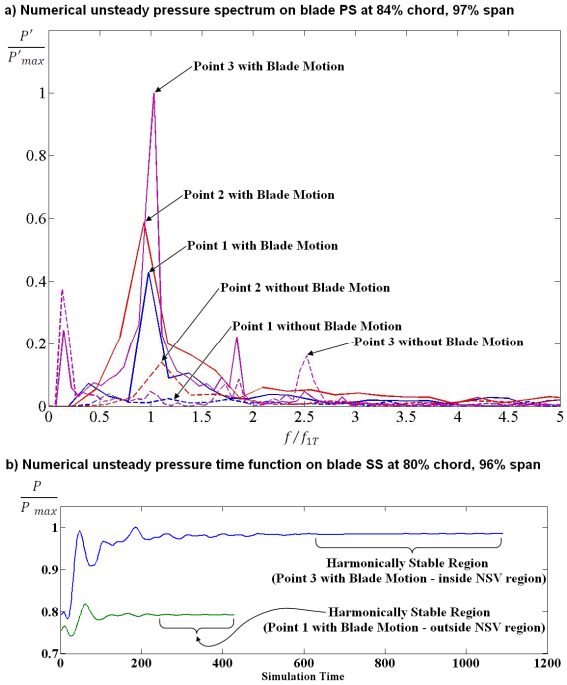

Figure 9 : a) Unsteady pressure fluctuations spectrum near blade tip PS at 84% chord, 97% span and b) unsteady pressure time function on blade SS at 80% chord, 96% span for N=68%

Figure 10a shows the numerical results of the normalized amplitude of the pressure fluctuations, at 80% chord and 96% span, in the frequency domain at three neighboring speeds in the NSV region for the cold inlet temperature. Also in Figure 10b is equivalent data for the hot inlet temperature. Similar behavior was obtained for other monitor points locations. It can be seen that as the rotor speed approaches the critical NSV speed, the pressure fluctuations are showing signs of resonance, with the highest peak near the critical NSV speed. These observations support the resonance of the tip clearance flow as the mechanism

behind NSV, as suggested in [8] and experimentally shown in [9].

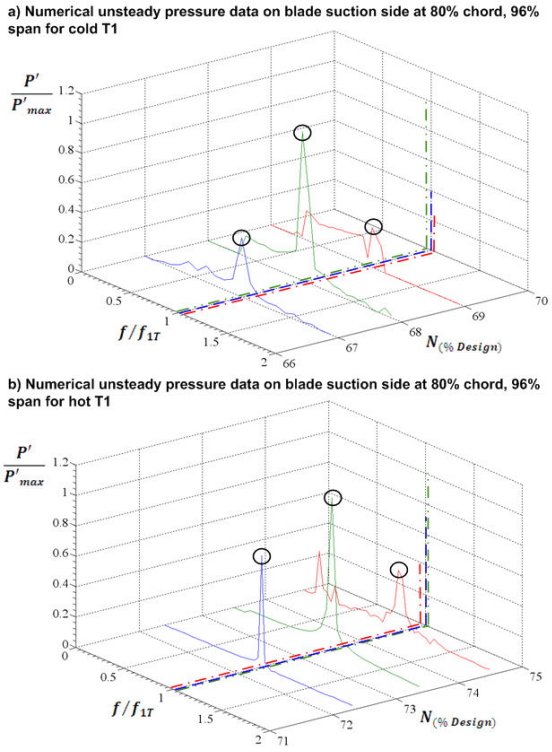

Figure 10: Frequency analysis of numerical unsteady pressure measurements on blade SS at 80% chord, 96% span for a) cold T1 b) hot T1

Resonance Prediction from Numerical Results

The resonant condition of the tip clearance flow as defined in [9] can be obtained from equation (1) in its general form: $U_F=c-(2sf_b/n)$, that is, without the assumption of $U_{tip}/U_F=2$. The resulting equation is shown here as equation (5) and can also be verified from the current numerical model solutions.

$$\frac{(c-U_F)}{2sf_b}=1 \qquad (5)$$

The local speed of sound, c, near the blade tip, where the impingement condition has been numerically observed, can be found from the numerical results using the corresponding local temperature. The convective speed U_F is found from averaging the tip clearance flow tangential velocity at ten equally spaced locations along the tip chord length. Figure 11 shows the pressure fluctuations from CFD computations normalized to the maximum observed value and the normalized measured stress [9], both as a function of $(c-U_F)/(2sf_b)$. The closest numerical data points from the predicted NSV resonance condition, $(c-U_F)/(2sf_b)=1$, for both cold and hot inlet temperatures, corresponds to the points with the highest pressure fluctuations. The numerical data shows that the resonance condition is met during NSV, which is in agreement with the experimental results [9]. Figure 12 shows the calculated values of U_F/U_{tip} as a function of the flow coefficient. The calculated average value of 0.64 is close to the experimental value of 0.61 found in reference [9].

The numerical prediction corresponds to k=1.5625 in equation (2). This value and the numerical results of the blade tip temperature for the solutions near the resonance condition are used in equation (2) to predict the critical NSV speed. The resulting predictions, N=63% for the cold T1 and N=68% for the hot T1, are within 4 to 6% error of the experimental data. This suggests that the current CFD model is operating in the correct NSV condition and that the phenomenon of interest is being captured.

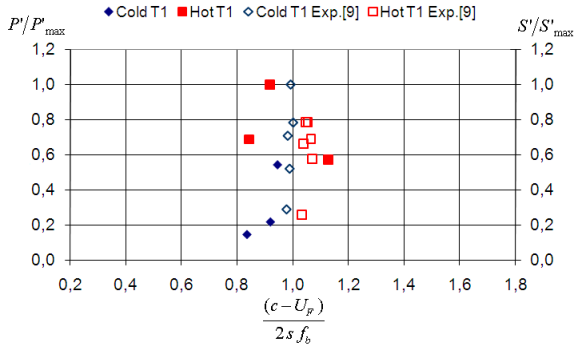

Figure 11: Resonance condition predictions: CFD unsteady pressure (CFD) and measured stress (exp. [9]) vs resonance condition

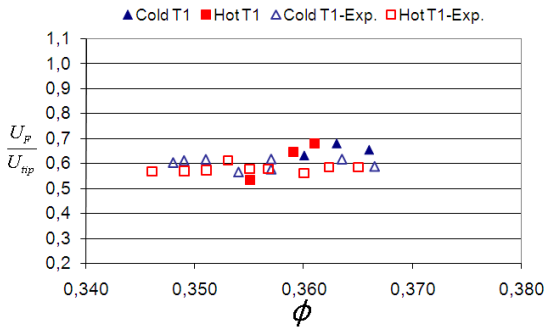

Figure 12: Numerical and experimental [9] predictions of convection velocity U_F vs flow coefficient Φ

Figure 13 shows the peak unsteady pressure on the blade during resonance condition as a function of the rotor speed (in % of design value) for all simulations. Taking the peak NSV to be at each maximum of the two curve fits (dashed curves), the predicted NSV critical speeds are N=67.9% for the Cold T1 and N=73.6% for the Hot T1. These results, again, show

very good agreement, in terms of critical NSV speeds, with those predicted based on Figure 5b, having less than 1.5% error. It should be noted, however, that the pressure amplitudes in Figure 13 do not match those of Figure 5b. The fact that the mode shape and displacement amplitude of the blade motion are approximate might explain why the numerical amplitudes in pressure fluctuations do not match the experimental ones.

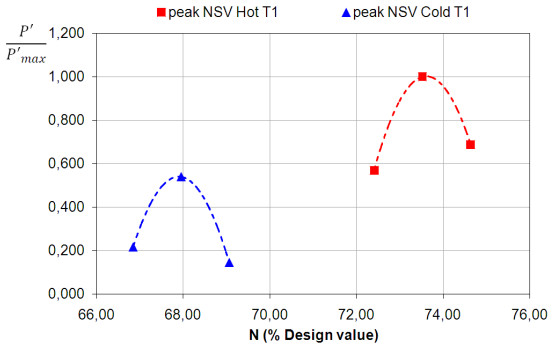

Figure 13: Critical NSV speed predictions from numerical peak unsteady pressures

Table 1 presents a summary of the relevant experimental and numerical critical NSV speed (N_{cr}) predictions for comparison. As previously explained, the critical NSV speed is predicted using two independent methods. The first method uses equation (2) with the value of k either estimated, obtained from experimental data or averaged from the tip clearance flow field of CFD simulations whether with non-moving mesh (standard) or with moving mesh (present case). The second method consists of CFD simulations with moving mesh to determine the critical NSV speed from unsteady pressure data (ref. Figure 13). The first method can be used to narrow the range of speeds in which the CFD simulations are carried out for the second method.

Table 1 : Summary of critical NSV predictions

Prediction Method	N (%design) Cold T1	N (%design) Hot T1
Experimental from Figure 5b	68.1 %	72.5 %
Numerical from Figure 13	67.9 %	73.6 %
Eq. 2 with experimental *k*	67 %	71 %
Eq. 2 with numerical *k*	63 %	68 %

The numerical results show good agreement with the experimental data. This demonstrates that a simple single row, single passage CFD simulation with a moving mesh, can accurately predict the critical NSV speed from the resonant behavior of the unsteady pressures at the blade tip.

Observation of Tangential Flow

From the numerical solutions near the resonance condition, it is possible to get insights into the fluid mechanics associated with the NSV phenomenon. As previously mentioned, tangential flow at the tip is necessary to have tip clearance flow resonance. Tangential flow can be observed for the simulation cases near peak NSV critical speed and tends to impinge on the adjacent blade tip. Figure 14 shows a vector plot at 99% span (just below the blade tip) for the hot inlet temperature case at peak NSV (2 passages shown) on which the impingement zone of the tangential flow at the tip is identified. A vector plot and pressure contours at midchord location are shown in Figure 15 which clearly depicts the impingement behavior. This was also observed at other chord locations along the impingement zone identified in Figure 14.

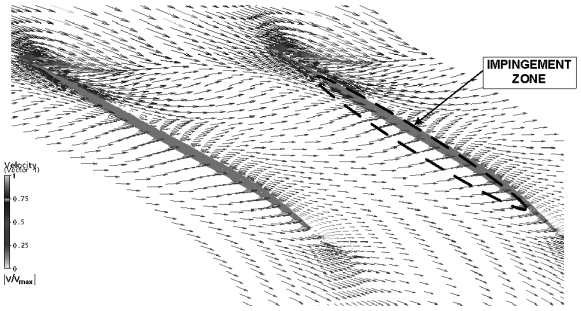

Figure 14: Tip clearance flow impingement zone – hot T1

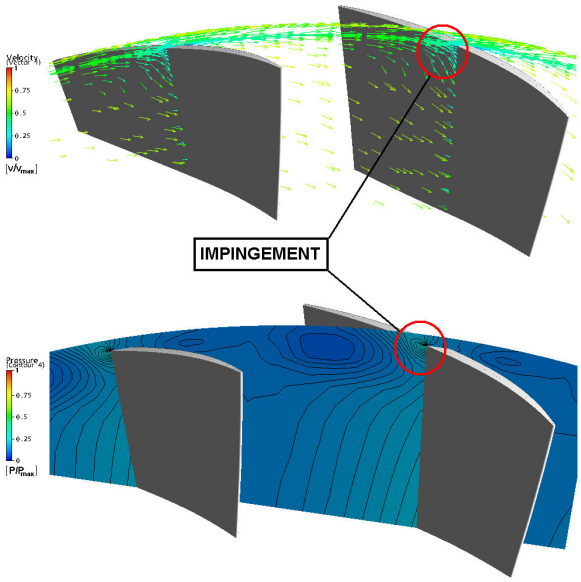

Figure 15: Impingement at midchord – hot T1

It was suggested by Thomassin et al. [8,9] that the blade tip clearance flow could be responsible for NSV. The tip clearance flow structure would evolve tangentially and be convected circumferentially, for the rotor under study for particular running conditions, at a speed $U_F \cong U_{tip}/k$ [8,9]. One can seek for this tip clearance flow structure by creating a vector of the velocity relative to the blades with a tangential component defined as v'= (v - U_{tip}/k). This would circumferentially "freeze" any fluid particle with a main tangential velocity component around U_{tip}/k. Figure 16a shows a streamline plot of this new velocity field. A low momentum structure, apparently the blade tip clearance flow vortex sheet, appears from this plot. This is similar to the observations made by Mailach et al. [4]. This suggests that the structure was moving around the predicted convection speed ($U_F \cong U_{tip}/k$ with $1/k \cong 0.61$ exp.[9] or $1/k \cong 0.64$ numerical) and could be linked to NSV. It can also be observed that the structure path is near tangential and seems to impinge on the upcoming blade pressure side and spills at the tip through the adjacent blade passage.

Figure 16b shows vorticity contours in the relative FOR which agree with the behavior of the tip clearance vortical structures. Figure 16 (c and d, respectively) show the temperature and Mach number contour plots from which average values within the circled region can be obtained. The characteristics of the blade tip vortex sheet can thus be used, as a different approach, to identify the convection velocity U_F. The local speed of sound is obtained from the temperature. Then, from the Mach number, the convective velocity U_F is obtained (assuming $M= U_F/c$). This leads to $U_F/U_{tip} \cong 0.64$ which shows good agreement with predictions of Figure 12 and also from [9]. Hence, this suggests that the blade tip vortex sheet presents the proper characteristics in terms of convective velocity ($U_F/U_{tip} \cong 0.64$) and temperature (sound speed) to be associated with NSV in agreement with the proposed NSV model [8,9]. Note that these observations were also true for the other "off-resonance" simulations since they were also in critical operating regime (tangential flow at tip) but their associated pressure amplifications were less. This may be due to the fact that the blade tip vortical structures were probably not perfectly synchronized with the blade vibration frequency, as expected from the proposed mechanism [8,9].

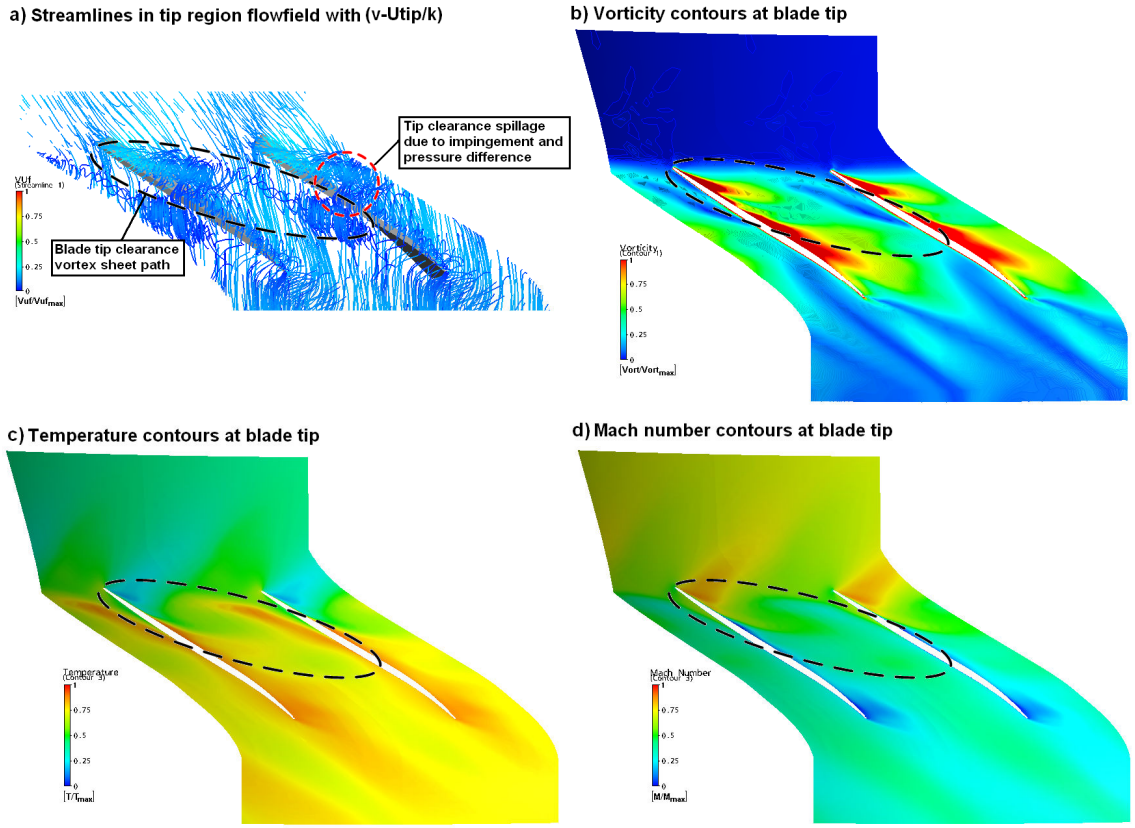

Figure 16: Blade tip vortex sheet characteristics at 99% span for hot T1 at peak NSV

Remarks on the Numerical Study

The current numerical study was conducted using a single blade passage having a periodicity condition that was chosen primarily for its low requirement in computation time and resources. The results from the simulations agree with the proposed mechanism for NSV [8,9] in addition to accurately predicting the critical NSV speed. It shows that a single rotor passage model with a moving mesh can be used to locate the critical NSV condition. Further investigation needs to be conducted to determine the actual size and detailed behavior of the flow structures responsible for NSV. Simulations with multiple passages using a moving mesh with complete fluid-structure interaction and blade finite-element analysis, could perhaps capture both the NSV and the associated blade stress levels. The current model also approximates the mode shape and displacement amplitude at the blade tip which allows accurate prediction of the critical NSV speeds but does not simulate the proper pressure fluctuations amplitude, as previously discussed. Simulations with more accurate representation of the mode shapes and displacement amplitude

may allow to capture the pressure amplification levels more accurately.

Proposed NSV Design Methodology

The relation shown as equation (1) or (2) proposed by Thomassin et al. [8,9] is a powerful and simple tool to determine, as a first approximation, the critical speed at which a given rotor geometry can encounter NSV in particular operating conditions. The computational method used in the current study was found in good agreement with the available experimental data [9] and is proposed here as a complementary design tool to equation (1) or (2).

The suggested iterative design methodology is depicted in Figure 17. The contribution from Thomassin et al. [8,9] and the current work essentially allows the a priori prediction of the critical NSV speeds and is delimited by the dotted line on the figure. First, the critical NSV speeds are determined using equation (2), for a given geometry at particular operating conditions, over a wide range of k values to ensure that all critical speeds are identified. Second, verification is made to determine which critical speeds are in the engine running speed range. Third, unsteady CFD simulations with moving mesh, which only account for the fluid mechanics behind NSV, are performed for several speeds near the identified critical speeds. Fourth, the exact NSV critical speed and a refined k value are identified from the numerical results, based on the method discussed in this work. The identified critical speed is then verified again to see if it is still in the engine running range.

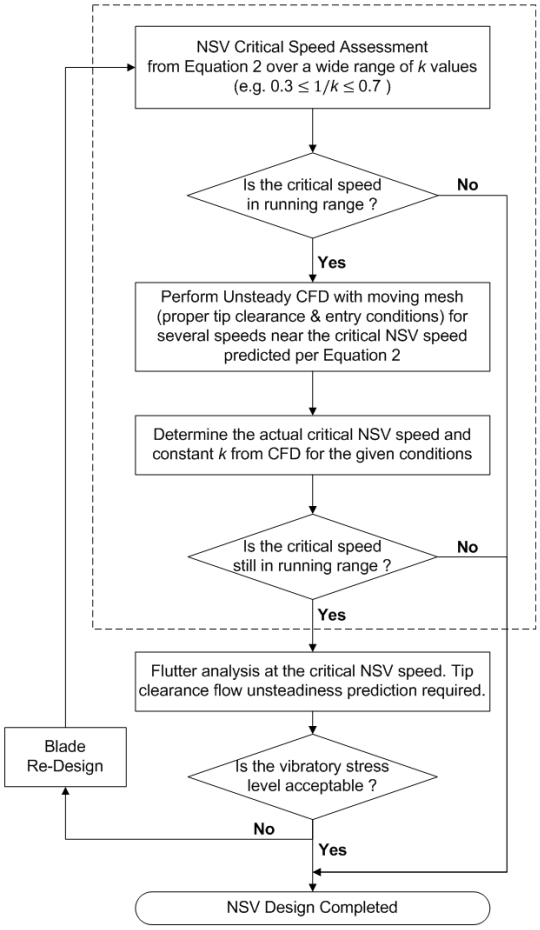

Figure 17: Proposed NSV design methodology

If the critical speed is no longer in the running range, the NSV design process is completed. However, if the predicted critical speed is still in the running range, flutter analysis that would capture the tip clearance flow effect and include stress levels and blade elasticity, shall be conducted to determine whether the blade vibratory stress level is acceptable. The latter is beyond the scope of this paper. If the stress is found unacceptable, the blade geometry is modified and the process of Figure 17 is repeated.

CONCLUSION

A numerical investigation on the proposed NSV mechanism [8,9] has been conducted using a CFD approach. Two validation cases, based on experimental data [9], have been studied. Results are consistent with the experimental data and the proposed mechanism. Evidence of the resonant tip clearance flow as the mechanism behind NSV has been shown. The need for blade motion to get the

resonance behavior was also highlighted. The convective velocity U_F of the flow structure associated with NSV has also been determined and is close to the experimental values. The NSV critical speed was predicted using different approaches and all have shown good agreement with experimental data. A summary of the predictions has been made and shows that the current CFD model, using a single blade passage with a moving mesh, is suitable for critical NSV speed predictions.

Some insights into the fluid mechanics associated with the proposed NSV theory [8,9] were also observed. The jet impingement-like behavior of the tip clearance flow associated with NSV has been identified. Further investigations on the vortical structures associated with NSV were conducted and showed similar behavior to that reported in the literature [4]. The blade tip vortex sheet was also identified with the proper characteristics to be potentially linked to the current NSV model [8,9]. Comments on the current CFD model have been made and suggestions for further numerical NSV investigations discussed. The current numerical study is proposed as a complementary design tool to the analytical relation found in [8,9]. A proposed iterative design methodology to account for NSV is presented.

ACKNOWLEDGMENTS

The authors would like to thank Pratt & Whitney Canada for the authorization to publish this work. The principal author would like to express his personal thanks to Mr. Feng Shi for his advice on numerical simulations and to Pratt & Whitney Canada for supporting this research initiative.

REFERENCES

[1] Baumgartner, M., Kamaler, F. and Hourmouziadis, J., "Non-Engine Order Blade Vibration in a High Pressure Compressor", ISABE Paper 95-7094, 1995.

[2] Kielb, R.E., Thomas, J.P., Barter, J.W. and Hall, K.C., "Blade Excitation by Aerodynamic Instabilities – A Compressor Blade Study", ASME Paper GT-2003-38634, 2003.

[3] März, J., Hah, C. and Neise, W., "An Experimental and Numerical Investigation Into the Mechanisms of Rotating Instability", ASME Journal of Turbomachinery, vol. 124, pp.367-375, July 2002.

[4] Mailach, R., Lehmann, I. and Vogeler, K., "Rotating Instabilities in an Axial Compressor Originating from the Fluctuating Blade Tip Vortex", ASME Journal of Turbomachinery, vol.123, pp.453-463, July 2001.

[5] Vo, H.D., Tan, C.S. and Greitzer, E.M., "Criteria for Spike Initiated Rotating Stall", ASME Journal of Turbomachinery, vol. 130, Jan. 2008, DOI:10.1115/1.2750674.

[6] Vo, H.D., "Role of Tip Clerance Flow in the Generation of Non-Synchronous Vibrations", AIAA Paper 2006-629, Proceedings of the 44th AIAA Aerospace Sciences Meeting and Exhibit, Reno, Nevada, 2006.

[7] Ho, C.-M. and Nosseir, S., "Dynamics of an Impinging Jet Part I: The Feedback Phenomena", Journal of Fluid Mechanics, vol. 105, pp.119-142, 1981.

[8] Thomassin, J., Vo, H.D. and Mureithi, N.W., "Blade tip clearance flow and compressor NSV: The jet core feedback theory as the coupling mechanism", ASME Journal of Turbomachinery, vol. 131, Jan. 2009, DOI:10.1115/1.2812979.

[9] Thomassin, J., Vo, H.D. and Mureithi, N.W., "Experimental Demonstration to the Tip Clearance Flow Resonance behind Compressor NSV", proceedings of GT2008: ASME Turbo Expo 2008: Power for Land, Sea and Air, June 9-13, 2008, Berlin, Germany, GT2008-50303.

[10] Menter, F. and Egorov, Y., "Turbulence Modeling of Aerodynamic Flows", International Aerospace CFD Conference, Paris, june 18-19, 2007.

[11] Thorsten, G. and Othmer, C., "Evaluation of Aerodynamic Noise Generation: Parameter Study of a Generic Side Mirror Evaluating the Aeroacoustic Source Strength", European Conference on Computational Fluid Dynamics, ECCOMAS CFD 2006, TU Delft, The Netherlands, 2006.

[12] Spille-Kohoff, A., "Acoustic Simulations with ANSYS CFX", CFX Berlin Software GmbH, 24th CADFEM Users' Meeting 2006 International Congress on FEM Technology with 2006 German ANSYS Conference, Stuttgart Region, October 25th – 27th 2006.

[13] Spiker, M.A., Kielb, R.E., Hall, K.C. and Thomas, J.P., "Efficient Design Method for Non-Synchronous Vibrations using Enforced Motion", proceedings of GT2008: ASME Turbo Expo 2008: Power for Land, Sea and Air, June 9-13, 2008, Berlin, Germany, GT2008-50599.

[14] Blevins, R.D., "Flow Induced Vibrations", 2nd Edition, Krieger Publishing Company, Malabar, Florida, 1990.

[15] Lucas, M.J.,"Acoustic Characteristics of Turbomachinery Cavities", ASME Press, New York, 1997.

APPENDIX 3 – Additional Numerical Results

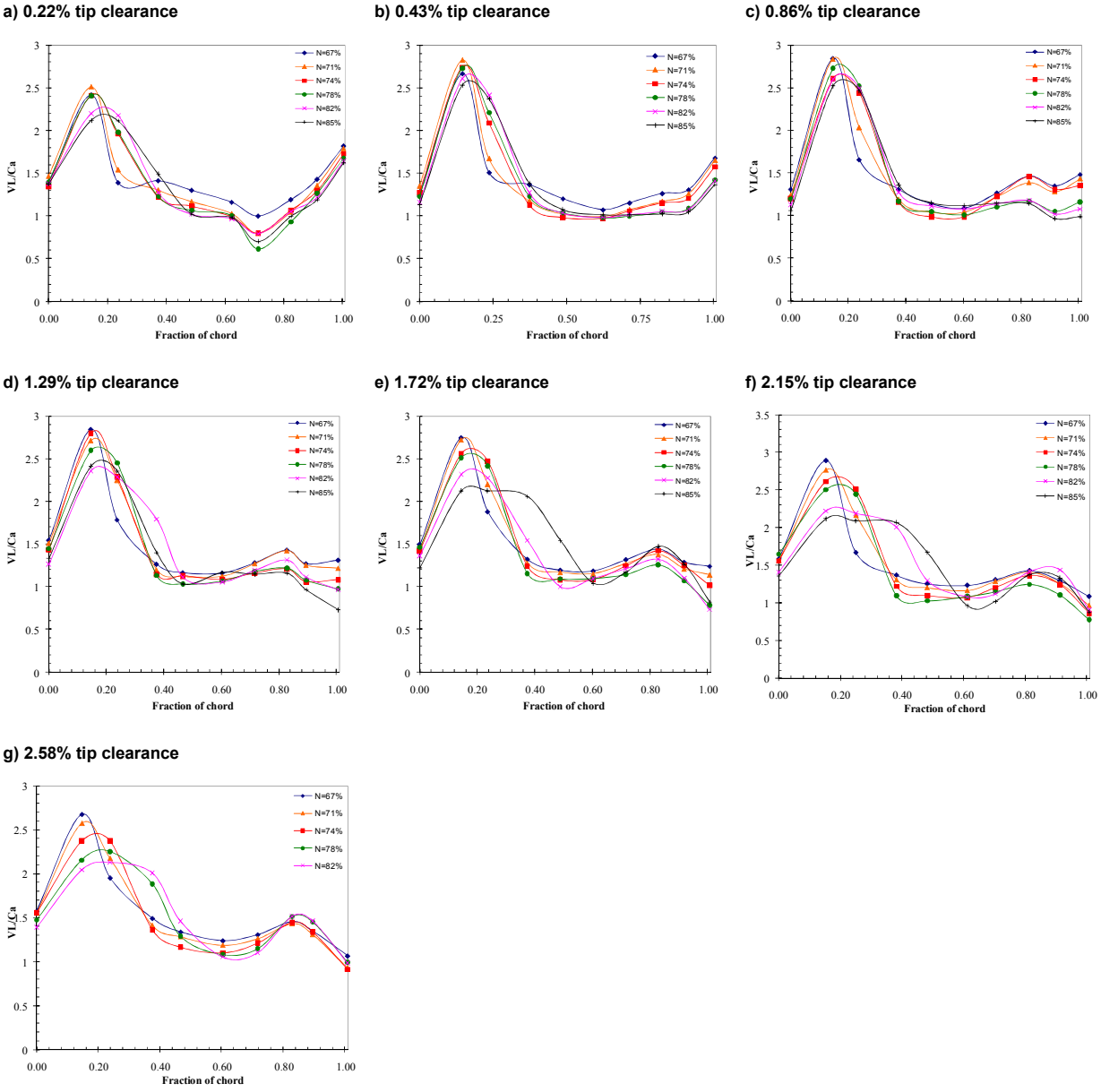

Figure A3.1 : TR geometry - Chord-wise V_L profiles calculated at different speeds and tip clearances

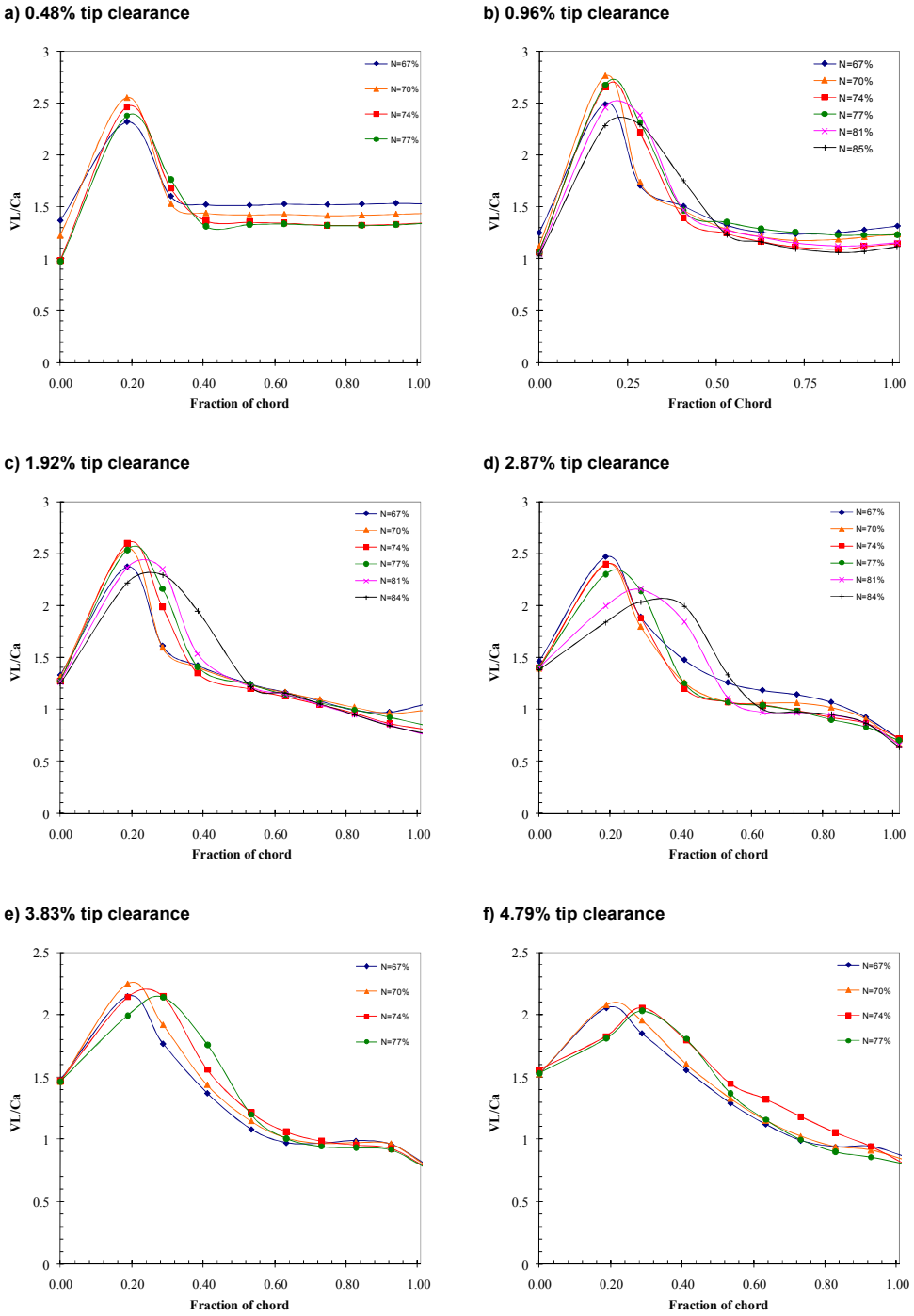

Figure A3.2 : SR geometry - Chord-wise V_L profiles calculated at different speeds and tip clearances

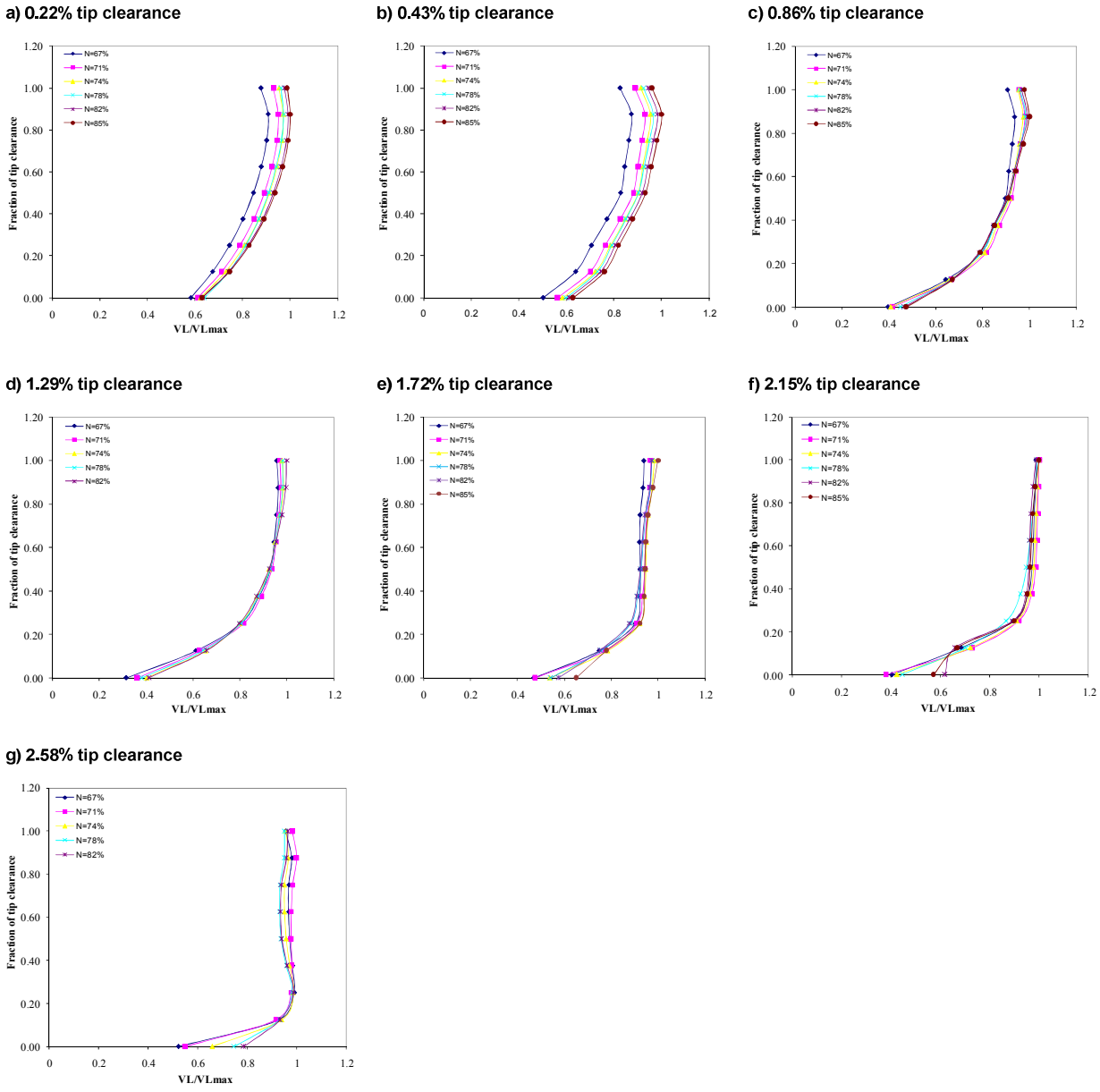

Figure A3.3 : TR geometry - Calculated tip leakage velocity profiles (span wise) at different speeds and tip clearances

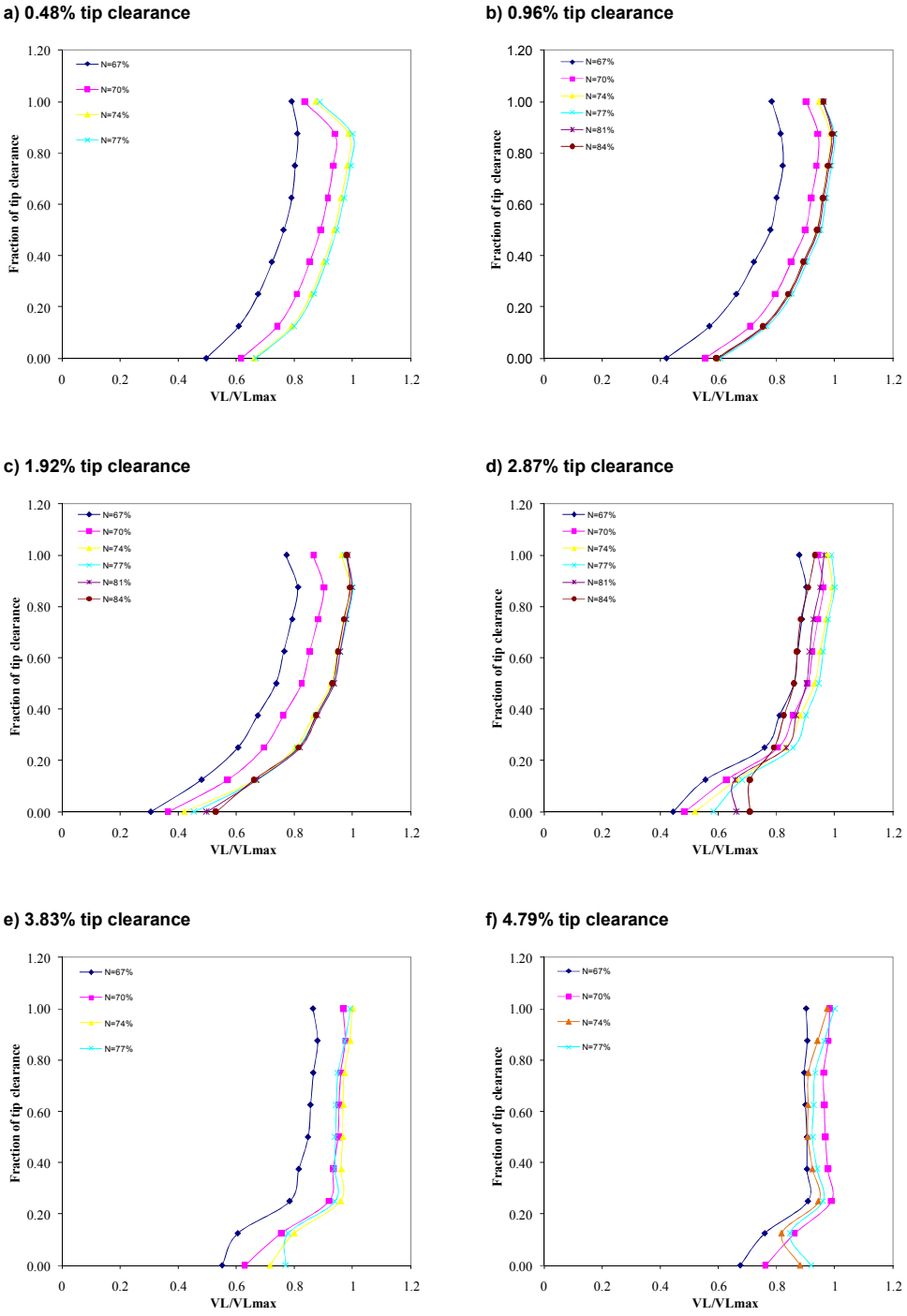

Figure A3.4 : SR geometry - Chord-wise V_L profiles calculated at different speeds and tip clearances